

A STUDY ON THE EFFECTS OF ELECTRICAL STIMULATION ON
NEURONAL STRUCTURE AND ACTIVITY

by

Genevieve Margaret Abd

A Dissertation Submitted to the Faculty of

Charles E. Schmidt College of Science

In Partial Fulfillment of the Requirements for the Degree of

Doctor of Philosophy

Florida Atlantic University

Boca Raton, FL

August 2022

Copyright 2022 by Genevieve Margaret Abd

A STUDY ON THE EFFECTS OF ELECTRICAL STIMULATION ON
NEURONAL STRUCTURE AND ACTIVITY

by

Genevieve Margaret Abd

This dissertation was prepared under the direction of the candidate's dissertation advisor, Dr. Jianning Wei, Department of Biomedical Sciences, and has been approved by all members of the supervisory committee. It was submitted to the faculty of the Charles E. Schmidt College of Science and was accepted in partial fulfillment of the requirements for the degree of Doctor of Philosophy.

SUPERVISORY COMMITTEE:




Jianning Wei, Ph.D.
Dissertation Advisor


E Du (Jul 15, 2022 10:50 EDT)

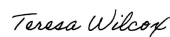
E Du, Ph.D.



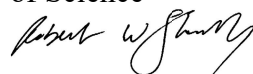
Erik D. Engeberg, Ph.D.


Sarah Milton (Jul 19, 2022 17:00 EDT)

Sarah L. Milton, Ph.D.
Chair, Department of Biological
Sciences



Teresa Wilcox, Ph.D.
Interim Dean, Charles E. Schmidt College
of Science



Robert W. Stackman Jr., Ph.D.
Dean, Graduate College


Sarah Milton (Jul 19, 2022 17:00 EDT)

Sarah L. Milton, Ph.D.

July 20, 2022

Date

ACKNOWLEDGEMENTS

I would like to express my sincere gratitude to my committee members, Dr. Erik Engeberg, Dr. Sarah Du, and Dr. Sarah Milton for their guidance and support through this project and my journey through this Ph.D. I would also like to pay my respects to my former committee member, Dr. Emmanuelle Tognoli and acknowledge her for the time and guidance that she gave me in the too short time that I was able to know her. A special thanks goes my advisor for her persistence, patience, and leadership through this academic experience. I would also like to thank the NIH institute for providing the research contract to conduct the research in chapter 1 of this dissertation. Research reported in this chapter was supported by R01EB025819 and R21NS111202. To all the lab collaborators and post-docs in this project, many thanks for your support. A special thanks to Darryl Dieujuste for providing technical assistance in image analysis. Lastly, I would like to thank my husband in life and colleague in research for his support in completing this academic journey.

ABSTRACT

Author: Genevieve Margaret Abd
Title: A Study on the Effects of Electrical Stimulation on Neuronal Structure and Activity
Institution: Florida Atlantic University
Dissertation Advisor: Dr. Jianning Wei
Degree: Doctor of Philosophy
Year: 2022

Chapter 1: Background: The search for effective electric stimulation protocols for peripheral nerve regeneration, specifically in dorsal root ganglion (DRG), is an ongoing area of interest. Multiple stimulation parameters using direct current, alternating current and pulsed magnetic electric fields have proven to increase neurite regeneration. In the past, there has been limited exploration of the impact of action potential-like electrical stimulation on DRG regeneration. *New method:* A novel action potential-like electrical stimuli output from a custom-built action potential generator board was used to assess multiple stimulation parameters on DRG regeneration. Finite-element modeling was used to determine electrolyte potential across a non-uniform electric field to test the effects of electric field strength from action potential-like stimuli on DRG regeneration. Total neurite length and neurite branching per DRG were examined for each applied field strength and

frequency to determine the effects of action potential-like stimulation on DRG structural regeneration. *Results:* Action potential-like stimulation showed inhomogeneous distribution of neurite regeneration and branching with higher regeneration and branching seen in areas away from the electrodes compared to the nearly homogenous distribution seen from the controls. Whole well analysis showed significant increases in total neurite regeneration and branching across all stimulation conditions with electric field strength, particularly 40 V/m, having the strongest effect on DRG structural regeneration. *Comparison with existing methods:* This study provides preliminary evidence supporting the hypothesis that action potential-like electric fields can improve DRG regeneration. *Conclusions:* This system and method may have applications for clinical interventions aimed at rehabilitating damaged peripheral nerve pathways.

Chapter 2: Background: Microelectrode arrays (MEAs) are suited for *in vitro* electrical and synaptic manipulations of neuronal cultures to study network activity at the whole culture level under normal and diseased conditions. *Method:* 24-well MEAs with 12 electrodes per well were used to examine parameters categorized into three levels of neuronal activity; spiking activity, neuronal excitability, and neuronal connectivity. These parameters were used to determine a stable developmental time window and determine the most robust parameters to perform pilot studies with electrical stimulation and neurotransmitter agonists to observe direct and synaptic responses for future comparison to diseased phenotypes. *Results:* Utilizing four batches of dissociated, primary cortical neurons, a stable time window was found from DIV10-DIV19. Descriptive analysis

determined % spikes in network burst, mean burst spike rate, % spikes in burst, mean network burst duration, mean network burst spike rate, and mean burst duration to be the most robust neuronal activity parameters batch-to-batch. Electrical stimulation with five biphasic pulses, 500 μ s wide per pulse, with an interpulse interval of 10 ms, in combination with AMPA and NMDA receptor agonist, showed that our stimulation protocols did not elicit electrical responses to the stimuli, but rather glutamatergic dependent synaptic responses. The addition of picrotoxin, a GABA_A receptor antagonist, increased bursting activity parameters as well as increased synchrony of activity in medium spiny neurons.

Comparison with existing methods: This study provides pilot test results for the establishment of stable, primary neuronal networks in a MEA platform. Pilot tests of electrical and synaptic evoked responses from MEA electrical stimulation will contribute to eventually establishing the MEA as a mechanistic tool to bridge molecular and phenotypic network activity for the future comparison with diseased neuronal networks.

A STUDY ON THE EFFECTS OF ELECTRICAL STIMULATION ON NEURONAL STRUCTURE AND ACTIVITY

| | |
|---|------|
| 1 LIST OF TABLES | xi |
| 2 LIST OF FIGURES | xiii |
| 1 STURCTRUAL (RE)GENERATION OF CULTURED DROSAL ROOT GANGLION NEURONS IN RESPONSE TO BIOLOGICAL ACTION POTENTIAL-LIKE STIMULI..... | |
| | 1 |
| 1.1 Introduction..... | 1 |
| 1.2 Experimental Methods | 6 |
| 1.2.1 Action potential generator board..... | 6 |
| 1.2.2 Electric chambers and stimulation parameters..... | 8 |
| 1.2.3 Finite element model | 9 |
| 1.2.4 Primary DRG culture | 11 |
| 1.2.5 DRG axotomy and electrical stimulation | 12 |
| 1.2.6 Immunohistochemistry staining | 12 |
| 1.2.7 Imaging and data analysis for DRG regeneration and orientation in response to action potential-like stimulation | 13 |
| 1.3 Results..... | 17 |

| | | |
|-------|---|----|
| 1.3.1 | DRG spontaneous regeneration assessment after axotomy..... | 17 |
| 1.3.2 | Verification of finite-element modeling for DRG stimulation | 19 |
| 1.3.3 | Assessment of post-axotomy recovery time and electrical stimulation on DRG structural regeneration | 22 |
| 1.3.4 | The effects of frequency on DRG structural regeneration with action potential-like stimuli | 25 |
| 1.3.5 | DRG neurite orientation after action potential-like stimulation..... | 28 |
| 1.4 | Discussion | 31 |
| 1.5 | Conclusions..... | 35 |
| 1.6 | Future directions | 35 |
| 2 | INVESTIGATION OF NEURON ACTIVITY AND CONNECTIVITY USING MULTI-MICROELECTRODE ARRAYS..... | 37 |
| 2.1 | Introduction..... | 37 |
| 2.2 | Experimental Methods | 48 |
| 2.2.1 | Primary neuronal cultures | 48 |
| 2.2.2 | MEA recording, parameters, and data analysis | 50 |
| 2.3 | Results..... | 61 |
| 2.3.1 | Temporal analysis of neuronal activity in dissociated, primary cortical neurons..... | 61 |
| 2.3.2 | Electrical stimulation-evoked activity in primary mouse neuronal culture | 68 |

| | | |
|-------|---|-----|
| 2.3.3 | Development profile of medium spiny neurons differentiated from iPSCs..... | 82 |
| 2.4 | Discussion..... | 90 |
| 2.5 | Conclusions..... | 99 |
| 2.6 | Future directions | 100 |
| 3 | APPENDICES | 101 |
| | Appendix A. List of Published Papers | 102 |
| | Appendix B. List of Papers Under-Preparation | 103 |
| 4 | REFERENCES | 104 |

1 LIST OF TABLES

| | |
|--|----|
| Table 1-1 Review of stimulation parameters used for DRG growth, outgrowth, or regeneration..... | 4 |
| Table 1-2 Parameters used to study DRG regeneration with action potential-like stimulation. | 8 |
| Table 1-3 Variables for dynamic electrode potential over time. | 10 |
| Table 1-4 Time averaged potential (V) of each region was calculated from the 0.4 V normalized potential..... | 22 |
| Table 1-5 One-way ANOVA p-values for all stimulation conditions in comparison to the control. | 26 |
| Table 1-6. T test mean and standard deviation (SD) for all stimulation conditions..... | 27 |
| Table 2-1 Approaches used at the single cell level (patch clamp), whole culture level (MEA), and whole organ level (functional MRI) to assess neuronal activity..... | 45 |
| Table 2-2 Definitions of parameters used to measure neuronal activity. | 53 |
| Table 2-3 List of guidelines. Guidelines were provided concerning the experimental design, cell culturing conditions, and MEA data analysis for this study. | 55 |
| Table 2-4 Stimulation parameters applied to cortical neurons DIV12. | 58 |

| | |
|---|----|
| Table 2-5 Information regarding the three independent batches of mouse primary neuronal cultures used for this study..... | 64 |
| Table 2-6 Calculated ranges in which MEA parameters of one MSN batch of cells behave. | 86 |

2 LIST OF FIGURES

| | |
|---|----|
| Figure 1-1 Customized action potential generator board. (a) The PCB has eight outputs (b-i) that can be pre-programmed or controlled in real-time to produce a variety of action potential patterns. The action potentials can consist of independent or spatiotemporally patterned spiking or bursting signals. The realistic action potential waveforms (j-k) can be programmed to vary in polarity, frequency, amplitude, and phase. | 7 |
| Figure 1-2 Method for quantitating neurite orientation according to the applied electric field in an 8-well chamber. The left figure shows the reference angle set-up according the chamber well. The figure on the right shows the direction of the neurites growth's deflection (turning). The angle(s) of the neurites tips (θ tip) was subtracted from the angle(s) initiating from the soma (θ root) of the same DRG neuron to yield the angle(s) of turning relative to the electric field direction (θ deflection). | 16 |
| Figure 1-3 DGR spontaneous regeneration assessment after axotomy. (a and c) Cells were fixed and stained with DAPI and β -III-tubulin, a neuronal marker, after axotomy at specified time endpoints. (b and d) Neurite length was assessed with NeurphologyJ at each time point. Data shown as averaged total neurite length per DRG (μ m) with SEM. | 19 |
| Figure 1-4 (a) Electrodes were fitted from the top of the lid to the bottom of the chamber with a 10 mm diagonal distance between the anode electrode and the cathode electrode. (b) Resulting | |

potentials with 0.2 V excitation for each of the seven regions over a 1 ms time period. (c-d) Simulation with 0.2 V excitation across the chamber well represented at two chosen time points ($T = 0.2$ ms and $T = 1$ ms) to show electric potential change (colored bar) as the electric potential (V) traveled from the anode and cathode electrode..... 21

Figure 1-5 Total neurite length and endpoints per DRG significantly increased with a two hour post-axotomy stimulation start time using an applied 0.2 V or 0.4 V at 250 Hz. (a-c) Cells were fixed and stained with β -III-tubulin, a neuronal marker, 24 hours after each stimulation parameter. (d) Cell stimulated with 0.2 V or 0.4 V at 250 Hz showed significant neurite regeneration and (e) increased neurite endpoints with a two hour post axotomy recovery. (f-g) Significant neurite regeneration was seen with an applied 0.6 V while an increased number of neurite endpoints was seen with an applied 0.2, 0.4, and 0.6 V amplitude with the three hours post-axotomy stimulation. (h-i) Significant structural regeneration was seen with an applied 0.2 V with the four hour post-axotomy stimulation start time. Statistical analysis based on one-way ANOVA with Dunnett's multiple comparisons test. 24

Figure 1-6 Action potential-like stimulation significantly increased total neurite outgrowth and neurite branching. Brightfield images of the DRG culture were taken before axotomy (a). Cells were fixed and stained with β -III-tubulin, a neuronal marker, after axotomy (b) and stimulated 24 hours afterwards with 20 V/m or 40 V/m field strengths at 20 Hz or 250 Hz frequencies (c-g). Averaged data from multiple wells per region showed inhomogeneous regeneration (h) and branching (i) for the stimulated DRG and nearly homogenous neurite regeneration (h) and neurite branching (i) for the control groups. More regeneration (h) and branching (i) was noted

| | |
|--|----|
| in regions away from the electrodes. Whole well analysis for each stimulation condition showed that action potential like stimulation significantly increased neurite regeneration (j) and branching (k) for all conditions. Further statistical analysis showed that field strength rather than frequency had a greater effect on neurite length (j) and branching (k). No significance was indicated with n.s. Scale bar shown as 100 μ m for the brightfield and confocal images..... | 27 |
| Figure 1-7 No neurite orientation seen with DRG neurites after action potential-like stimulation. | |
| (a-f) Neurite deflection across all stimulation parameters shown with Gaussian best fit lines. | |
| (g-l) Orientation of neurite tips shown across all stimulation parameters shown with Gaussian best fit lines. Cells were analyzed for alignment 24 hours post stimulation with ImageJ..... | 30 |
| Figure 2-1 Schematic time frame of the differentiation protocol of iPSCs to MSNs. | 50 |
| Figure 2-2 Multiwell MEA system (1) and 24-well plate (2) with poly(3,4-ethylenedioxythiophene) (PEDOT) coated gold electrodes. Each well contained 12 electrodes that were 30 μ m in diameter and 300 μ m apart..... | 51 |
| Figure 2-3 MEA analysis flow chart with inclusion and exclusion criteria. | 52 |
| Figure 2-4 Schematic of parameters measured from the analyzed MEA data. | 54 |
| Figure 2-5 Biphasic stimulation pulse and stimulation timing scheme. (a) Characteristic, biphasic pulse showing a pulse width of 100 μ s for the positive and negative peaks. (b) Stimulation timing showed an interburst interval of 10,000 ms with a burst consisting of 5 spikes. The IPI of those 5 spikes was 10 ms. Stimulation was stopped by 100 ms..... | 57 |
| Figure 2-6 Inhibitory and excitatory drug effects on post-synaptic terminals. (a) CNQX is an antagonist of AMPA receptors and block the ion flow of sodium intracellularly which leads to | |

depolarization of the post-synaptic side. MK801 is an antagonist of NMDA receptors and blocks the ion flow of sodium and calcium intracellularly which leads to depolarization on the post-synaptic side. (b) Axons that release GABA on the pre-synaptic side will bind to GABAA modulation sites of the receptor on the post-synaptic side. Activation of GABAA allows for the influx of chloride intracellularly which leads to hyperpolarization of the membrane potential on the post-synaptic side. Picrotoxin blocks the GABAA receptor..... 60

Figure 2-7 Developmental profile of spontaneous activity for dissociated, primary neurons. (a)

Representative brightfield image of well with neurons in contact with the electrodes and showing even distribution. (b) Representative raster plot of network activity across twelve electrodes during stable time window of DIV13. Red lines indicate spiking activity. Red boxes indicated bursting activity. Network activity highlighted in light blue. (c-m) Temporal analysis showing stable neuronal activity indicated with gray boxes for each parameter was determined with one-way ANOVA followed by multiple comparisons test. Orange line represented the median for each parameter from a total of 12 wells. Each gray line represents the calculated average of 12 electrodes per well for each parameter over the duration of the temporal analysis. 63

Figure 2-8 Neuronal networks showed a stable phenotype on MEA. (a) Coefficient of network

interburst interval of all four batches of cortical cells separately and pooled together indicating regularity of network burst with a value below 1. Mean \pm SEM shown with black lines. (b) Graph showing the range in which the MEA parameters of all three batches behaved from DIV10-DIV19. Values were averaged per batch and then averaged across all batches with SD.

| | |
|--|----|
| (c) Percent coefficient of variation of all 11 parameters across three batches DIV10-DIV18 to determine the most robust parameters with 50% as the cutoff points. Mean \pm SD shown with black lines. nwells=53. (d) PCA loading plot to showed 55 possible correlations of the 11 parameters DIV10-DIV19 from the three combined batches. PC score graph showed individual batch clustering DIV10-DIV19. | 67 |
| Figure 2-9 Well-wide analysis of batch 4. (a) Temporal raster plot from representative well A4 on DIV11 showing spikes (black lines) bursts (red blocks), and network bursts (highlighted in blue). (b) Example of criteria used to select one stimulating electrode per well. (c) Extracted spike counts of each electrode from all 24 wells. (d) Extracted burst counts of each electrode from all 24 wells. (e) Extracted network burst counts of each electrode from all 24 wells. Data shown as mean with SEM. | |
| | 71 |
| Figure 2-10 Variation of network activity accounted across 23 wells from batch 4. (a) PCA loading plot showed 55 possible correlations of the 11 parameters of 23 wells from a single batch of dissociated, cortical neurons on DIV11. PC score graph showed individual well clustering on DIV11. | |
| | 73 |
| Figure 2-11 Raster plot of representative A4 well. The stimulating electrode was electrode 31. Detected burst highlighted in red, network burst highlighted in blue, electrical stimuli highlighted in gold, and random spikes shown as black lines across all 12 electrodes for a time period of 120 seconds. Direct and synaptic responses occurred within milliseconds after the stimuli before spontaneous activity resumes. | |
| | 75 |

Figure 2-12 Firing activity of electrode 12 of well A4 for all 15 electrical stimulation protocols. (a)

Applied biphasic 100 μ s pulse width with increasing voltage shown within blue box. (b)

Applied biphasic 250 μ s pulse width with increasing voltage shown within green box. (c)

Applied biphasic 500 μ s pulse width with increasing voltage shown within red box..... 77

Figure 2-13 Spiking activity from direct and synaptic responses as a response to pulse width and

voltage. (a) Spiking activity across 600 ms bins (excluding the first 50 ms bins) of the

representative well A4, electrode 12 (b) Spiking activity of direct and synaptic responses to

pulse width and voltage showed a downward trend with 250 μ s and 500 μ s pulse widths above

100 mV. Data shown as mean with SEM. 79

Figure 2-14 Effects of excitatory and inhibitory drugs neuronal activity parameters of dissociated

cortical neurons. (a) Representative raster plots of cortical activity on DIV19 before and after

the addition of both 10 μ M CNQX and 20 μ M MK801. (b-d) Three parameters measure showed

no spiking activity after the addition of CNQX plus MK801 confirming it agonist effects on

excitatory neurons. 81

Figure 2-15 Effects of agonist on excitatory neurons after evoked activity. (a) A single electrode

from each of the 12 wells pooled from row C-D were shown with stimulation after stimulation

as the mean with the range. (b) The same 12 wells pooled from row C-D, where CNQX and

MK801 were added, showed no spiking activity in response to stimulation. 82

Figure 2-16 Developmental profile of spontaneous activity for MSNs. (a) Representative raster plot

of a culture well on DIV14. Stable neuronal activity indicated with gray boxes for each

parameter (c-m). Orange line represented the medium for each parameter from a total of 6 wells

| | |
|--|----|
| (c-m). Each gray line represent the calculated average of 12 electrodes per well for each parameter over the duration of the temporal analysis (c-m)..... | 85 |
| Figure 2-17 The effects of PTX on increasing MSNs activity parameters DIV34. (a) Representative raster plots from well C6 of MSNs on DIV34 before (baseline) and after the addition of 10 μ M PTX. (b-m) Unpaired t-test was used to determine significance ($p>0.05$) after the addition of PTX (nwells= 6, nelectrodes= 72) across all 12 parameters of activity. | |
| | 89 |

1 STRUCTURAL (RE)GENERATION OF CULTURED DORSAL ROOT GANGLION NEURONS IN RESPONSE TO BIOLOGICAL ACTION POTENTIAL-LIKE STIMULI

1.1 Introduction

The pursuit for effective electrical stimulation protocols to promote neurite outgrowth and regeneration in peripheral neurons, such as dorsal root ganglion neurons, is an active area of research [1], [2]. Most studies have focused on the effects of direct current [3], [4], [5], [6], alternating current [1], [7], [8], or pulsed magnetic fields [9], [10] on DRG outgrowth and regeneration. These studies revealed that neurons have a broad response to a variety of electrical stimulation protocols in terms of neurite outgrowth and regeneration.

The ability of electrical stimuli to enhance nerve regeneration has been well demonstrated both *in vivo* and *in vitro*. On the efferent side, one study demonstrated that electrical stimulation applied to the spinal cord or sciatic nerve root axon accelerated axon sprouting in partially denervated muscle by means of sinusoidal electrical stimulation at 50 to 100 Hz for 10 to 60 minutes [11]. Studies on physical therapies found that electrical stimulation is an artificial means to induce activity in axotomized neurons while exercise is the natural way to achieve the same [12], [13], [14], [15]. This activity enhances the expression of brain-derived neurotrophic factor (BDNF) and pro-regenerative associated

genes which expedited sensory [16] and motor [17] axon growth in rat models. Moderate exercise promoted axonal sprouting in partially denervated muscles [18], [19]. In the same approach, low frequency electrical stimulation at 20 Hz had positive effects on axonal regeneration and muscle reinnervation potentially because 20 Hz is approximately the mean firing frequency of motor neurons in both humans and animals [20].

On the afferent side, direct current electric fields within the range of 20 Hz to 200 Hz with corresponding electric field ranges up to 25 V/m positively influenced DRG outgrowth [3], [4]. In an in vitro study that utilized low intensity pulsed ultrasound stimulation, 20 Hz with voltages of 0.5 V or 0.8 V significantly increased DRG neurite outgrowth and branching 18 hours after a 3 minute stimulation duration [21]. In a study that demonstrated the synergetic effects of substrate stiffness and electrical conductivity of carbon nanotube-hydrogel composites, neurons stimulated for 1 hour with 30 V/m direct current showed increased neurite outgrowth and mean neurite length by 2-fold and 1.8-fold, respectively [22]. We previously showed that stimulation frequency can alter DRG neurite growth in vitro [1]. Stimulation applications for pain management and analgesia have found that low frequency signaling (< 20 Hz) activates the native endogenous opioid system which inhibits action potential signals while higher frequencies (> 25 Hz) excite neuron activity [23]. Frequencies as low as 4 Hz have demonstrated clinical effectiveness at modulating DRG neurotransmission by mimicking low-threshold mechanoreceptor fibers that transmit or modulate innocuous tactile sensations [23]. Computational modeling of DRG stimulation for chronic pain indicated that afferent signaling was blocked via T-

junction filtering in stimulated DRGs with frequencies above 2 Hz at amplitudes of 2.8-5.5 x the stimulation threshold of -20 mV [24]. This model confirmed that the amplified filtering at the T-junction was dependent on calcium and calcium-dependent small conductive potassium channels to produce a hyperpolarization offset in the soma, neurite stem, and T-junction of the modeled DRG with repeated action potentials during the stimulation [24]. In an in vitro study utilizing ganglionic field stimulation, 60 Hz at 30 V with 400 μ sec pulses reduced the generation of action potentials in the soma of intact DRG during membrane depolarization [25].

Table 1-1 Review of stimulation parameters used for DRG growth, outgrowth, or regeneration.

| <i>Current type</i> | <i>Study type</i> | <i>Magnitude, potential, or pulse trains</i> | <i>Frequency</i> | <i>Stimulation Duration</i> | <i>Time between stimulation and analysis</i> | <i>Results</i> | <i>Ref.</i> |
|---------------------|-------------------|--|------------------------------|-----------------------------|--|--|-------------|
| Direct current | <i>In vivo</i> | 100 ms with 3-5 V pulses | 20 Hz | 1 hour | 3 weeks | 70% increased stimulated neurite regeneration compared to 40% regeneration without stimulation | [5] |
| | <i>In vivo</i> | 25 V/m | N/A | 10 minutes | 48 hrs | Increased outgrowth on laminin and collagen substrates | [3] |
| | <i>In vivo</i> | 100 μ s at 3 V | 20 Hz | 1 hour | 21 days | Significant increase in regeneration and reinnervation into surrounding cutaneous and muscle branches | [16] |
| Alternating current | <i>In vivo</i> | 0.1 ms at 3 V | 20 Hz | 1 hour | 1, 3, 5, 7, and 9 weeks | Increase number of regenerated myelinated axons in groups that received stimulation and/or exercise | [15] |
| | <i>In vivo</i> | Bipolar pulses | 20 Hz; 200 Hz | 1 hour | 14 weeks | Upregulation of neurotrophic factors and receptors that precede accelerated upregulation of growth associated genes | [26] |
| | <i>In vivo</i> | 1 mA | 2 Hz; 20 Hz; 20 Hz | 15 minutes every other day | 7, 14, 21, and 28 days after injury | Improved regeneration at 20 and 200 Hz 4 week after injury compared to 0 and 2 Hz. | [27] |
| | <i>In vitro</i> | 1-10 V biphasic rectangular pulses | 0.1-100 Hz | 30 minutes | 1, 3, and 5 days | Increased neurite length seen with 1 Hz, 10 Hz, and 100 Hz at 5 V; increased neurite length seen with 5 V and 10 V at 10 Hz on days 1, 3 and 5 | [28] |
| | <i>In vitro</i> | 17.86 V/m sinusoidal pulses | 20 Hz; 200 Hz; 1 MHz; 20 MHz | 1 hour | 24 and 48 hours | Megahertz stimulation does not enhance or impair neurite growth; 20-200 Hz increases radial growth, intracellular calcium, and neurite orientation | [1] |
| | <i>In vitro</i> | 100 μ s biphasic pulse at 2 μ A | 20 Hz | 1 hour | Daily from days 1-7 | Significant neurite regeneration seen from days 1-7 | [7] |
| Pulsed current | <i>In vitro</i> | Asymmetric, 220 ms-wide, 4.0 mT-peak pulses | 15 Hz; 25 Hz | 18 hours | 6 hours | Significant asymmetric neurite outgrowth in combination with neural growth factor with no preferred orientation to induce electric field | [29] |
| | <i>In vitro</i> | 20 μ s pulses at 0.25 V/m | Between 10 & 25 Hz | 18 hours | 18 hours | Significant asymmetrical growth with directional growth parallel to the current's direction | [10] |
| | <i>In vitro</i> | 1000 cycles/pulse, 3600 pulses at 0.2, 0.5, or 0.8 V | 20 Hz | 3 minutes | 18 hours | 2.83-fold increased neurite outgrowth and 2-fold neurite branching compared to controls | [21] |

These studies strongly suggest that electrical stimulation holds significant value in promoting increased neurite outgrowth and regeneration. The optimal electrical parameters in promoting neurite regrowth and functional recovery however remains elusive. Natural signaling in peripheral nerves possess more dynamical complexity than what is embedded in direct current, alternating current, or pulsed magnetic fields, and this complexity might be important for functional restoration of the nerve pathways.

In this paper, the two features that we explored for adaptive plasticity of the regenerative processes were the field strength and frequency. An already established electrical stimulation protocol which implements biometric electrical stimulations that mimic physiological action potential propagation and its dynamic patterns is the mathematical Izhikevich's model [30]. This model will be used to provide insight on the association of biomimetic electric stimuli and DRG neurite regeneration. To physiologically model neuronal activity, we deployed a custom-built action potential generator board that output programmable waveforms comparable to physiological signals from human mechanoreceptors. The board is used in tandem with a finite element model to understand the electric field distribution and to tailor the stimulation spatiotemporally. The evolution of DRG morphology was compared for several action potential-like stimulation protocols that examined the effects of electric field strength and frequency on DRG regeneration in comparison to spontaneous DRG regeneration. Morphological changes were analyzed with the high throughput software NeurophologyJ that screened microscopy images and quantified structural regeneration. Unlike other methods using

direct and alternating electrical current stimulation and uniform electric fields, our method allows for analysis of biomimetic electrical stimulation on DRG regeneration across a range of electrical potentials and electric field strengths.

1.2 Experimental Methods

1.2.1 Action potential generator board

To generate action potential-like electrical stimuli, an innovative action potential generator board was developed (Figure 1-1). The board includes eight independent channels. Each channel is capable of outputting an action potential-like signal with programmable waveform, firing rate (frequency), polarity, amplitude, and resting potential. The action potential waveform is easily defined with a looked-up table of x, y coordinates and stored on an SD card integrated on the board. In addition, the action potential waveform can correspond to any shape indicative of the rising, peak, falling, undershoot, and refractory phases of physiological action potential cycles. The firing rate (frequency) of the action potential can be externally or internally triggered at a constant or variable frequency with the range of 0 to 50 kHz. Independent triggers can be generated up to 1 kHz using a USB serial interface. If internal triggering is used, then input pulses can be generated in bursts with a programmable burst rate and pulse count. For each trigger event, the sample waveform is outputted digitally using an onboard microcontroller with a digital-to-analog converter. The eight independent output channels were implemented with two quad 16-bit digital-to-analog converters driven by a microcontroller using a high-speed SPI interface. Each digital-to-analog output is low-pass filtered and fed to an output amplifier, providing

a user selectable gain with a full-scale output voltage range of ± 6 V or ± 0.6 V. This setup may be necessary to adapt to varied distance between the electrodes and the impedance of the media. The rated output current per channel is 10 mA maximum. The resting potential can also be modulated between the ± 6 V range to allow for DC electric fields to simulate different cellular disease states and cell types.

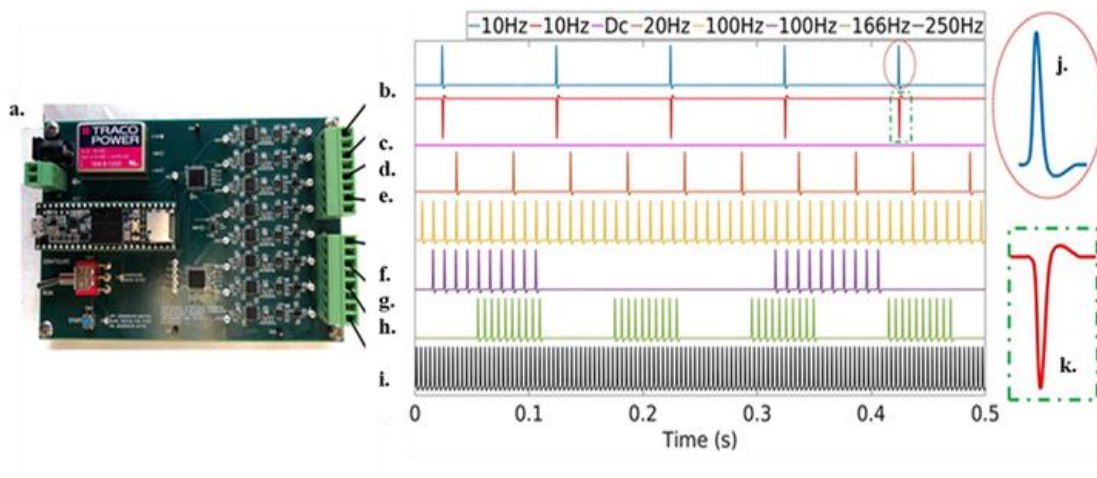


Figure 1-1 Customized action potential generator board. (a) The PCB has eight outputs (b-i) that can be pre-programmed or controlled in real-time to produce a variety of action potential patterns. The action potentials can consist of independent or spatiotemporally patterned spiking or bursting signals. The realistic action potential waveforms (j-k) can be programmed to vary in polarity, frequency, amplitude, and phase.

1.2.2 Electric chambers and stimulation parameters

Chambered coverslips with 8 wells (μ -Slide 8 well chamber) were purchased from Ibidi (USA). Non-toxic polylactic acid was used to 3-D print a fitted lid for the chamber. This lid provided a stable environment for electrode insertion for cultured DRGs during stimulation protocols. Gold electrodes extracted from 10 μ l Neon electroporation tips (ThermoFisher, USA) were utilized for the stimulation. These electrodes were 0.045 mm in diameter and two electrodes were inserted diagonally into one well at a 10 mm distance between the positive and negative electrodes. Gold electrodes produced a more uniform electric field and were less toxic to cells [31]. For the action potential-like stimulation parameters, electric field strengths of 20 V/m, 0.4 V/m, or 0.6V/m at frequencies of 20 Hz or 250 Hz were used to stimulate atomized DRG for one hour. All analyzed spontaneous and stimulation parameters used in this study were summarized in Table 1-2 below.

Table 1-2 Parameters used to study DRG regeneration with action potential-like stimulation.

| | DRG axotomy recovery duration | Electric field strengths | Frequency | Stimulation duration | Time between stimulation and analysis |
|------------|--|-------------------------------------|------------------|---------------------------------|--|
| (a) | Spontaneous regeneration/CTL | | | | 1h to 120h |
| (b) | 2h | 20 or 40 V/m | 20 Hz | 1h | 24h |
| (c) | 2h | 20, 40, or 60 V/m | 250 Hz | 1h | 24h |
| (d) | 3h | 20, 40, or 60 V/m | 250 Hz | 1h | 24h |
| (e) | 4h | 20, 40, or 60 V/m | 250 Hz | 1h | 24h |

1.2.3 Finite element model

Finite element analysis was performed to determine the electric field of the action potential-like pulse set at a 0.2 V amplitude excitation in the 11 x 10 mm chamber well. Thus, a two-dimensional finite element model was created in COMSOL Multiphysics environment. The simulated chamber well was divided into 7 regions with the anode electrode in the lower left corner and the cathode electrode in the upper right corner. For the simulation, the regions were meshed with extra fine quad meshes. The two electrode areas, whose radii were 0.045 mm, were defined by small circles and excluded from the calculation. The distance between the anode and cathode was set as 10 mm. The simulation was performed using a 0.3 S/m electrolyte conductivity and a H2O dielectric constant of 78 for the DRG complete neural basal media. The governing equations used for the COMSOL simulation can be seen from Equations 1:

$$\nabla \cdot J = Q_{j,v} \text{ (Equation 1)}$$

Where $\nabla \cdot J$ is the scalar current density and $Q_{j,v}$ was the unit change of current density and potential. According to the Ohm's law, the relation between J in Equation 2 and electrical field E was as follows:

$$J = \sigma E + \frac{\partial D}{\partial t} + J_e \text{ (Equation 2)}$$

Where σ represented the electrolyte conductivity at a value of 0.3 S/m. The electric displacement was represented by $\frac{\partial D}{\partial t}$. The externally generated current density was represented with J_e . The electric field intensity was given by Equation 3:

$$E = -\nabla v \text{ (Equation 3)}$$

Where E is the electric field intensity and $-\nabla v$ is the electric scalar potential. The boundary condition was fitted to the edges of the simulated chamber in COMSOL and was based on the positive electrode input equation from the action potential generator board. The simulated action potential-like excitation pulse of 0.2 V was shown with a total time of 1 second. In COMSOL software, the dynamic electrode potential over time was shown in Equation 4:

$$A = a_1 \cdot e^{-\left(\frac{t-b_1}{c_1}\right)^2} + a_2 \cdot e^{-\left(\frac{t-b_2}{c_2}\right)^2} - a_3 \cdot e^{-\left(\frac{t-b_3}{c_3}\right)^2} + a_4 \cdot e^{-\left(\frac{t-b_4}{c_4}\right)^2} \quad (\text{Equation 4})$$

The value of the variables for equation 4 were shown in Table 1-3.

Table 1-3 Variables for dynamic electrode potential over time.

| Coefficient | Value |
|----------------------|----------|
| t | 1 ms |
| a₁ | -0.07958 |
| b₁ | 0.621 |
| c₁ | 0.2112 |
| a₂ | 0.37 |
| b₂ | 0.1996 |
| c₂ | 0.04983 |
| a₃ | 0.02397 |
| b₃ | 0.002868 |
| c₃ | 0.04983 |
| a₄ | 0.7501 |
| b₄ | 0.2604 |
| c₄ | 0.09198 |

Once the simulation was done, region plots were exported as a data source. Then it was imported into the model as geometric entities to partition the calculation domain. After that, simulation results were updated. The surface average values were calculated for each

region from the 0.2 V excitation simulation. Furthermore, the calculated time-averaged potential at 0.2 V was used to generate the surface average potential values for the 20 V/m and 40 V/m field strengths used on the DRG cells.

1.2.4 Primary DRG culture

Mice pups at 1-3 postnatal days old (B6C3 strain) were used to prepare DRG neuronal culture as described [32]. Briefly, pups were euthanized with quick decapitation. Spinal columns were extracted and cut in half along the midline from the cranial to caudal of the spinal column. DRG bulbs were isolated from the central/peripheral dorsal root horns under a dissection microscope and stored in ice-cold dissection media [1 mM sodium pyruvate, 10 mM HEPES, 0.1% glucose in HEPES-buffered saline (HBSS), pH=7.4]. DRG tissue was then digested with 0.125% trypsin in dissection medium at 37°C for 10 minutes. At the end of incubation, 5% fetal bovine serum (FBS) was added to neutralize trypsin activity and the trypsin-digested tissue was further incubated with 0.4 mg/ml deoxyribonuclease I (DNase I, Sigma Aldrich, USA) at room temperature for 10 minutes. After the DNase incubation, the tissues were triturated with a fire-polished glass Pasteur pipette. The dissociated neurons were pelleted by centrifugation at 200 x g for 5 minutes and re-suspended in neurobasal medium supplemented with 2 mM glutaMAX, 1% B27, 1% penicillin/streptomycin and 100 ng/ml nerve growth factor (NGF, R&D systems). About 20,000 viable neurons were plated on a 35 mm culture dish coated with 0.1 mg/ml Poly-D-lysine (PDL, Sigma Aldrich, USA). After 45 minutes, the media was replaced with complete neurobasal medium. On DIV1 (1 Day *in vitro*), 1 μ M cytosine arabinoside was

added to the medium to inhibit non-neuronal cells growth and cells were further cultured at 37 °C with 5% CO₂. All animal procedures were approved by the Institutional Animal Care and Use Committee of Florida Atlantic University and in compliance with the National Institutes of Health Guidelines for the Care and Use of Laboratory Animals.

1.2.5 DRG axotomy and electrical stimulation

DRG at DIV6 were trypsinized and axotomy was performed by gently triturating the cell suspension in Dulbecco's modified eagle medium (DMEM) supplemented with 10% FBS, 1% glutamine and 1% penicillin/streptomycin six times. Axotomized DRGs were centrifuged at 200 x g for 5 minutes to remove the debris and re-suspended in complete neurobasal media. Axotomized DRGs were re-seeded in the 8-well chamber coated with 0.1 mg/ml PDL and 10 µg/ml laminin at 20,000 cells/well. The chambers were further incubated for two hours at 37 °C with 5% CO₂ to allow cell attachment before applying the stimulation protocol. In this study, we focused on the effects that different field strengths and frequencies and field of action potential-like stimuli had on DRG axonal regeneration. Stimulation duration was set for one hour since it has been shown to be effective for DRG outgrowth *in vitro* and *in vivo* [6], [16], [5], [7]. After stimulation, DRGs were further cultured for 24 hours before analysis with immunostaining. All spontaneous and stimulation experiments were conducted at 37 °C with 5% CO₂.

1.2.6 Immunohistochemistry staining

DRG were fixed 24 hours after last stimulation with 4% paraformaldehyde (PFA) for 10 minutes at room temperature. Immunostaining was performed as we previously

described [33]. Briefly, cells were first permeabilized with 0.25% Triton X-100 for 10 minutes followed by incubation with blocking buffer (1% bovine serum albumin (BSA) and 10% normal goat serum (NGS) in PBS) for one hour at room temperature. Cells were then incubated with primary antibody (Beta-III-tubulin, 1:1000, Abcam) in primary antibody dilution buffer (1% BSA, 1% NGS in PBS) for one hour at room temperature. After extensive washing with PBS, cells were further incubated with goat anti-mouse Alexa Fluor 488 secondary antibody (Invitrogen, 1:2000) in dilution buffer for one hour. Cells were counterstained with 4', 6-diamidino-2-phenylindole (DAPI). After secondary antibody incubation, cells were extensively washed with PBS to remove any unbound antibodies and left in PBS for imaging.

1.2.7 Imaging and data analysis for DRG regeneration and orientation in response to action potential-like stimulation

Fluorescently stained DRG were imaged with a Nikon A1R confocal microscope (Tokyo, Japan). A large area scan with a 10% overlap under a 10x objective (Plan Apo λ 10x, numeric aperture 0.45) was performed to cover the whole bottom of the well. The obtained images were used to quantify neurite length using NeurophologyJ, an autonomous algorithm publicly available as an ImageJ plugin [34]. The average total neurite length per neuron was determined by dividing the “neurite length” with the number of cells counted by DAPI staining. Neurite branching are defined as the location at the tip of the neuron [34]. The dependent variables measured were total neurite length and neurite branching per DRG. The independent variables were field strengths and frequency from action potential-

like waveform stimulation. To analyze the effect of the calculated electric field strength on total neurite length or neurite branching per DRG with our chosen field strengths, each confocal image was divided into the previously shown 7 regions that had corresponding calculated time averaged potential value. Total neurite length or neurite branching per DRG were analyzed continuously, meaning the soma of that cell in that specific regions was part of that region even if its neurite(s) crossed over into another region. Whole well analysis was done to compare the effects of electric field strength and frequency on neurite length and branching across an entire well. All experimental data was expressed as means \pm the standard error of the mean (SEM). To establish significance, data were subjected to one-way ANOVA followed by two-way unpaired t test using the GraphPad Prism software statistical package 9.0 (GraphPad Software). The criterion for significance was set at $p \leq 0.05$.

To quantify the overall direction of neurite regeneration compared to the direction of the electric field created by action potential-like stimulation, the method use by Rajnicek et al., 1998 [35] was adapted. Briefly, determination of asymmetric regeneration was under the assumption that the anode was at 45° and the cathode was at 225° (or -135°) (Figure 1-2). The deflection of neurite regeneration (θ deflection) was calculated from angle measurements obtained from the root or initiation site of the neurite from the cell body (θ root) minus the tip of each neurite (θ tip). Angle measurements were obtained manually with the standard angle measurement tool in ImageJ (version 1.8.0). All DRG were considered for angle analysis per well except for somas/neurites that were “interwoven”

together since the tips could not be identified/traced back to the original soma. Any negative angle values were converted to positive angle values by adding 360° to the negative value. All measured deflection angles were pooled into 9 bin centers from 0° to 360° with a bin width of 45° in frequency histograms. Statistical analysis with GraphPad Software of deflection angles from the stimulated DRG were compared to spontaneous control deflection angles using the Kolmogorov-Smirnov test. The criterion for significance was set at $p \leq 0.05$. Additionally, a Gaussian best fit nonlinear curve was added to the frequency histograms to show possible directional preference from the stimulated DRG compared to the applied electric field.

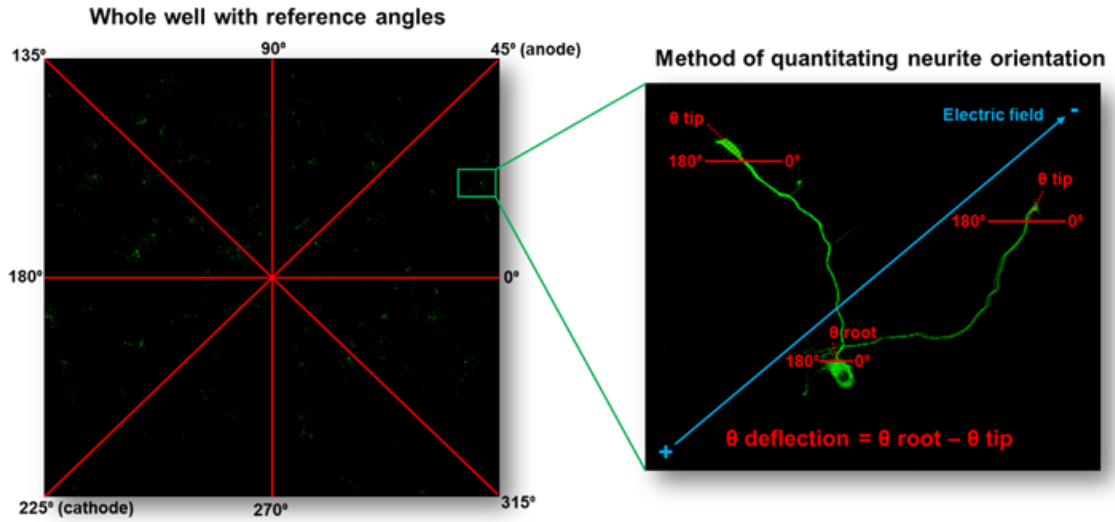


Figure 1-2 Method for quantitating neurite orientation according to the applied electric field in an 8-well chamber. The left figure shows the reference angle set-up according the chamber well. The figure on the right shows the direction of the neurites growth's deflection (turning). The angle(s) of the neurites tips (θ tip) was subtracted from the angle(s) initiating from the soma (θ root) of the same DRG neuron to yield the angle(s) of turning relative to the electric field direction (θ deflection).

1.3 Results

1.3.1 DRG spontaneous regeneration assessment after axotomy

Axotomy and axon injuries initiates a retrograde signaling cascade that activate the transcription and translation of genes associated with regeneration [36], [37]. This pro-regenerative response is required for neurite regeneration [38], [39], [40]. To determine the spontaneous regeneration response of our axotomized DRG cells under our *in vitro* conditions, we chose to assess neurite outgrowth over a scale of specific endpoints with immunohistochemistry staining and NeurologyJ analysis. Utilizing a single batch of mice, spontaneous regeneration was assessed a two different series of set time points (Figure 1-3). Spontaneous regeneration was quantified at 4, 8, 12, and 24 hours after axotomy to determine the critical time point after axotomy that would yield reliable morphological data compatible for high content screening with NeurophologyJ (Figure 1-3 (a and b)). It was noted that DRG did not undergo spontaneous regeneration one hour after axotomy (Figure 1-3 (c and d)) which agrees with previous observations [41]. Increasing spontaneous regeneration was seen by 24 hours and up to 120 hours after the first axotomy (Figure 1-3 (c and d)). However, extensive neuronal networking was seen by 48 hours making analysis of individual cells not compatible with high content screening (Figure 1-3 (c)). It was also noted that there was no statistical differences between the neurite length resulting from the first series of measured time points (Figure 1-3 (b)) and the second series of measured time points (Figure 1-3 (d)) at the 24 hour time mark indicating consistency in the experimental set-up. Therefore, it was determined that 24 hours would be used as the set time between

stimulation and high content screening analysis for action potential like stimulation protocols.

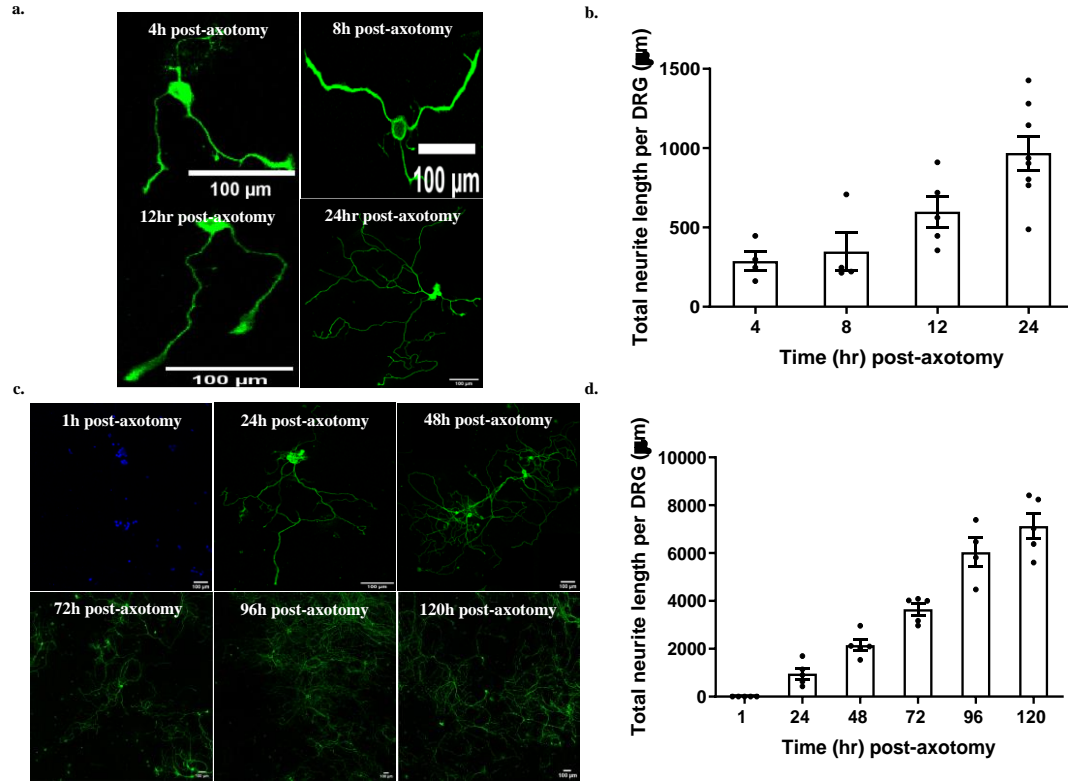


Figure 1-3 DGR spontaneous regeneration assessment after axotomy. (a and c) Cells were fixed and stained with DAPI and β -III-tubulin, a neuronal marker, after axotomy at specified time endpoints. (b and d) Neurite length was assessed with NeurphologyJ at each time point. Data shown as averaged total neurite length per DRG (μm) with SEM.

1.3.2 Verification of finite-element modeling for DRG stimulation

The finite element analysis with a 0.2 V simulated excitation was represented in the 11 x 10 mm chamber well (Figure 1-4 (a)). Two time points ($T=0.2$ and $T=0.6$ milliseconds) were chosen to represent the potential energy (Figure 1-4 (b)) within the chamber well (Figure 1-4 (c-d)). Furthermore, Figure 1-4 (c-d) demonstrated that potential scaled with the excitation amplitude over time. Figure 1-4 (b) showed the normalized potential (V) as

an action potential-like pulse for 1 second in each of the 7 regions with a 0.2 V excitation.

From this data, the time averaged potential (V) of each of the 7 regions was calculated in

MatlabR2019b using Simpson rule and shown in Table 1-4.

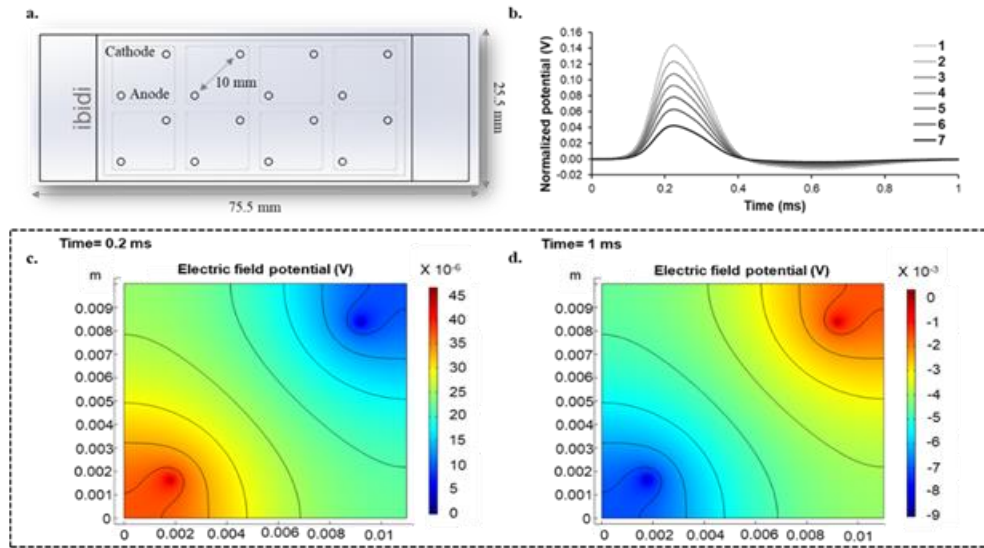


Figure 1-4 (a) Electrodes were fitted from the top of the lid to the bottom of the chamber with a 10 mm diagonal distance between the anode electrode and the cathode electrode. (b) Resulting potentials with 0.2 V excitation for each of the seven regions over a 1 ms time period. (c-d) Simulation with 0.2 V excitation across the chamber well represented at two chosen time points ($T = 0.2$ ms and $T = 1$ ms) to show electric potential change (colored bar) as the electric potential (V) traveled from the anode and cathode electrode.

Table 1-4 Time averaged potential (V) of each region was calculated from the 0.4 V normalized potential.

| Region | Time averaged potential (V) |
|--------|-----------------------------|
| 1 | 0.39 |
| 2 | 0.33 |
| 3 | 0.29 |
| 4 | 0.25 |
| 5 | 0.21 |
| 6 | 0.17 |
| 7 | 0.11 |

1.3.3 Assessment of post-axotomy recovery time and electrical stimulation on DRG structural regeneration

To see the effects of post-axotomy recovery time before the application of action potential-like stimuli, axotomized DRG were allowed to recover two hours, three hours, or four hours before the start of stimulation. Confocal images showed that there was healthy spontaneous (CTL) and stimulated DRG regeneration (Figure 1-5 (a-c)). The stimulation was done with 0.2 V, 0.4 V, or 0.6 V applied amplitudes with a set frequency of 250 Hz. Axotomized DRG that had two hours to recover had significant neurite regeneration and increased neurite endpoints with 0.2 V and 0.4 V applied amplitudes at 250 Hz (Figure 1-5 (d and e)). No significant increases were seen in neurite length nor neurite endpoints with the 0.6 V applied amplitude (Figure 1-5 (d and e)). With a three hours post-axotomy time, only a significant increase was seen with neurite length with the applied 0.6 V (Figure 1-5 (f)). However, an applied 0.2 V, 0.4 V, and 0.6 V significantly increased neurite endpoints

(Figure 1-5 (g)). For the four hour post-axotomy recovery time, significant structural regeneration was seen with DRG simulated with an applied 0.2 V (Figure 1-5 (h and i)).

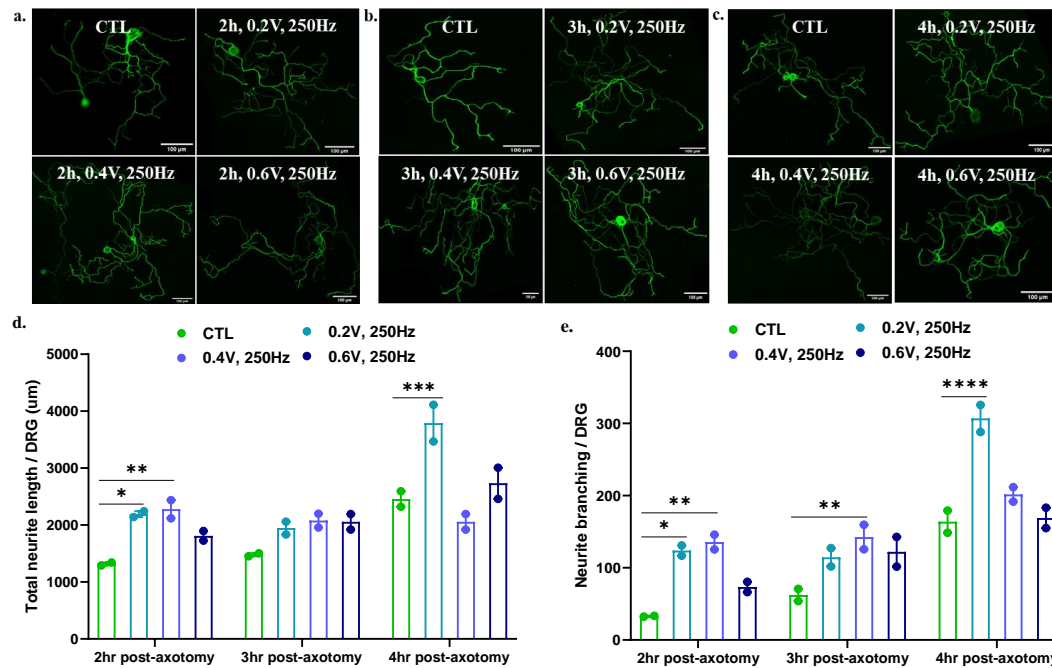


Figure 1-5 Total neurite length and endpoints per DRG significantly increased with a two hour post-axotomy stimulation start time using an applied 0.2 V or 0.4 V at 250 Hz. (a-c) Cells were fixed and stained with β -III-tubulin, a neuronal marker, 24 hours after each stimulation parameter. (d) Cell stimulated with 0.2 V or 0.4 V at 250 Hz showed significant neurite regeneration and (e) increased neurite endpoints with a two hour post axotomy recovery. (f-g) Significant neurite regeneration was seen with an applied 0.6 V while an increased number of neurite endpoints was seen with an applied 0.2, 0.4, and 0.6 V amplitude with the three hours post-axotomy stimulation. (h-i) Significant structural regeneration was seen with an applied 0.2 V with the four hour post-axotomy stimulation start time. Statistical analysis based on one-way ANOVA

1.3.4 The effects of frequency on DRG structural regeneration with action potential-like stimuli

To investigate the effects of action potential-like stimulation on DRG regeneration, axotomized DRGs were stimulated with a specific field strength and frequency for one hour. DRGs had extensive neurites before axotomy (Figure 1-6 (a)) and these neurites were completely removed after axotomy (Figure 1-6 (b)). Spontaneous neurite regeneration occurred with the non-stimulated control (Figure 1-6 (c)). Stimulated neurite regeneration also occurred under different field strengths and frequencies (Figure 1-6 (d-g)).

In our initial screening, we tested three different applied field strengths, 20 V/m, 40 V/m or 60 V/m at three different frequencies, 20, 125 or 250 Hz. 60 V/m field strength had no effect on total neurite length nor neurite branching per DRG at 250 Hz (data not shown). In addition, 125 Hz had no effect on total neurite length nor neurite branching per DRG (data not shown). Averaged data from multiple wells per region showed that stimulation with field strengths of 20 V/m or 40 V/m at 20 Hz or 250 Hz had inhomogeneous, spatial distribution with a higher extent of regeneration in the regions away from the electrode regions (Figure 1-6 (h and i)). A nearly homogenous distribution of neurite length (Figure 1-6 (h)) and branching (Figure 1-6 (i)) with minor variation was seen across different regions of the control groups. It was also noted that intra-well variation seemed to increase with electric field strength, especially with 0.4 V, at both frequencies for neurite length and neurite branching (Figure data not shown).

For whole well analysis, ordinary one-way ANOVA between the control and stimulated cells was conducted to compare the effects of applied field strength and frequency on DRG neurite length (Figure 1-6 (j)) and branching (Figure 1-6 (k)). There was a significant effect that action potential-like stimulation had on neurite length at the $p < 0.05$ [$F(4, 36) = 30.55$] and neurite branching at the $p < 0.05$ [$F(4, 36) = 13.45$] across all conditions (Figure 1-6 (j and k)). P value were shown in Table 1-5.

Table 1-5 One-way ANOVA p-values for all stimulation conditions in comparison to the control.

| Stimulation condition | P value for total neurite length | P value for neurite branching |
|-----------------------|----------------------------------|-------------------------------|
| 20 Hz, 0.2 V | <0.001 | 0.0122 |
| 20 Hz, 0.4 V | <0.001 | 0.0003 |
| 250 Hz, 0.2 V | <0.001 | 0.0114 |
| 250 Hz, 0.4 V | <0.001 | <0.001 |

Post hoc comparisons using two-way unpaired t test indicated that the mean score for the effects of field strength on neurite regeneration (Figure 1-6 (j)) and branching (Figure 1-6 (k)) was significantly higher than the effects of frequency from action potential-like stimulation. The mean and standard deviation for each condition were shown in Table 1-6.

Table 1-6. T test mean and standard deviation (SD) for all stimulation conditions.

| Stimulation condition | Total neurite length | | Neurite branching | |
|-----------------------|----------------------|-----|-------------------|----|
| | Mean | SD | Mean | SD |
| 20 Hz, 0.2 V | 1796 | 186 | 73 | 23 |
| 20 Hz, 0.4 V | 2202 | 89 | 130 | 18 |
| 250 Hz, 0.2 V | 1954 | 239 | 86 | 40 |
| 250 Hz, 0.4 V | 2309 | 222 | 145 | 31 |

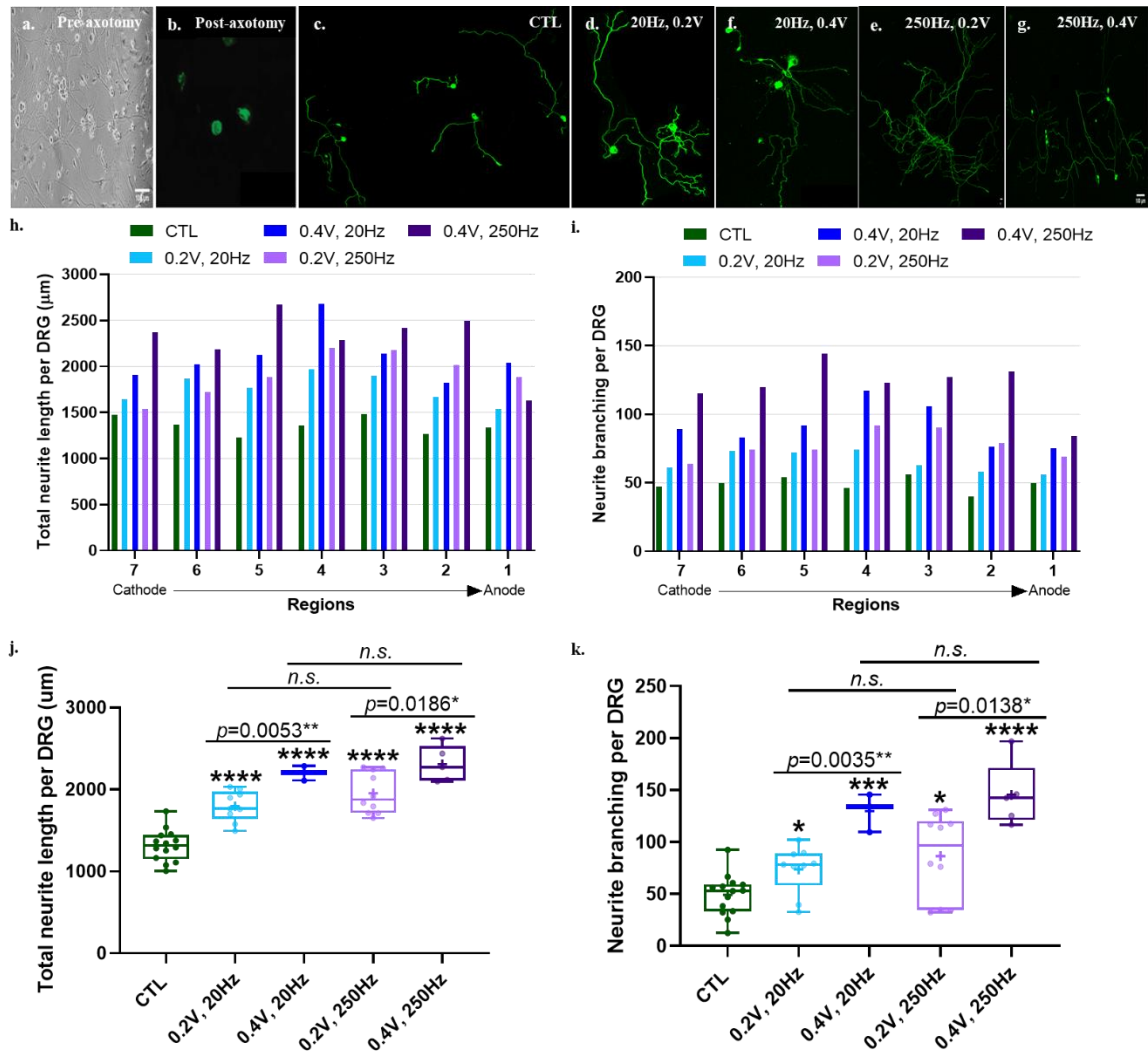


Figure 1-6 Action potential-like stimulation significantly increased total neurite outgrowth and neurite branching. Brightfield images of the DRG culture were taken before axotomy

(a). Cells were fixed and stained with β -III-tubulin, a neuronal marker, after axotomy (b) and stimulated 24 hours afterwards with 20 V/m or 40 V/m field strengths at 20 Hz or 250 Hz frequencies (c-g). Averaged data from multiple wells per region showed inhomogeneous regeneration (h) and branching (i) for the stimulated DRG and nearly homogenous neurite regeneration (h) and neurite branching (i) for the control groups. More regeneration (h) and branching (i) was noted in regions away from the electrodes. Whole well analysis for each stimulation condition showed that action potential like stimulation significantly increased neurite regeneration (j) and branching (k) for all conditions. Further statistical analysis showed that field strength rather than frequency had a greater effect on neurite length (j) and branching (k). No significance was indicated with n.s. Scale bar shown as 100 μ m for the brightfield and confocal images.

1.3.5 DRG neurite orientation after action potential-like stimulation

To examine the orientation at 24 hours post-electrical stimulation, DRG cells were quantified according to neurite deflection (θ deflection) or orientation of their tips (θ tips) at an angle of 0° to 360° to the x-axis where the complement alignments with the electric field would be 225 ° for the anode and 45 ° for the cathode. Representative histograms depicting cell alignment were shown in Figure 1-7. Non-stimulated cells (CTL) did appear to align towards the cathode 45 ° as evidenced by the downward-line histogram data fit (Figure 1-7 (a)). By comparison, the orientation of the neurite tips showed a symmetric distribution indicating no alignment (Figure 1-7 (g)). For the stimulated cells, 20 Hz at

0.4 V and 250 Hz at 0.6 V showed statistical differences in distribution from the non-stimulated cells using the Kolmogorov-Smirnov test (Figure 1-7 (c and f)). However, there is no trend indicating that neurite show a preference to the anode or the cathode based on alignment as evidenced by the Gaussian best fit lines (Figure 1-7 (c and f)). Furthermore, no statistical differences in distribution were seen in the orientation of the neurite tips with any of the applied action potential-like stimuli in comparison to the non-stimulated cells (Figure 1-7 (g – l)).

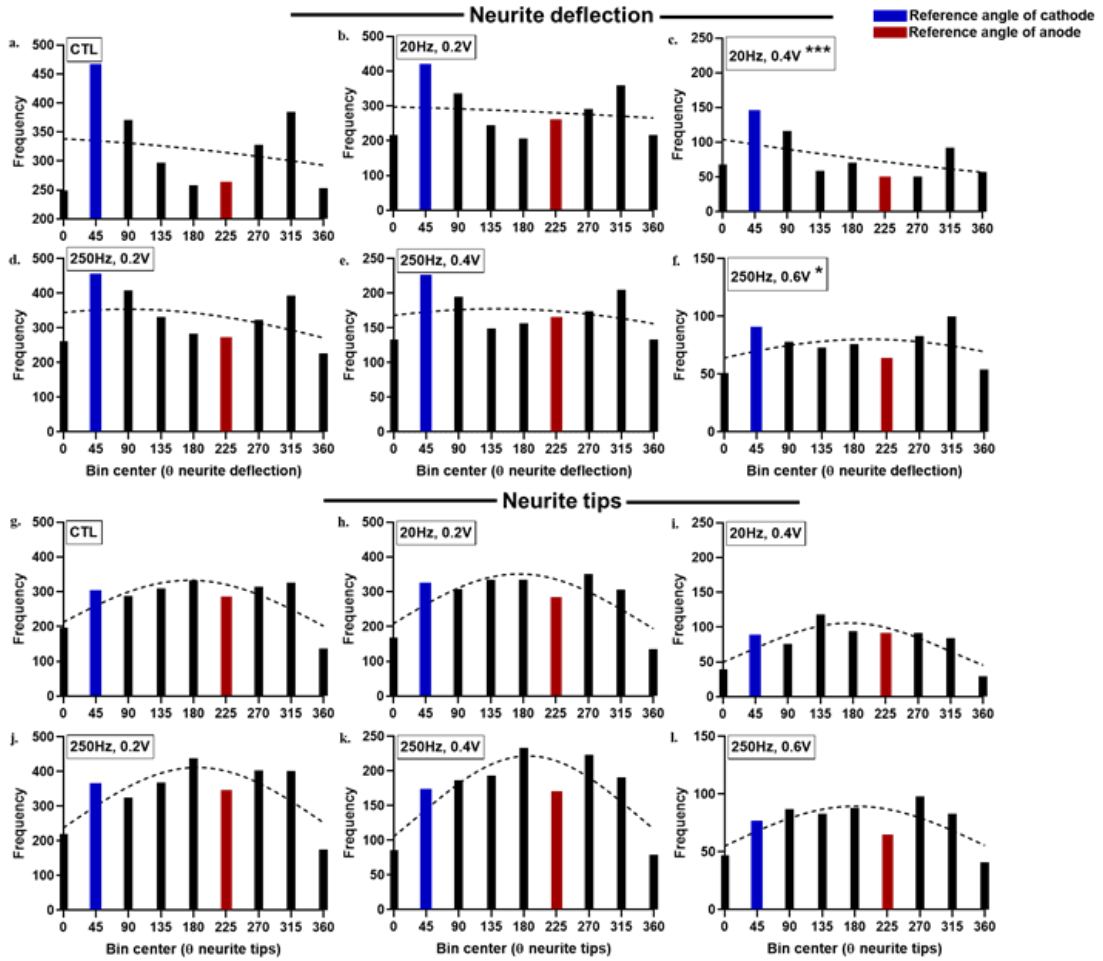


Figure 1-7 No neurite orientation seen with DRG neurites after action potential-like stimulation. (a-f) Neurite deflection across all stimulation parameters shown with Gaussian best fit lines. (g-l) Orientation of neurite tips shown across all stimulation parameters shown with Gaussian best fit lines. Cells were analyzed for alignment 24 hours post stimulation with ImageJ.

1.4 Discussion

Utilizing physiological levels of electrical stimulation after nerve injury may have a significant impact in improving peripheral nerve regeneration in people suffering from peripheral nerve damage [41], [42], [43]. Under normal physiological conditions, DRG neurons exhibit spontaneous regenerative properties that can result in functional sensory recovery [44]. However, in the case of nerve-injury, spontaneous regenerative properties are limited by the extent of the nerve gap, neuroma, and scar tissue formation [44]. Electrical stimulation in the forms of direct current, alternating current, or pulsed currents have been shown to elicit neurite growth and regeneration. Therefore, exploring *in vitro* electrical stimulation protocols using peripheral sensory neurons is an important approach in identifying applicable electrical parameters that induce structural regeneration in injured nerve cells. However, one area that is underexplored is the effects that biologically based action potential-like stimulation has on DRG regeneration after nerve-injury. In the present study, we describe an innovative action potential generator board to identify specific stimuli parameters for encouraging peripheral neurite regeneration after axotomy.

We first assessed the electric field created by the action potential generator board in our electrical chamber set-up by utilizing a finite-element model. Given that the distance between the anode and cathode electrodes was 1 cm, we programmed the action potential generator board to have a peak-to-peak amplitude of 0.2 V for the simulation with a given applied field strength of 20 V/m. Thus, an amplitude of 0.4 V produced a field strength of 40 V/m. The finite-element model's simulation with 0.2 V showed an expected decrease

in calculated time averaged potential across the 7 regions. The calculated time averaged potential values was based on our electrical stimulation set-up that created a non-uniform electric field. This heterogeneous variance in time averaged potential was unique to other electrical stimulation studies that utilized parallel electrode plates and rectangular chamber geometry to obtain uniform voltages and electric fields across their stimulation chamber set-ups [45], [28], [4], [1]. The advantage of our non-uniform electric field was the ability to observe the effects of spatial distribution of neurite regeneration and neurite branching across the well. Our results indicated that there was an almost homogenous distribution of regeneration for the neurite lengths and branching of the controls with only minor variations across the whole well. However, non-homogeneous spatial distribution with a higher extent of regeneration and branching was seen in regions that were not near the electrode containing regions. Additional analysis revealed that intra-well variation seemed to increase with electric field strength with both frequencies. From these results, it was concluded that electric field strength positively influenced DRG structural regeneration with action potential-like stimulation.

To further explore the effects of field strength and frequency of action potential-like stimulation on DRG regeneration, the combinations of 0.2 V or 0.4 V at 20 Hz was applied as a low frequency electrical stimulation parameter. Electrical stimulation at 20 Hz has been shown to promote DRG outgrowth *in vitro* and *in vivo* through upregulation of injury or regeneration-associated genes [16], elevation of adenosine 3',5'-cyclic monophosphate (cAMP), a second messenger that regulates neuron plasticity [6], [26],

possible elevation of calcium [7], and upregulation of matrix metalloproteinase-2 (MMP-2) [7]. For our electrical simulation set-up, we observed that both applied electric field strength of 0.2 V or 0.4 V at 20 Hz significantly increased DRG structural regeneration. These results were expected given that 20 Hz with a stimulation duration of 1 hour has been shown to significantly increase neurite outgrowth 24 hours to 3 weeks post-stimulation [5], [11], [7]. Higher stimulation frequencies of up to 200 Hz were shown to enhance neurite growth *in vitro* [28],[1] while *in vivo* nerves had a more mature structure, increased myelinated fibers, and improved muscle recovery [27], [46]. For our max frequency, we utilized 250 Hz with applied field strengths of 0.2 V or 0.4 V. Our results showed that action potential-like stimulation of with 0.2 V or 0.4 V at 250 Hz also significantly improved DRG structural regeneration. Additionally, we did see a similar concordance between neurite length and neurite branching at the 20 Hz 250 Hz with both applied electric fields. In terms of electrical stimulation, cortical neuron cultures stimulated with a biphasic 250 Hz waveform with an applied 0.75 V field strength had increased neurite outgrowth and branching with conductive 3D polymer electrodes [47]. In another study, PC12 cells electrically stimulated with 100 Hz with an applied 100 V/m electric field together with 100 ng/ml NGF increased neurite length but reduced neurite branching [48]. It was suggested that electrical stimulation in combination with NGF affects neurite elongation, not neurite initiation [48]. This effect is due to NGF-induced phosphorylation of ERK1/2, increased activity of protein kinase, and increased expression of the EGR1(Early growth response 1) gene, all of which are associated with neurite outgrowth

[48]. NGF is required for survival and differentiation of DRG *in vivo* and for survival for embryonic DRG *in vitro* [49]. Increased branching as a result of both frequency conditions and electric field strengths in our studies warrants further investigations.

We showed that both high and low frequencies with field strengths of 20 V/m and 40 V/m improved DRG regeneration and neurite branching in comparison to spontaneous regeneration controls. We also noted that increased DRG structural regeneration was dependent on a higher field strength with action potential-like stimulation rather than frequency given the values from the whole well analysis. These observations also confirmed that an applied electric field strength of 20 V/m or 40 V/m corresponded to increased DRG regeneration in any one direction according to the direction of the electric field. Conflicting evidence has shown that the electric field strength may or may not affect DRG neurite outgrowth. For example, an applied electric field strength of 50 V/m [50] did not result in any changes to DRG morphology or neurite outgrowth. However, in another study, an applied field strength of 50 V/m increased neurite outgrowth two-fold with stimulation alone or when co-cultured with unstimulated Schwann cells [45]. The study also found that co-culturing with Schwann cells pre-stimulated with 50 V/m of direct current further increased neurite outgrowth by 1.2 fold compared to electrical stimulus alone or co-culture with unstimulated Schwann cells [45]. Another study indicated that an applied 17.86 V/m increased DRG directional outgrowth at 20 and 200 Hz [1]. Our whole well analysis results indicated that maximum neurite regeneration and neurite branching with action potential-like stimulation was seen at 40 V/m at either frequency.

1.5 Conclusions

Neurite outgrowth can be promoted electrotactically in peripheral neurons: this plasticity has crucial implications for neuroengineered rehabilitation of peripheral sensory pathways. With the vast number of electrical stimulation protocols available, a significant challenge lies in determining optimal stimulation parameters that are compatible with increased neurite growth. An underexplored area is the specific effects of action potential-like electrical stimulations, that is, signals with enhanced physiological realism, akin to when sensory DRG neurons convey the information transduced by mechanoreceptors on neurite structural regeneration. Unlike other methods using direct and alternating electrical current stimulation and uniform electric fields, our stimulation method embeds the unique spatiotemporal features of efferent and afferent signals in the peripheral nervous system and allows for the analysis of those biomimetic stimulations across a range of electric field strengths.

1.6 Future directions

Utilizing the action potential generator board to its full potential in applying direct current, alternating current, and pulsed current stimulation protocols with different voltages and different stimulation frequencies to compare and verify the current findings that our action potential-like stimulation protocols gave with our axotomized, DRG protocol. After verifying whether action potential-like stimulation is more realistic or comparable for regenerating axotomized DRG compared to already established stimulation protocols, we would like to utilize a commercial microfluidic neuronal platform for neuron regeneration

to co-culture DRG and mouse skeletal muscle cells in separate channels connected by micro-sized channels. This microfluidic chamber would be fixed to a substrate with gold printed electrodes. This substrate would allow us to stimulate the DRG with action potential-like stimuli after axotomy. We would then be able to assess regeneration and reinnervation of the DRG with the muscle cells by the formation of motor neuron axon terminals. We would also characterize motor neurons formation via live video analysis to measure spontaneous myotube contraction versus motor neuron stimulated contraction with action potential-like stimulation of the DRG. This future work would allow us to establish the efficacy of action potential-like stimulation compared to other electrical stimulation protocols. Additionally, we would be able to establish a platform to study the effects of action potential-like stimulation *in vitro* nerve intervention and function on skeletal muscle after axotomy. This approach would allow for a simplified platform for screening of potential therapeutic applications for peripheral nerve injuries and or amputees.

2 INVESTIGATION OF NEURON ACTIVITY AND CONNECTIVITY USING MULTI-MICROELECTRODE ARRAYS

2.1 Introduction

Importance of understanding neuronal activity: During development, neurons extend their dendritic and axonal arborizations to form synaptic connections. Throughout adulthood, neural activity will be communicated through synaptic connections via action potentials. Network activity consist of individual neurons, mixed neuron populations, or anatomically segregated tissue regions that are crucial in constructing, processing, and allowing for the flow of encoded neuronal activity from sensory stimuli and motor actions, both of which are essential for higher-order cognitive and motor function [51], [52]. The precise network of connections between neurons includes a division of labor between excitatory and inhibitory neurons [53]. Excitatory neurons make up the largest proportion of cortical cells which are essential for long-range connections and for the integration of ascending (sensory stimuli) and recurrent information across wide regions of the brain [53]. In contrast, the minority population of inhibitory interneurons control the flow of neuron activity by keeping excitation in check as well as locally modulating the timing, shape, and coordination of the network activity [53], [54], [55]. The delicate balance between

excitatory and inhibitory actions is important for normal brain functions and its impairment has been indicated in various neurological disorders.

Neuronal connectivity can have several meanings within the developed network activity. For example, anatomical connectivity is when neurons are synaptically connected [56]. Functional connectivity is when nerves have anatomical connectivity and are able to fire together or have correlated activity [57]. Effective connectivity is understood as dynamic or activity-dependent, and requires a model of interactions (Friston., 2011). Even with these definitions of connectivity [57], brain function evolves over the lifetime of the organism, meaning that processes undergo constant rewiring [59] and neuronal loss with or without adult neurogenesis [60]. This evolution in brain connectivity is identified as brain plasticity which allows an individual to adapt to dynamic environments through the strengthening, weakening, pruning, or adding of synaptic connections [61], [62]. Plasticity consists of a balanced interplay of mechanisms that promote change at the synaptic sites versus those that promote homeostatic plasticity [63]. For example, long term potentiation, a high frequency stimulation of a chemical synapse, strengthens synaptic connections [64] while long term depression weakens them through the dephosphorization of α -amino-3-hydroxy-5-methyl-4-isoxazolepropionic acid (AMPA) receptors that cause their movement away from synaptic junctions [65]. Both of these events take place at the synapse level and are critical for the formation of new memories with strong evidence pointing to the fact that learning and synaptic activity are tightly linked [66].

Studying function and connectivity of neurons has involved advancements in genetic markers [67], immunostaining [68], optical and electro-optical methods [69], computational tools [70], and electrophysiology [71] that can identify neuron types, describe their molecular machinery, explain network wiring, understand neuronal coding, and characterize the function of specific brain regions. When using electrophysiology techniques with *in vitro* cultures, connected neuronal networks are characterized with periods of synchronized firing known as network bursts [72]. These synchronized bursts within the culture occur spontaneously and are initiated and directed by spatio-temporal summation of synaptic events [73]. The functional connectivity between neurons in the network forms the basis of firing activity patterns which are strongly shaped by the structural properties of that network [72]. Three specific approaches, patch clamp, microelectrode arrays, and functional magnetic resonance imaging, will be further discussed as methods to evaluate neuronal activity.

Approaches to assess neuronal activity: Neurons are electrically-active cells that can be assessed by various types of electrophysiological recording techniques that measure their intercellular or extracellular potential dynamics [74]. Intracellular recordings can be classified into patch-clamp techniques which captures the intracellular activity of single neurons with high signal-to-noise ratio via a giga-ohm seal between the neuron's plasma membrane and the blunt tip of a heat-polished glass of quartz micropipette electrodes [75], [76], [77]. Cell-attachment patch configuration allows for the study of single channel currents or a summed current of several channels of cell firing activity without disturbing

the cell membrane or the cytosolic content [78]. However, the membrane potential cannot be controlled given that the lack of seal rupture restricts the intracellular electrical access [78]. Therefore, only the patch membrane potential relative to the cell's resting potential can be controlled via the magnitude of the seal's resistance and/or whether the recording electrode is current or voltage clamped [78]. Cell attached patch configuration can be used to measure single ion channel currents, cell firing (action potentials), and synaptic potentials within the neuron [78]. Two other configurations of the cell-attached patch, the perforated patch and whole-cell patch, are also non-invasive configurations that also utilize the giga-ohm seal [78]. To increase the electrical access, antibiotics or antifungal agents are used for the perforated patch configuration to form monovalent ion permeable pores in the neurons membrane [79], [78]. These pores exclude large ions such as calcium which minimalizes cell disruption. However, the perforated patch technique has higher electrical noise, loss of single channel assessment, and patch instability [78]. The perforated patch measures the sum of activity of ion channels and is ideal for recording whole cell current without disturbing second messenger signaling cascades [78]. Whole cell configuration involves rupturing the membrane with strong suction to allow the pipette to be continuous with the cell cytoplasm [78]. This configuration allows for continuous measurements of the cell's membrane potential but may cause the cytosol to dialyze and/or alter the activity of second messengers [78].

Given that ion channels are essential for neuronal signal transduction, neuronal excitation, electrolyte transportation, and muscle contraction through efferent pathways,

the patch clamp technique is considered the gold standard for intracellular recording research (Yajuan et al., 2012). This technique has been employed in studying the properties of ion channel function and modulation in many diseases including epilepsy (Morris et al., 2017), pain (Bell & Dallas, 2018), and peripheral neuropathies (Bianchi et al., 2019). However, patch clamp techniques are known to be expensive, have high labor cost, and have low throughput, all of which has been improved through the advancement in automated patch clamp systems [80]. Patch clamp has been utilized to study synaptic connectivity between cortical neurons (Jouhanneau et al., 2018), (Jouhanneau et al., 2015) but is limited by its ability to record the activity of a single neuron. Some studies have been able to record 8-12 neurons from brain slices through paired-recordings of simultaneously patched clamped neurons [81], [82]. However, this is extremely challenging and requires specialized recording setups and technical skills.

Microelectrode arrays (MEAs) are advantageous since they provide a high-throughput evaluation of extracellular neuronal activity and synaptic connectivity from a cultured neuronal population (Quiroga et al., 2013). MEAs are an instrument platform used for the purpose of monitoring extracellular, spontaneous firing activity of *in vitro* neurons over an extended period of time with no destructive effects [83]. MEAs contain a large number of planar electrodes that detect local field potentials generated by either spontaneous or evoked firing events [83]. Thus, potential differences across recordings with reference electrodes at rates of 10 – 60 kHz detect action potentials, known as spikes, when the sample values deviate significantly from the background noise [83]. This

resulting spiking activity can be quantified as parameters that refer to spiking activity, neuronal activity, and network activity [84], [85], [86]. The principle behind extracellular MEA recordings is the action potential or “spike” produced by currents that induce flow in the extracellular space around the active neuron (Heinricher, 2004). The extracellular media has a low uniform resistance and is considered the “volume conductor” (Heinricher, 2004). When the axon is in the resting state, the membrane potential is uniform, meaning there is no current flow. Upon depolarization, the current will flow somewhere along an active area of the membrane. As the current flows inward at the active site, the electrode adjacent to the active site will be negative and will result in a current “sink” (Heinricher, 2004). Inactive sites of the depolarizing axon will act as the “source” of current since the current flows out, resulting in a positive signal to the adjacent electrode. Thus, an extracellular spike will appear as a positive-negative-positive waveform with MEA recordings while an intracellular recording with a patch clamp would appear as a positive, monophasic waveform [88], [87]. Differing geometries of the recorded spike waveform with MEAs will be seen depending on the layout of the dendrites and the location of the electrode which can enhance or attenuate the positive phase [87]. A main problem seen with MEAs is that they are fabricated with materials that are substantially different to the physical and chemical properties of the brain. For example, the neurons of the brain used to softer surfaces with a stiffness moduli between 3-200 kPa [89]. Thus neurons have a difficulty in attaching to the stiffer substrate of MEAs resulting in micromotion that can strain the neuronal network [90], [91]. An additional disadvantage of *in vitro* MEAs is

unlike patch clamp techniques, MEAs cannot record or stimulate a single neuron due to their low spatial resolution thus decreasing the complexity of signals that could be sent to other cells through a MEA electrode [92]. *In vivo* implantation of MEAs into the brain leads to chronic biological responses such as neuronal death, glial scarring, and a decrease in functioning electrodes [93].

Magnetic resonance imaging (MRI) is a well-known, non-invasive procedure used for functional investigation of the human brain. MRI detects and analyzes magnetic resonance energy from specific points in a volume of tissue resulting in images of the brain structure with superb detail. However, MRI does not reveal anything about neuronal activity, but rather looks at the brain's energy metabolism [94]. Given that active neurons require high amounts of energy, known as adenosine 5'-triphosphate (ATP) [95], areas of high neuronal activity results in significant differences in the concentration of oxygenated and deoxygenated hemoglobin in the arterial blood and venous outflow, respectively [96]. These differences are magnetic-field inhomogeneity's that can be assessed with the blood-oxygenated-level-dependent (BOLD) method [97], [98]. Functional MRI (fMRI) uses the BOLD method to measure neuronal activity indirectly [97]. The BOLD method along with fMRI can capture intrinsic oscillation, excitatory postsynaptic potential, inhibitory postsynaptic potential, action potential generation and propagation along the axon, and release, binding, and reprocessing of neurotransmitters [97], [99], [98]. These captured localized changes and perturbations cause an increase in the BOLD results. However, conclusions cannot be drawn as to which of these neuronal activities singularly or in

combination are causing the changes in BOLD. Another drawback of fMRI and the BOLD method is that it has slow temporal resolution [100]. Given that fMRI images changes in blood-flow responses, the blood flow response is delayed half of a second after neuronal activation [101]. This equates to the second-scale resolution of the BOLD method being too long to evaluate the spatiotemporal progression of neuron activity since increased BOLD activity does not provide any knowledge about the temporal sequence of neuronal activation due to cognitive actions across the brain regions [100].

Table 2-1 Approaches used at the single cell level (patch clamp), whole culture level (MEA), and whole organ level (functional MRI) to assess neuronal activity.

| Approach | Configuration | Method | Pros | Cons | Ref. |
|-----------------------|---|---|---|---|-------|
| <i>Patch clamp</i> | Cell-attached patch  | <ul style="list-style-type: none"> Giga-ohm seal Single ion channel suction | <ul style="list-style-type: none"> Study single channel or summed channel currents Study action potentials and synaptic potentials | <ul style="list-style-type: none"> Membrane potential cannot be controlled Lack of seal rupture restricts the intracellular electrical access | [78] |
| | Perforated patch  | <ul style="list-style-type: none"> Giga-ohm seal Pores with antibiotic or antifungal drugs | <ul style="list-style-type: none"> Increased electrical access No disturbances to second messenger signaling cascades | <ul style="list-style-type: none"> Higher electrical noise Loss of single channel assessment Patch instability | [78] |
| | Whole-cell patch  | <ul style="list-style-type: none"> Giga-ohm seal Membrane is ruptured with strong suction | <ul style="list-style-type: none"> Continuous measurements of the cell's membrane potential | <ul style="list-style-type: none"> Dialysis of the cytosol Altered activity of second messengers signaling cascades | [78] |
| <i>MEA</i> | Extracellular action potential recording  | <ul style="list-style-type: none"> Local field potentials generated by spontaneous or evoked firing events detected by substrate with printed electrodes | <ul style="list-style-type: none"> Used to study network activity Can input electrical signals and/or utilize pharmaceutical drugs to study evoked changes in network activity High throughput evaluation of network activity | <ul style="list-style-type: none"> Cannot study single cells Manufactured materials different from brain tissue Micromotion detachment from hard substrate causes disruptions in network activity | [83] |
| <i>Functional MRI</i> | Blood-oxygenated-level-dependent (BOLD) method  | <ul style="list-style-type: none"> Visualizes brain's energy metabolism Active neurons require high amounts of ATP | <ul style="list-style-type: none"> Non-invasive procedure Captures intrinsic oscillations, excitatory postsynaptic potentials, inhibitory postsynaptic potentials, action potential generation, propagation along the axon, and release, binding, and reprocessing of neurotransmitters | <ul style="list-style-type: none"> Cannot distinguish between intrinsic oscillations, excitatory postsynaptic potentials, inhibitory postsynaptic potentials, action potential generation, propagation along the axon, and release, binding, and reprocessing of neurotransmitters | [102] |

MEAs are well suited for *in vitro* manipulation of neuronal cultures for studying the network activity of neurons under normal and disease conditions [103]. Furthermore, MEAs have been widely used to measure basic network properties such as synchronized neuronal activity [104], oscillatory behavior of neuronal populations [105], and to manipulate synchronized network bursting in a neural networks [106]. To monitor the formation of stable neuronal circuits, microelectrode arrays will be used to study two behaviors of neuronal activity, spontaneous activity and stimulus induced activity. Thus, our first goal is to look at spontaneous neuronal activity variations of different batches. We will utilize dissociated cortical neurons from mice for temporal analysis to examine parameters categorized into three levels of neuronal activity; spiking activity, neuronal excitability and neuronal connectivity. This temporal analysis will allow us to determine a stable, development time window of our dissociated cortical neurons from which we can pool the MEA parameters. Pooled MEA parameters will then be further analyzed using descriptive analysis to compare variation across different batches and determine the most robust parameters that describe a stable MEA phenotype. For the second goal, we will perform pilot studies to establish MEAs as a mechanistic tool to observe the effects that different electrical stimulation protocols have on directly evoked and synaptic responses for future comparisons to diseased phenotypes. We will also utilize pharmacological drugs that inhibit the modulatory effects that GABAergic neurons have on neuronal networks and as well as drugs that inhibit excitatory neuron neurotransmitter receptors to confirm the evoked activity from our stimulation protocols. We will also look at a single batch

medium spiny neurons from human induce pluripotent stem cells (iPSCs) to observe the neural activity of a pure culture composed of GABAergic inhibitory neurons in comparison to dissociated cortical neurons which are a mixed population of excitatory and inhibitory neurons. Thus, understanding the mechanisms by which neuronal networks self-regulate their activity is essential for comparing emergent firing dynamics, such as under spontaneous conditions or stimulated conditions. This will build the necessary foundation in the future to further mechanistically investigate changes in neuronal activity patterns under normal and pathological conditions.

2.2 Experimental Methods

2.2.1 Primary neuronal cultures

Primary cortical/striatal mouse neurons: Brains from mice pups at 1 postnatal day old (B6C3 strain) were used to prepare the primary neuronal culture. Briefly, pups were quickly decapitated, whole brains were removed and stored in ice-cold dissection media [1 mM sodium pyruvate, 10 mM HEPES, 0.1% glucose in HEPES-buffered saline (HBSS), pH=7.4)]. The meninges were completely removed under a dissection microscope. Brain tissue was then digested with 1 mg/ml collagenase/dispase in dissection medium at 37°C for 20 minutes. At the end of incubation, digested tissue was further incubated at room temperature for 5 minutes with 0.04 mg/ml deoxyribonuclease I (DNase I, Sigma Aldrich, USA). After the DNase incubation, the supernatant was removed and the tissues were triturated with a widebore P1000 in warmed, fresh neuronal culture medium (2 mM glutaMAX and 1% B27). The debris were allowed to settle for 2 minutes and then the supernatant containing the dissociated cells was transferred to a new tube. The supernatant was then centrifuged at 200 x g for 2 minutes and the pellet was resuspended in appropriate volume of neural basal medium for seeding. About 2.5×10^5 viable cells were plated per well of a 24-well MEA plate previously coated with 0.1 mg/ml polyethyleneimine (PEI, Sigma Aldrich, USA). Half the medium was changed every 3-4 days and cells were cultured at 37 °C with 5% CO₂. All animal procedures were approved by the Institutional Animal Care and Use Committee of FAU and in compliance with the National Institutes of Health Guidelines for the Care and Use of Laboratory Animals.

Medium spiny neurons (MSNs) from iPSCs: Age and sex-matched iPSCs from an apparently healthy individual (GM23476, female, 20 years old at sampling, RRID:CVCL_T841) was obtained from MIGMS cell repository through Coriell Institute for Medical Research. iPSCs were cultured in Matrigel-coated plates with mTeSR™1 complete medium (STEMCELL Technologies). The differentiation of iPSCs to neuronal stem cells was performed using the STEMdiff™ SMADi Neural Induction Kit based on the rosette formation and isolation method according to the manufacture's instruction (STEMCELL Technologies). After differentiation, neuronal stem cells were further cultured and expanded in the complete STEMdiff™ Neural Progenitor Basal Medium (STEMCELL technologies). Neuronal stem cells expansions were limited to 4 passages. The use of human iPSC lines was approved by Institutional Biosafety Committee of Florida Atlantic University (Approval number B20-21). All iPSCs utilized in this study were used within 10 passages from cryopreserved stocks previously determined to be karyotypically normal.

After neuronal stem cells were derived from iPSCs with the rosette selection method, we utilized the method from N. Zhang et al., 2010 to differentiate neuronal stem cells into striatal medium spiny neurons. Briefly, striatal differentiation of neuronal stem cells was induced by changing neural proliferation medium to DMEM complete medium supplemented with 250 ng/ml SHH (R&D Systems), 100 ng/ml DKK1 (R&D Systems), 20 ng/ml BDNF (Peprotech) and 10 μ M Y27632 (Calbiochem). This condition referred to as Stage 1 was maintained for 8-10 days. For Stage 2, cells were exposed to 0.5 mM

dibutryl-cyclic AMP (Sigma), 0.5 μ M valpromide (Alfa Aesar), 20 ng/ml BDNF and 10 μ M Y27632 for 1-3 days or for the length of the culture. The scheme overview of the MSN differentiation process was shown in Figure 2-1.

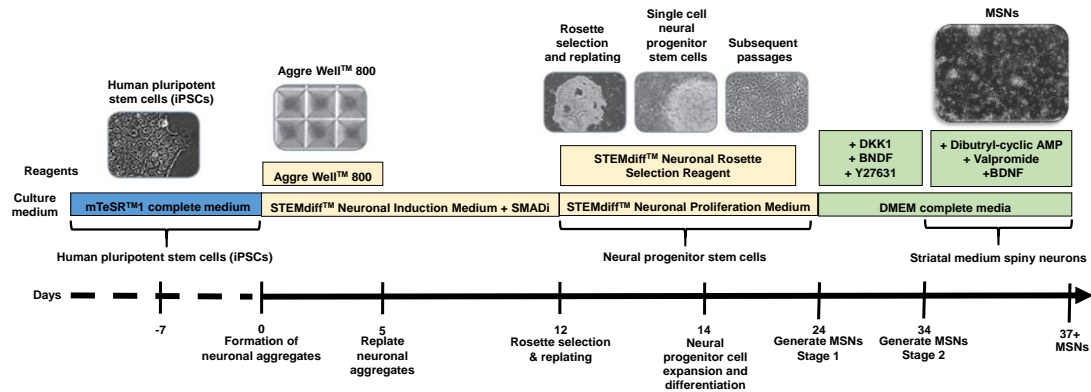


Figure 2-1 Schematic time frame of the differentiation protocol of iPSCs to MSNs.

2.2.2 MEA recording, parameters, and data analysis

MEA recording: To record neuron activity, a Multiwell MEA system (multichannel Systems, MCS GmbH, Reutlingen, Germany) with the 24-well plate was used. Each well consisted of 12 embedded electrodes with a diameter of 30 μ m, 300 μ m apart (Figure 2-2). The neuronal activity was recorded for 5-20 minutes as specified for the primary cortical neurons and 10 minutes for the MSNs after a 20 minute acclimatization period. The recording chamber was maintained at 37°C. The raw signal was sampled at 25 kHz for developmental protocols or 20 kHz for stimulation protocols.

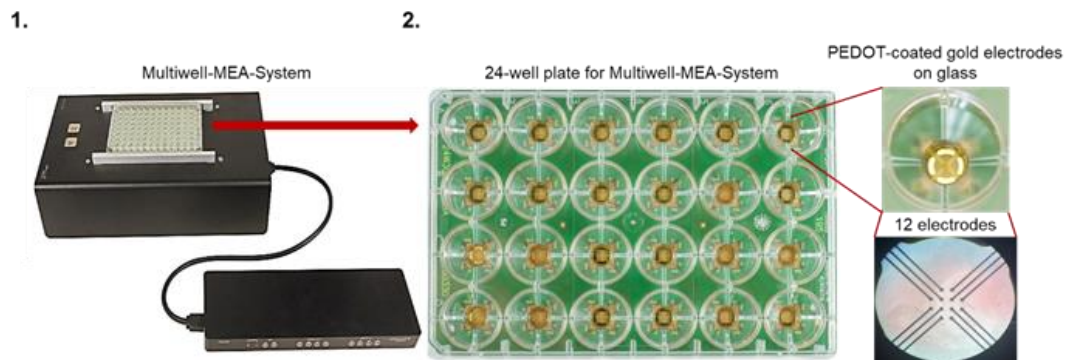


Figure 2-2 Multiwell MEA system (1) and 24-well plate (2) with poly(3,4-ethylenedioxythiophene) (PEDOT) coated gold electrodes. Each well contained 12 electrodes that were 30 μm in diameter and 300 μm apart.

Offline analysis: Offline data analysis was performed using Multiwell-Analyzer software (Multichannel Systems) (Figure 2-3). This permitted the extraction of parameters regarding to spiking activity, neuron excitability, and networks connectivity of individual microelectrodes to be collected in excel files. During analysis, the raw data was filtered with a Butterworth high passed filtered at 1 Hz, order of 2, and a low passed filtered at 3500 Hz, order of 4 which were optimized for the neuronal activity information analyzed for this study. A minimum amplitude of 10 μV was used for the detection of spiking activity. 50 segments were used to estimate the thresholds which was computed as the minimum standard deviation over all segments multiplied by either the “Rising Edge” or “Falling Edge” factor. This reduced the risk that standard deviation was strongly influenced by spike activity. The noise threshold of individual spike detection with set at ± 5.0 standard

deviation. Any microelectrodes with an excessive amount of noise that could not be filtered out were excluded from the data.

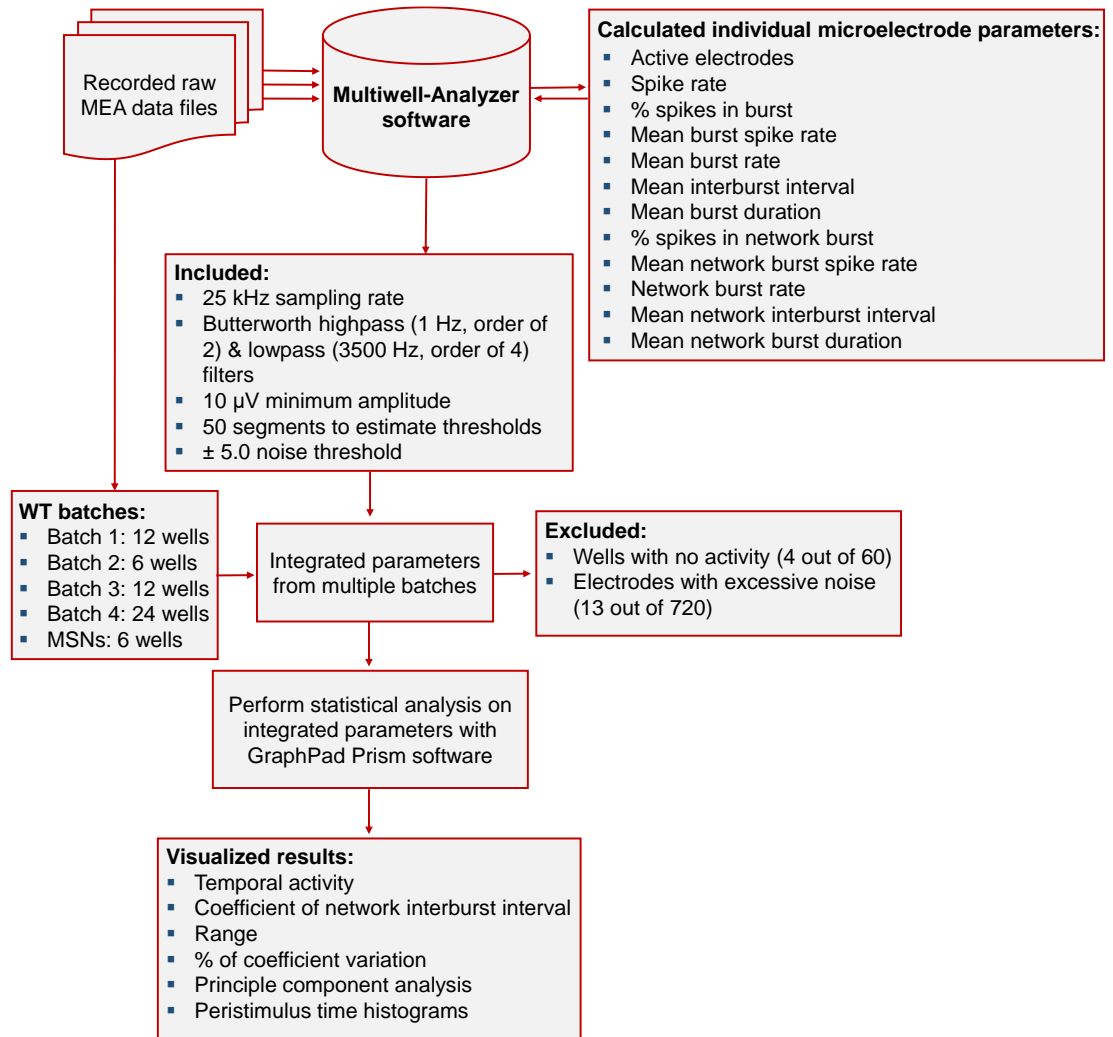


Figure 2-3 MEA analysis flow chart with inclusion and exclusion criteria.

The calculated individual active microelectrode parameters were averaged for a single well and used for spontaneous, temporal analysis of the primary dissociated cortical neurons and MSNs. Additionally, these parameters were used to define a stable dissociated

cortical cell phenotype on the MEA. These neuronal activity parameters used in this study were defined in Table 2-2 according to Cotterill et al., 2016.

Table 2-2 Definitions of parameters used to measure neuronal activity.

| Implication | Parameters | Explanation |
|------------------------------|--|---|
| <i>Spiking activity</i> | Active electrodes | Number of electrodes (n=12) per well detecting extracellular neuron activity. |
| | Spike rate (Hz) | Number of all spikes divided by the recording time per electrode. |
| <i>Neuronal excitability</i> | Percent spikes in burst | The number of spikes in burst divided by the total number of spikes. |
| | Mean burst spike rate (Hz) | The number of spikes in a burst divided by the burst duration in a well. |
| | Mean burst rate (burst/s) | The number of burst divided by the recording time per electrode per well. |
| | Interburst interval (ms) | The average interval between two consecutive burst per well. |
| | Mean burst duration | Averaged duration of burst per electrode per well. |
| <i>Neuronal connectivity</i> | Percent spikes in network burst | The number of spikes in network burst (minimum of 3 electrodes) divided by the total number of spikes. |
| | Network burst spike rate (Hz) | The number of spikes in a network burst (minimum of 3 electrodes) divided by the burst duration in a well. |
| | Network burst rate (burst/s) | The number of network burst (minimum of 3 electrodes) divided by the recording time per electrode per well. |
| | Network interburst interval (ms) | The average interval between two consecutive network burst per well. |
| | Network burst duration (ms) | The duration of a network bursts per electrode averaged per well. |
| | Coefficient of network interburst interval | Calculated by dividing the standard deviation of all the network interburst intervals to the mean. Values ranging zero and below mean very regular network burst while values ranging one and above mean very irregular network burst. |

The schematic of the parameters measured from the analyzed data was shown in Figure 2-4. This schematic explains the extraction of each parameter from the raw recordings as single channel activity and network burst activity from our MEAs raster plots.

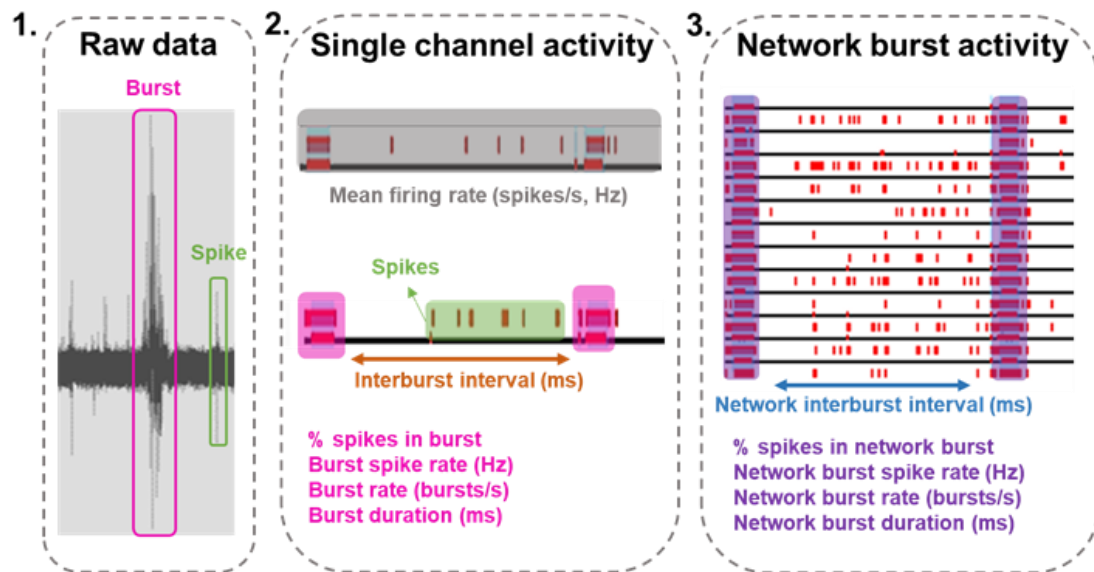


Figure 2-4 Schematic of parameters measured from the analyzed MEA data.

A set of guidelines were provided to prevent variability in experimental design, culturing methods and MEA analysis across all batches of cells (Table 2-3). To guarantee sufficient experimental replicates, a minimum of 6 wells per cell type was measured for temporal analysis or electrical stimulation analysis.

Table 2-3 List of guidelines. Guidelines were provided concerning the experimental design, cell culturing conditions, and MEA data analysis for this study.

| | |
|----------------------------|--|
| Experimental design | 6-24 wells per condition divided over 4 MEA batches |
| Cell culturing | Homogenous distribution of cells |
| | Optimal cells density for confluency and neuron-electrode coupling ($\approx 7,800$ cells/mm ²) |
| | Analyzed 12 MEA parameters |
| Data analysis | Pooling of data to analyze network development |
| | Analysis on all 12 electrodes |
| | Variability analysis for pooled batches |

Data and statistical analysis: To look at the developmental profile using temporal analysis, each well was counted as a single data point that represented the average of a measured parameter from the 12 microelectrodes within that well. To determine the stable time window of each parameter, the data were subjected to one-way ANOVA followed by multiple comparisons test using the GraphPad Prism software statistical package 9.0 (GraphPad Software). All experimental data was expressed as means \pm the standard error of mean (SEM) for the coefficient of network interburst interval or the standard deviation (SD) for the range and coefficient of variation as indicated. The criterion for significance was set at $p \leq 0.05$. To check the variability amongst the three batches for each parameter, the coefficient of variation on each parameter was calculated independently for all batches.

Principle component analysis: For principle component analysis (PCA), the data was analyzed the GraphPad Prism software statistical package 9.0 using the principle

component analysis. A PCA plot converts the correlation or lack of correlation among all the variables. For example, given that we had 11 variables for the pooled 4 batches, we could expect 11 PC eigenvalues that could result in 11 dimensions. With the 11 MEA parameters used for the PCA, a calculated 55 correlations ($(p(p-1)/2)$) could be made from one graph. Thus, parameters that cluster together are highly correlated and vice versa. Differences along the first principle component axis (PC1) are more important than differences along the second principle component axis (PC2). All 11 parameter (excluding active electrodes) from Table 2-2 were continuous variables included when calculating the principle component while the batch (batch 1, batch 2, batch 3 or batch 4) was the categorical variable. The method used for these criteria was standardized which means the data were to have a mean of zero and a standard deviation of one. This is similar to a correlation matrix. The method for selecting the principle components (PCs) was based on the eigenvalues which mean the PCs would have eigenvalues greater than one (Kaiser rule). The eigenvalues determine how much variance there is in the data depending on the principle component of 1 and 2. Principle component 1 was shown since it represents the maximum variance direction of the pooled, 11 parameters. Principle component 2 was also shown in the PCA plot since it represented the second largest variance across the pooled data of the 11 parameters. Principle components 3-11 of the pooled data represented values of 10.55% (PC3) down to 0.65% (PC11). Thus, our PC plots showed the projected direction of variance for each parameter within the PC1 (e.g. 36.38%) and PC2 (e.g. 24.64%) to

explain the largest variance and second largest variance seen in the pooled data, respectively.

Pulse width and voltage stimulation protocols with MEA: To see the effects of biphasic pulse widths and associated voltages on direct and synaptic responses, we utilized a positive-negative biphasic waveform (Figure 2-5 (a)). The interpulse interval (IPI) was set to 10 ms. The interburst interval (IBI) was set to 10,000 ms with a single burst consisting of 5 bursts (Figure 2-5 (b)). The stimulation cut-off time was 100 ms. Thus, only the effects of a single burst consisting of 5 pulses was recorded for each stimulation protocol.

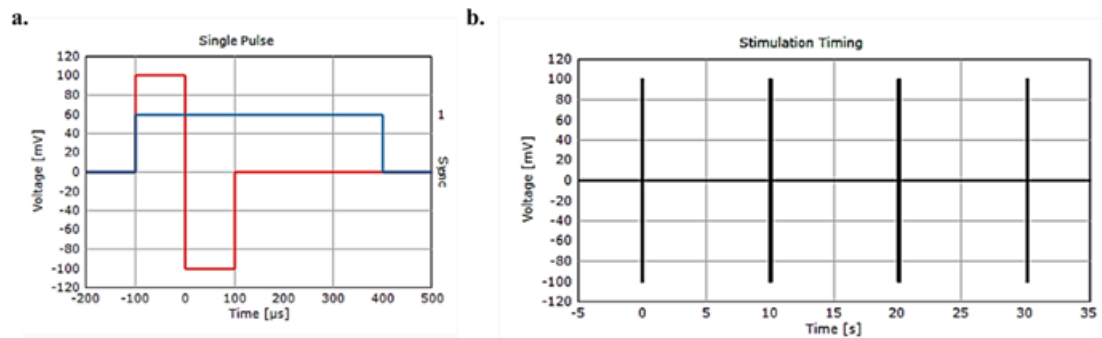


Figure 2-5 Biphasic stimulation pulse and stimulation timing scheme. (a) Characteristic, biphasic pulse showing a pulse width of 100 μ s for the positive and negative peaks. (b) Stimulation timing showed an interburst interval of 10,000 ms with a burst consisting of 5 spikes. The IPI of those 5 spikes was 10 ms. Stimulation was stopped by 100 ms.

15 stimulation protocols shown in Table 2-4 were utilized to stimulate a single batch consisting of 24-wells cultured with dissociated cortical neurons.

Table 2-4 Stimulation parameters applied to cortical neurons DIV12.

| Stimulation protocol | Biphasic pulse interval | Applied voltage |
|----------------------|-------------------------|-----------------|
| 1) | 100 μ s | 100 mV |
| 2) | | 300 mV |
| 3) | | 500 mV |
| 4) | | 700 mV |
| 5) | | 900 mV |
| 6) | 250 μ s | 100 mV |
| 7) | | 300 mV |
| 8) | | 500 mV |
| 9) | | 700 mV |
| 10) | | 900 mV |
| 11) | 500 μ s | 100 mV |
| 12) | | 300 mV |
| 13) | | 500 mV |
| 14) | | 700 mV |
| 15) | | 900 mV |

We utilized peristimulus time histograms (PSTH) to visualize the rate and timing of neuronal spike discharges, specifically direct and synaptic responses to the stimulation. These graphs were generated after analysis with the Multiwell-Analyzer software and values with units as spikes/s were extracted for each recording electrode of each well. To make a PSTH, a spike train (spikes/s) are recorded from the cells of the recording electrode(s). This spike train is aligned with the onset of an identical stimulus that can be single or repeated. The aligned spike trains are then superimposed in time to create the histogram [109]. The bin size used for the PSTH was 10 ms and 600 ms of neuron activity was shown after the stimulus. The first 0-60 ms bins were excluded from the PSTH graphs since this time frame contained artifacts of the 5 pulses.

Pharmacology: For increasing excitation, we removed 100 μ l of media from each chosen well and added a final concentration of 10 μ M of Picrotoxin (PTX) (Sigma A-169), action of mechanism shown in Figure 2-6 (b)) from a 10 mM stock to antagonize the inhibitory GABA_A receptor. For blocking NMDA receptor and AMPA receptor-mediated activity, we used a medium pre-mixed with CNQX (Sigma C-239), an AMPA/kainate antagonist, and MK801 (Sigma M-107), a NMDA antagonist, at 10 μ M and 20 μ M concentrations respectively (action of mechanism shown in Figure 2-6 (a)). Prior to the addition of either excitatory or inhibitory drugs into the wells, we recorded a baseline of 10 minutes after allowing the culture to equilibrate for 30 minutes. After the addition of the excitatory or inhibitory drugs to the wells and allowing the drugs to mix into the remaining culture media, we recorded the activity for another 10 minutes. Afterwards, we recorded a 1 minute baseline before the stimulus, then the 500 μ s at 500 mV stimulus, and finally, a 1 minute recording after the stimulus.

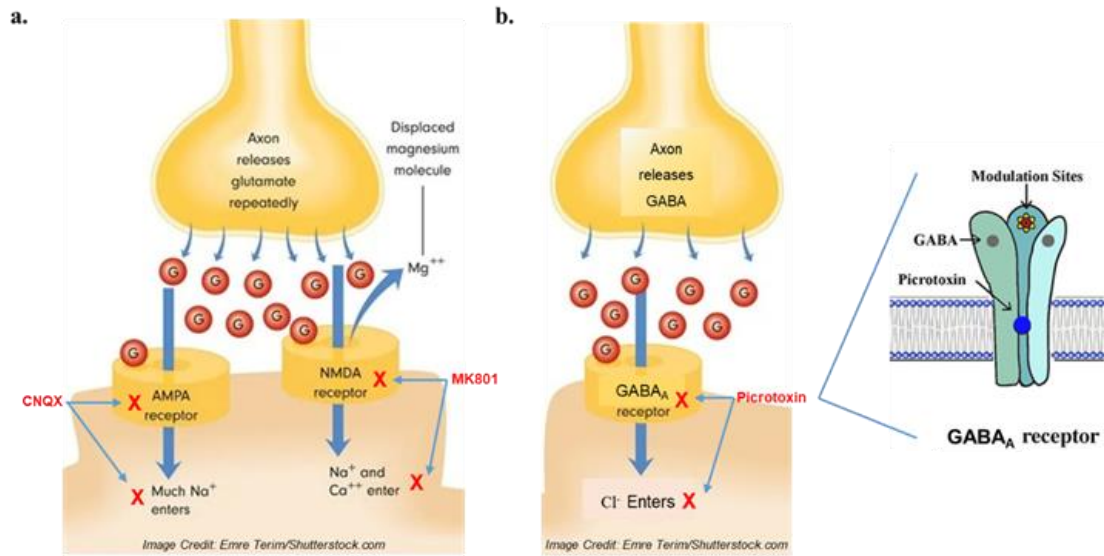


Figure 2-6 Inhibitory and excitatory drug effects on post-synaptic terminals. (a) CNQX is an antagonist of AMPA receptors and block the ion flow of sodium intracellularly which leads to depolarization of the post-synaptic side. MK801 is an antagonist of NMDA receptors and blocks the ion flow of sodium and calcium intracellularly which leads to depolarization on the post-synaptic side. (b) Axons that release GABA on the pre-synaptic side will bind to GABAA modulation sites of the receptor on the post-synaptic side. Activation of GABAA allows for the influx of chloride intracellularly which leads to hyperpolarization of the membrane potential on the post-synaptic side. Picrotoxin blocks the GABAA receptor.

2.3 Results

2.3.1 Temporal analysis of neuronal activity in dissociated, primary cortical neurons

To temporally examine the spontaneous neuronal activity of primary cortical neurons, we performed daily recordings of their spontaneous activity for 10 minutes starting from DIV7. A representative image of primary neurons cultured on the electrodes in a single well is shown in Figure 2-7 (a). Neuronal activities were analyzed at three different levels: spiking, burst and network activities. A representative raster plot from DIV13 is shown to indicate synchronized bursts (red clustered lines) and network activities (blue bar across all electrodes). (Figure 2-7 (b)).

Spontaneous spiking: In general, the spiking activity increased over the developmental time and was stable across the 12 electrodes from DIV13-DIV18 (Figure 2-7 (c)). The occurrence of spiking activity in the burst was stable by DIV13 (Figure 2-7 (e and f)). The spiking activity within the network burst also stabilized between DIV13-DIV18 (Figure 2-7 (j-k)).

Bursting activity: General bursting activity was relatively stable between DIV10-DIV11 (Figure 2-7 (e-h)) with exception of the mean burst duration (Figure 2-7 (i)) which stabilized by DIV14. The mean interburst interval decreased from DIV7-DIV10 and then stabilized DIV11-DIV18 indicating a regularity in the interval between each burst (Figure 2-7 (h)).

Neuronal network connectivity: In general, stable network connectivity gave mixed results. The % spikes in the network burst (Figure 2-7 (j)) monotonically increased DIV7-DIV12 before plateauing DIV11-DIV18 at around 78% which was similar to the % spikes in the burst parameter (Figure 2-7 (e)). Like the burst spike rate parameter (Figure 2-7 (f)) the mean network burst spike rate (Figure 2-7 (k)) plateaued DIV13-18 indicating a correlation in these two parameters as the network matured. Maturation of network bursts (Figure 2-7 (j, l, and n)) also seem to be correlated given their stabilization by DIV10-DIV12. However, the interval between this network bursts (Figure 2-7 (m)) was stable by DIV10 indicating spiking organization occurring within the network burst and not in the random spiking.

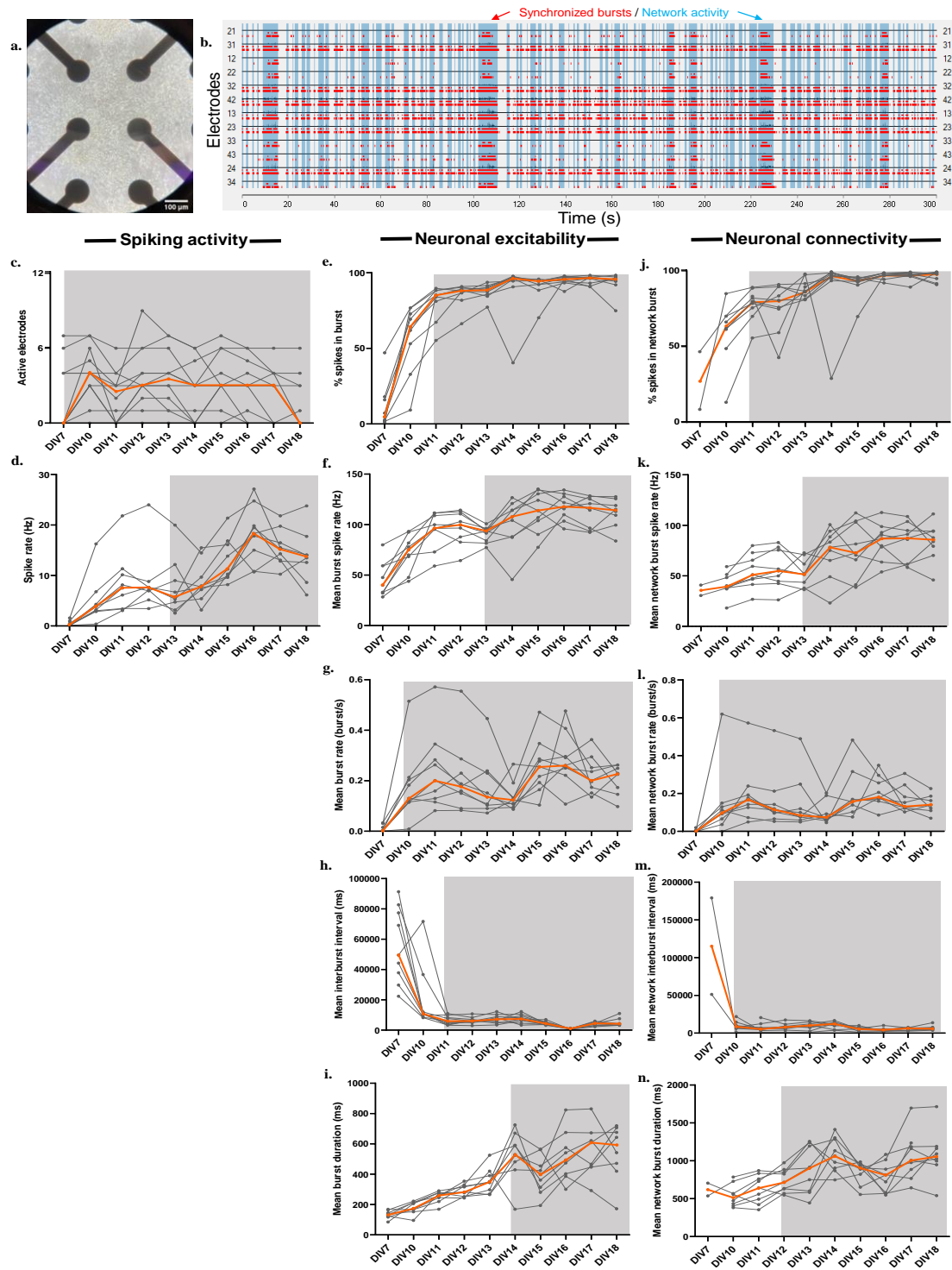


Figure 2-7 Developmental profile of spontaneous activity for dissociated, primary neurons.

(a) Representative brightfield image of well with neurons in contact with the electrodes and showing even distribution. (b) Representative raster plot of network activity across

twelve electrodes during stable time window of DIV13. Red lines indicate spiking activity. Red boxes indicated bursting activity. Network activity highlighted in light blue. (c-m) Temporal analysis showing stable neuronal activity indicated with gray boxes for each parameter was determined with one-way ANOVA followed by multiple comparisons test. Orange line represented the median for each parameter from a total of 12 wells. Each gray line represents the calculated average of 12 electrodes per well for each parameter over the duration of the temporal analysis.

Given that electrophysiological parameters stabilized within a temporal time frame of DIV10-DIV18 in this pilot study, we further explored the variability of all the parameters across four independent MEA batches and pooled their information within a DIV10-DIV18 time frame. Information regarding the batches of dissociated, primary neurons used for this study was shown in Table 2-5. The DIV represented the days *in vitro* MEA neuronal activity was recorded for each batch.

Table 2-5 Information regarding the three independent batches of mouse primary neuronal cultures used for this study.

| Name | # of wells | DIVs |
|----------------|-------------------|---------------------------------------|
| <i>Batch 1</i> | 12 | 7, 10, 11, 12, 13, 14, 15, 16, 17, 18 |
| <i>Batch 2</i> | 6 | 10, 12, 14 |
| <i>Batch 3</i> | 12 | 13, 14, 15 |
| <i>Batch 4</i> | 23 | 11, 19 |

Coefficient of network interburst interval: The coefficient of network interburst interval differentiated a regular network burst with a value of zero and below from an irregular network with a value of one and above. We showed that the four individual dissociated cortical batches had a mostly regular network burst during the DIV10-DIV19 time window (Figure 2-8 (a)). When pooled (orange values), we confirmed that with more batches, the standard error of mean (SEM) decreased compared to batches 1 and 4 indicating how far the mean of the data was from the true population mean.

Specific range: To visualize the variability of each parameter across four batches, the range was calculated, averaged for each parameter of each batch, and then averaged across the four batches with standard deviation to see the dispersion in each batches' average for that parameter ($n_{\text{well}}=53$), (Figure 2-8 (b)). Neural networks showed a general level of activity of 17.3 for spike rate (Hz), 0.5 mean burst rate (bursts/s), and 0.5 mean network burst rate (bursts/s) with mean network burst duration (s) of 1.2.

Coefficient of variation: Next, we further investigated the variability in the MEA parameters within the four batches to identify the most robust parameters (i.e., coefficient of variation lower than 50% as cutoffs) (Figure 2-8 (c)). Certain parameters were more stable including % spikes in the network burst, mean burst spike rate, % spikes in burst, mean network burst duration, mean network burst spike rate, and the mean burst duration. The more variable parameters (parameters that were not lower than the 50% cutoff) were mean network interburst interval, spike rate, mean interburst interval, mean burst rate, and mean network burst rate.

Principle component analysis: A PCA was carried out to visualize the differences of the 11 parameters (Figure 2-8 (d)) across the four batches as a loadings graphs and to visualize the level of differences among the four batches according to all their parameters as a PC score graph (Figure 2-8 (e)). The PC1 accounts for the largest possible variance explained at 36.38% while the PC2 accounts for the second largest variance explained at 24.64% (Figure 2-8 (d and e)). First thing noted was the high level of correlation between certain parameters due to the length and direction of the arrows in the loadings graph (Figure 2-8 (d)). For example, the mean interburst interval and mean network interburst interval were positively correlated (lower two arrows). Mean burst rate and mean network burst rate were positively correlated (upper two arrows). Spike rate showed positive correlation to the mean burst rate and mean network burst rate. Mean network burst spike rate, mean burst spike rate, mean burst duration, mean network burst duration, % spikes in burst, and % spikes in network burst were positively correlated by their similarity in arrow lengths and their close proximity by their arrow's direction (middle, right cluster). In comparison, mean burst rate and mean network burst rate were negatively correlated to the mean interburst interval and mean network interburst interval given the opposite directions of the arrows. Given the radial length of the arrows from the zero point, we know the MEA activity of these parameters was totally captured by this PCA and that close to 100% each of these parameters variances were explained due to the mostly equivalent length of the arrows and the proximity of the arrowheads. In terms of the PC score graph (Figure 2-8 (e)), all four batches showed overlap at the zero value of PC1 and PC2 and did not show

clear separate clusters for each batch. This result indicated similarity in the MEA activity phenotype of all four batches concerning the 11 parameters during the stable window of DIV10-DIV19

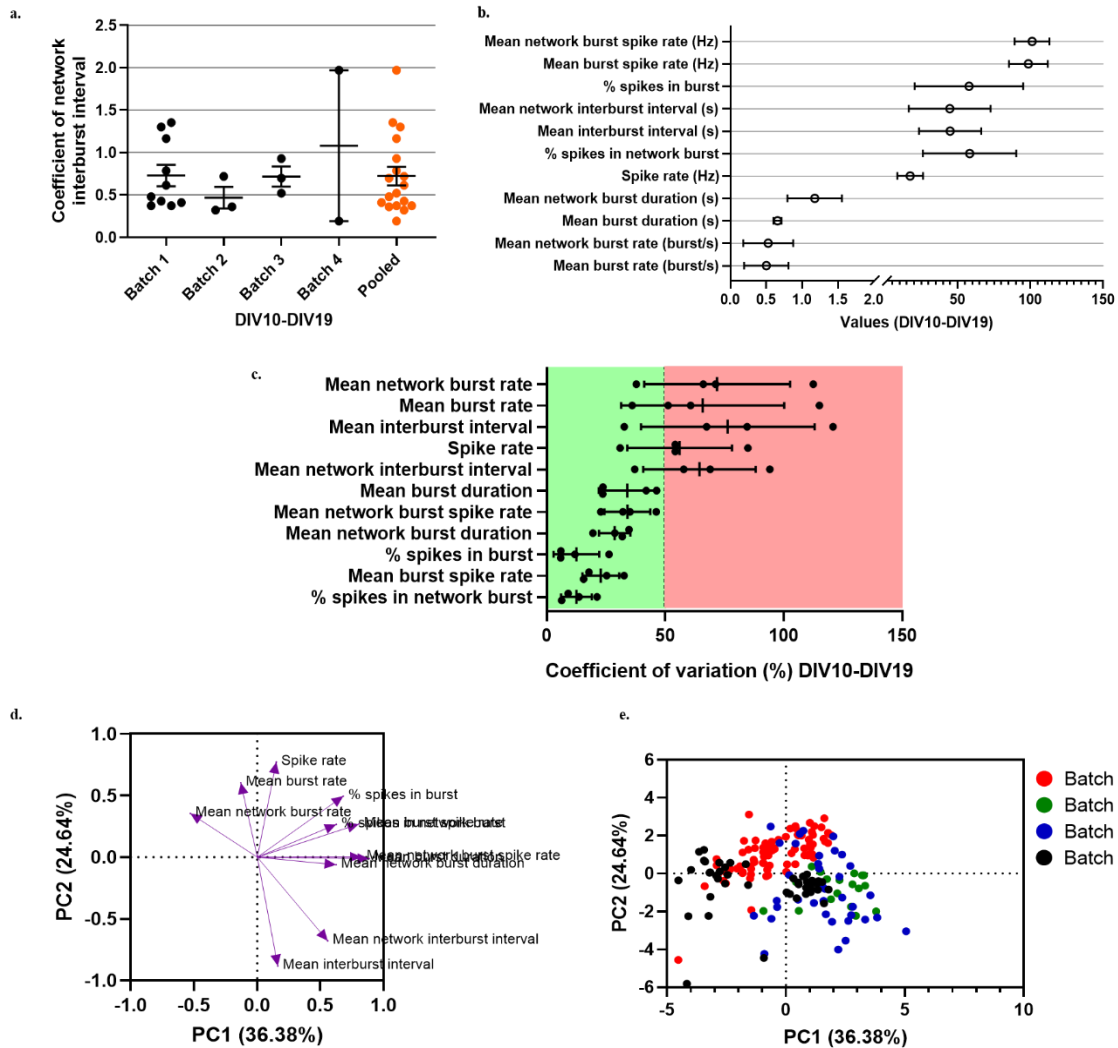


Figure 2-8 Neuronal networks showed a stable phenotype on MEA. (a) Coefficient of network interburst interval of all four batches of cortical cells separately and pooled together indicating regularity of network burst with a value below 1. Mean \pm SEM shown with black lines. (b) Graph showing the range in which the MEA parameters of all three

batches behaved from DIV10-DIV19. Values were averaged per batch and then averaged across all batches with SD. (c) Percent coefficient of variation of all 11 parameters across three batches DIV10-DIV18 to determine the most robust parameters with 50% as the cutoff points. Mean \pm SD shown with black lines. nwells=53. (d) PCA loading plot to showed 55 possible correlations of the 11 parameters DIV10-DIV19 from the three combined batches. PC score graph showed individual batch clustering DIV10-DIV19.

2.3.2 Electrical stimulation-evoked activity in primary mouse neuronal culture

Electrical stimulation through MEAs has been used to elicit spiking activity in dissociated cortical neurons [110], [111], [112]. When establishing stimulation protocols, choices need to be made on the robustness of the neuronal activity within the of the wells used for stimulation, which electrode to use as a stimulating electrode, the pulse width of the biphasic waveform used for stimulation, and the voltage level that can be used to evoke activity. Direct responses to electrical stimuli that do not depend on glutamatergic synapses are known as direct responses [113]. To explore stimulus evoked direct and synaptic responses in dissociated cortical neurons, we utilized a full 24-well plate of cells to first find the most robust wells for stimulation with whole well analysis. Second, PCA was done on to look at variations in the spiking, excitability, and network activity parameters of those robust wells to further narrow down well with similar network activity. Third, we implemented 15 different electrical stimulation protocols to compare the effects of biphasic pulse width and voltage on direct and synaptic responses. Last, we utilized picrotoxin

(PTX), an antagonist of GABA_A receptors, to observe if there was a spatial change in the spontaneous firing which would shed light on the effects that inhibitory populations within the neural network had on spontaneous firing.

Whole-well analysis of spike, burst, and network burst activity: A raster plot from the representative A4 well showed the distribution of spikes (thin black lines), bursts (red blocks), and network bursts (aligned red block highlighted in blue) across all 12 electrodes (Figure 2-9 (a)). To determine the best electrode for stimulating the neuronal network, each well was analyzed with the Multiwell-Analyzer software with all criteria utilized for in the developmental profile experiments adhered to including Butterworth filters, segments, and a minimum of three active electrodes to define network bursting activity. To choose a stimulating electrode per well that would be utilized for the electrical stimulation protocol, the criteria used was the following; the burst needed to be consistent across all highlighted network burst for the duration of the recording and the bursts needed to have the largest negative and positive microvoltage (Figure 2-9 (b)) which indicated that a depolarizing cell(s) was close to that electrode. In the case of the representative well A4, electrode 31 was chosen as the stimulating electrode (Figure 2-9 (b)). To utilize wells that had robust neuronal activity for electrical stimulation, we graphed the spike count, burst count, and network burst count (Figure 2-9 (b, c, and d)). Any wells with a spike count below 500, such as well A1, was automatically excluded from further experimentation and analysis (Figure 2-9 (c)). The burst count showed normal variation of between 50 and 100, excluding well A1 (Figure 2-9 (d)). The network burst count showed normal variation

between 40 and 80, excluding well A1 (Figure 2-9 (e)). Thus, no other wells were exclude other than A1 with the whole well analysis.

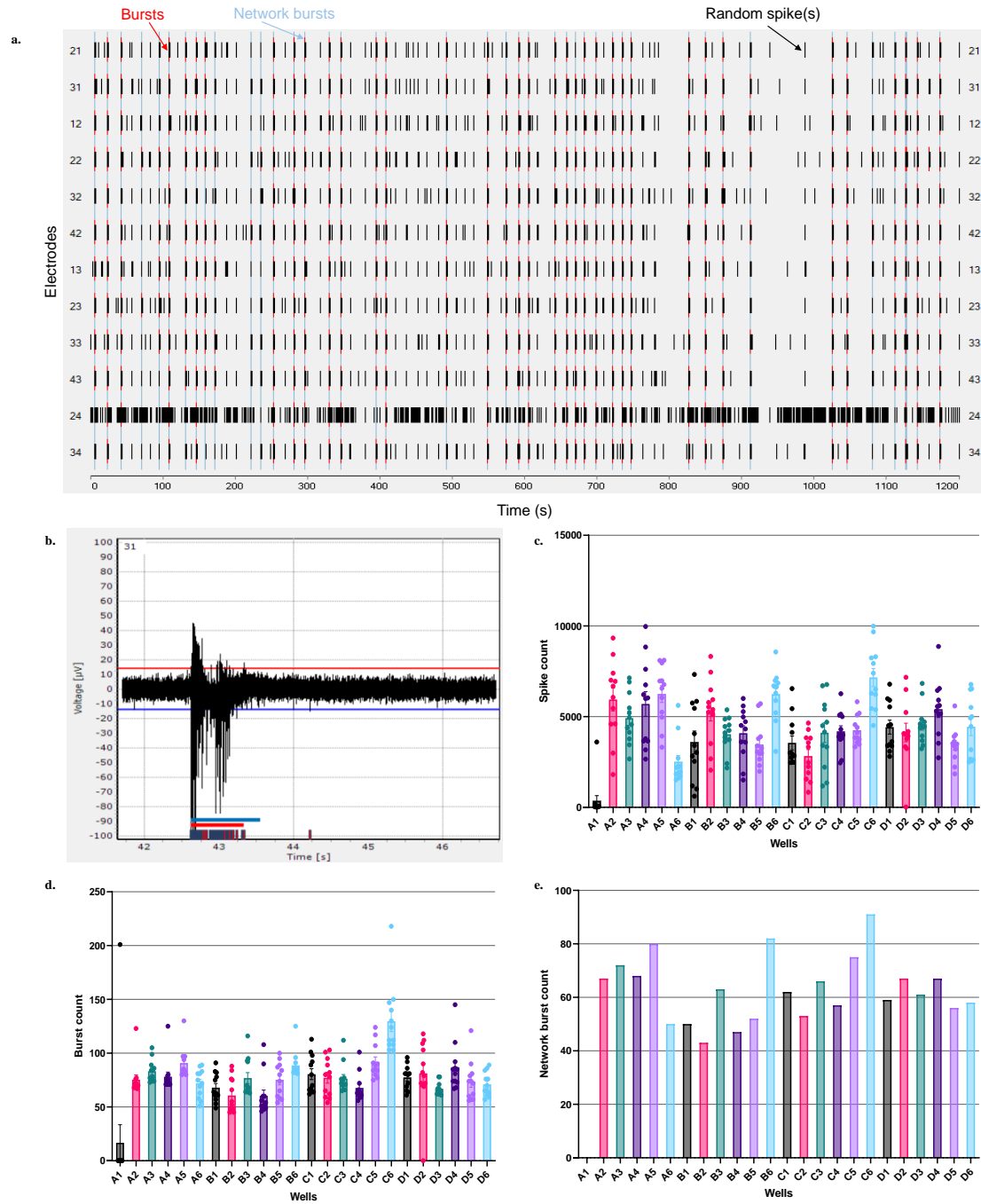


Figure 2-9 Well-wide analysis of batch 4. (a) Temporal raster plot from representative well A4 on DIV11 showing spikes (black lines) bursts (red blocks), and network bursts (highlighted in blue). (b) Example of criteria used to select one stimulating electrode per

well. (c) Extracted spike counts of each electrode from all 24 wells. (d) Extracted burst counts of each electrode from all 24 wells. (e) Extracted network burst counts of each electrode from all 24 wells. Data shown as mean with SEM.

Principle component analysis: A PCA was carried out to visualize the differences of the 11 parameters across the 23 wells as a loading graph (Figure 2-10 (a)) and to visualize the level of differences among the 23 wells according to all their parameters as a PC score graph (Figure 2-10 (b)). The PC1 accounts for the largest possible variance explained at 32.50% while the PC2 accounts for the second largest variance explained at 26.14%. Given the almost equal radial length of the arrows from the zero point, we know the MEA activity of all of the parameters except % spikes in the burst and % spikes in the network burst were totally captured by this PCA and that close to 100% each of these parameters variances were explained due to the mostly equivalent length of the arrows and the proximity of the arrowheads. The exceptions, % spikes in burst and % spikes in the network burst, had shortened arrows. Both of these results indicated that these parameters were not well explained within the PCA and that their correlation and variance interpretations were ambiguous. Mean network burst rate had negative correlation to mean network interburst interval. Also, the mean burst rate had negative correlation to the mean interburst interval. Spike rate and mean burst rate showed high positive correlation. With regards to PC1, mean network interburst interval, mean network burst duration, mean interburst interval, and mean burst duration showed positive correlation. Spike rate mean

burst spike rate, mean network burst spike rate, and mean network burst rate also showed positive correlation to each other with regards to PC1. In terms of the PC score graph (Figure 2-10 (b)), 23 wells could be graphed according to presences of data at the electrode for certain parameters and/or their presence within the PC1 and PC2 variances. The results of the PC score graph indicated similarity across 23 wells of a single batch concerning the 11 parameters.

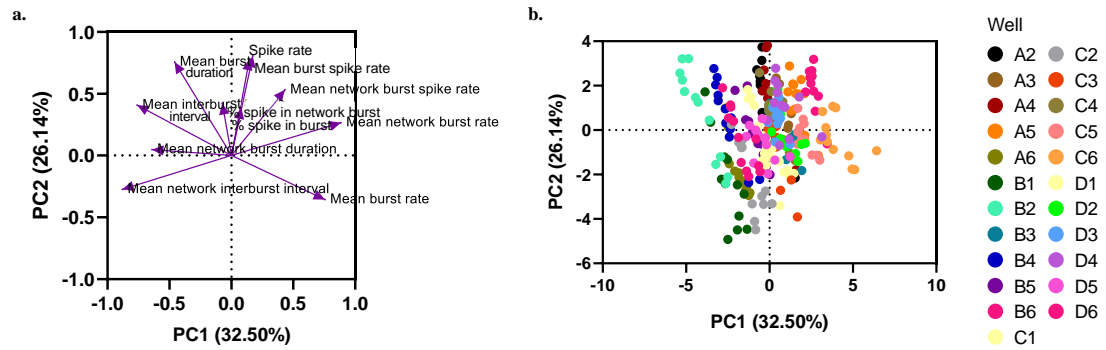


Figure 2-10 Variation of network activity accounted across 23 wells from batch 4. (a) PCA loading plot showed 55 possible correlations of the 11 parameters of 23 wells from a single batch of dissociated, cortical neurons on DIV11. PC score graph showed individual well clustering on DIV11.

Stimulation protocols: At this point, we had narrowed down the most robust wells with the least variation well-to-well and we had chosen a stimulating electrode per well that increased the chances of evoking network wide bursting activity. For the stimulation, we utilized 15 stimulation protocols that had a stimulation time period of 100 ms with a

total of 5 pulses. The interpulse interval (IPI) was set to 10 ms. A representative well and recording electrode, in this case well A4, electrode 12, was chosen to represent the responses seen with stimulation protocols since this electrode had consistent bursting and network activity across the recording time. A raster plot of the representative A4 well showed the temporal layout of burst (red boxes) network bursts (highlighted in blue), random spikes (black lines), stimuli (gold line) (Figure 2-11). The stimulating electrode was electrode 31 for this well. Direct and synaptic responses occurred within milliseconds of the stimulation (purple arrow). A recoding of one minute before and one minute after the stimulation was taken for a total time of 120 seconds. After the direct and synaptic responses occurred, spontaneous network activity resumed.

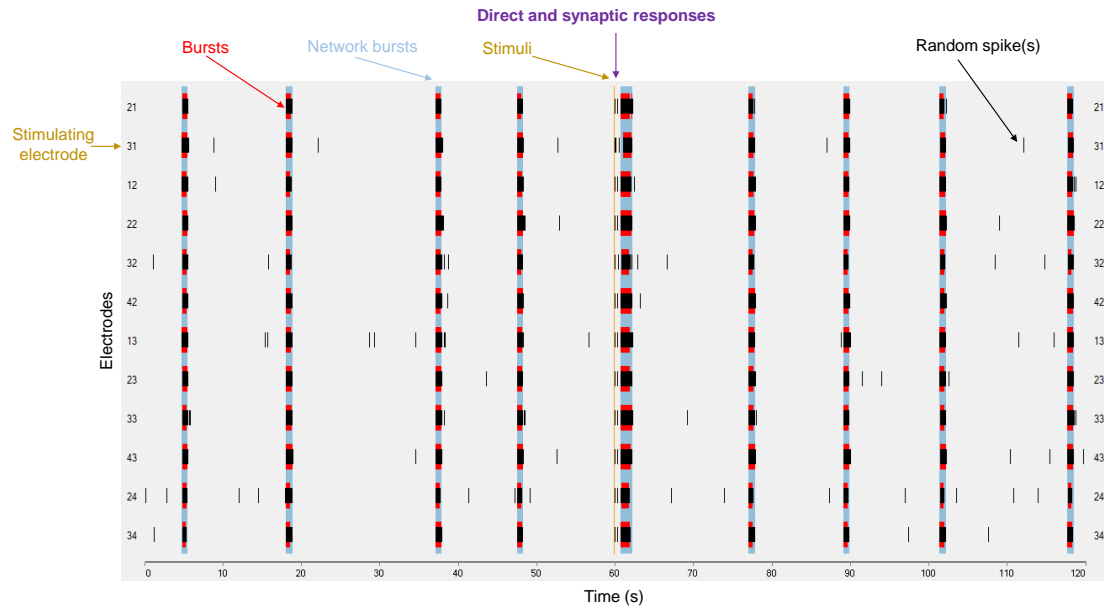


Figure 2-11 Raster plot of representative A4 well. The stimulating electrode was electrode 31. Detected burst highlighted in red, network burst highlighted in blue, electrical stimuli highlighted in gold, and random spikes shown as black lines across all 12 electrodes for a time period of 120 seconds. Direct and synaptic responses occurred within milliseconds after the stimuli before spontaneous activity resumes.

PSTH analysis of stimulation protocols: To see the temporal resolution at which responses occurred after the stimuli for each electrical stimulation protocol, the spikes/s was extracted from a single recording electrode from wells A2-A6. A PSTH bin size of 10 ms was used and 600 ms after the stimulation was utilized as the end point of the PSTH graphs. The stimulating electrode was excluded given that it had a 300 μ s delay time which would interfere with the temporal occurrence of the stimulated response and thus was

excluded. Given that we stimulated with a total of 5 bursts for a time period of 100 ms and the IPI was set to 10 ms, we excluded the 0-60 ms bins since the detected spikes/s showed to be artifacts of the 5 burst and not evoked spiking activity. Using the representative well A4, electrode 12, Figure 2-12 showed the effects of biphasic pulse width of 100 μ s (a) with increasing voltage, 250 μ s (b) with increasing voltage, and 500 μ s (c) with increasing voltage within a time frame of 600 ms. Overall, responses to the stimulation occurred approximately between 70-110 ms after the stimulation for all 15 stimulation protocols. There was also a second distinct response that occurred approximately between 340-440 ms for all the stimulation protocols. The “silent” periods between responses indicated the time needed for the action potential to travel down the axon to reach the pre-and post-synaptic clefts for the initiation of possible synaptic responses in the neuronal network. It was noted that that 250 μ s and 500 μ s pulse widths (Figure 2-12 (b and c)) with voltages of 300, 500, 700, and 900 mV appeared too consistently have a dampening effect on the response’s spiking activity. This indicated that the wider pulses resulted in fewer recorded responses since the early responses were obscured by stimulation artifacts earlier in the latency of the PSTH.

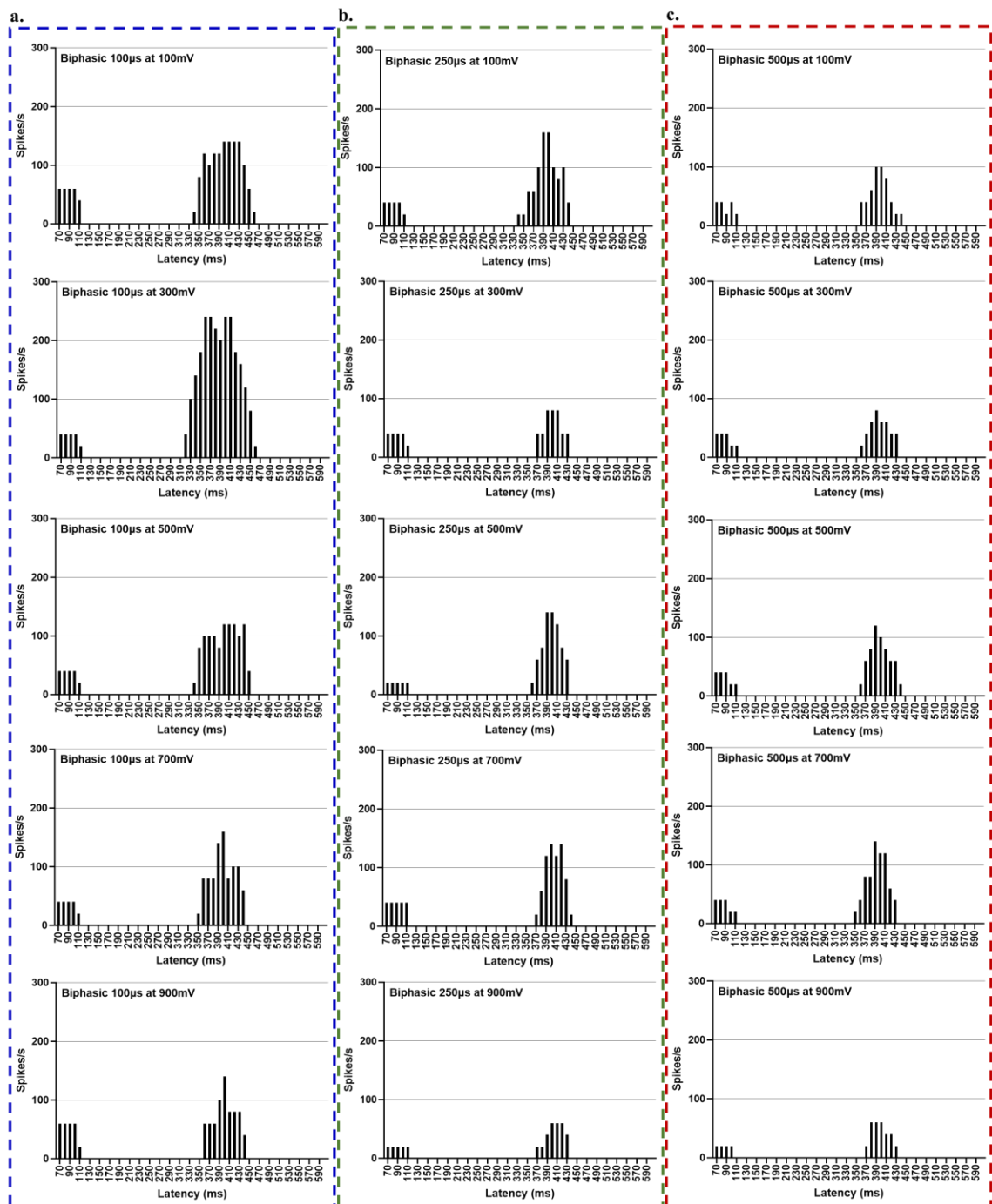


Figure 2-12 Firing activity of electrode 12 of well A4 for all 15 electrical stimulation protocols. (a) Applied biphasic 100 μ s pulse width with increasing voltage shown within blue box. (b) Applied biphasic 250 μ s pulse width with increasing voltage shown within

green box. (c) Applied biphasic 500 μ s pulse width with increasing voltage shown within red box.

To acquire a clearer, visual understanding of the differences between the effects of pulse width and/or voltage on direct and synaptic responses, the spiking activity across 600 ms (excluding the first 60 ms) were extracted from a single recording electrode of each of the 23 wells and pooled together (Figure 2-13 (b)). The recording electrode per well was chosen based on the reasons the representative A4, electrode 12 was chosen to represent responses to stimuli as indicated earlier. We also showed the single representative A1, electrode 12 to show that the statistical variance improved with more data points and the difference in the effects of the stimulation protocols was more enhanced with more data points (Figure 2-13 (a)). The results indicated the similarity in the spiking activity across all voltages with the 100 μ s pulse width (Figure 2-13 (b)) after one-way ANOVA analysis. A declining trend in the spiking activity was seen after 100 mV with both 250 μ s and 500 μ s pulse widths. One-way ANOVA analysis with multiple comparisons confirmed significance between the 100 μ s pulse width to the 250 μ s and 500 μ s pulse widths at the 300 mV, 500 mV, 700 mV and 900 mV voltages. These results indicated a combined, decreasing effect of wider pulse widths and higher voltages on spiking activity seen with evoked responses.

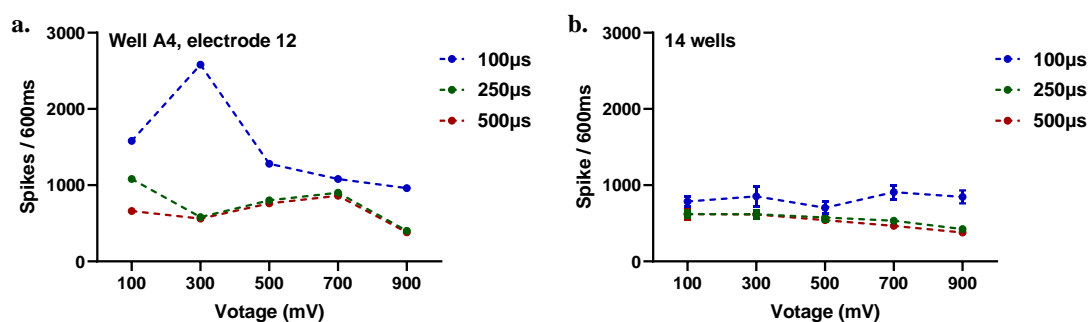


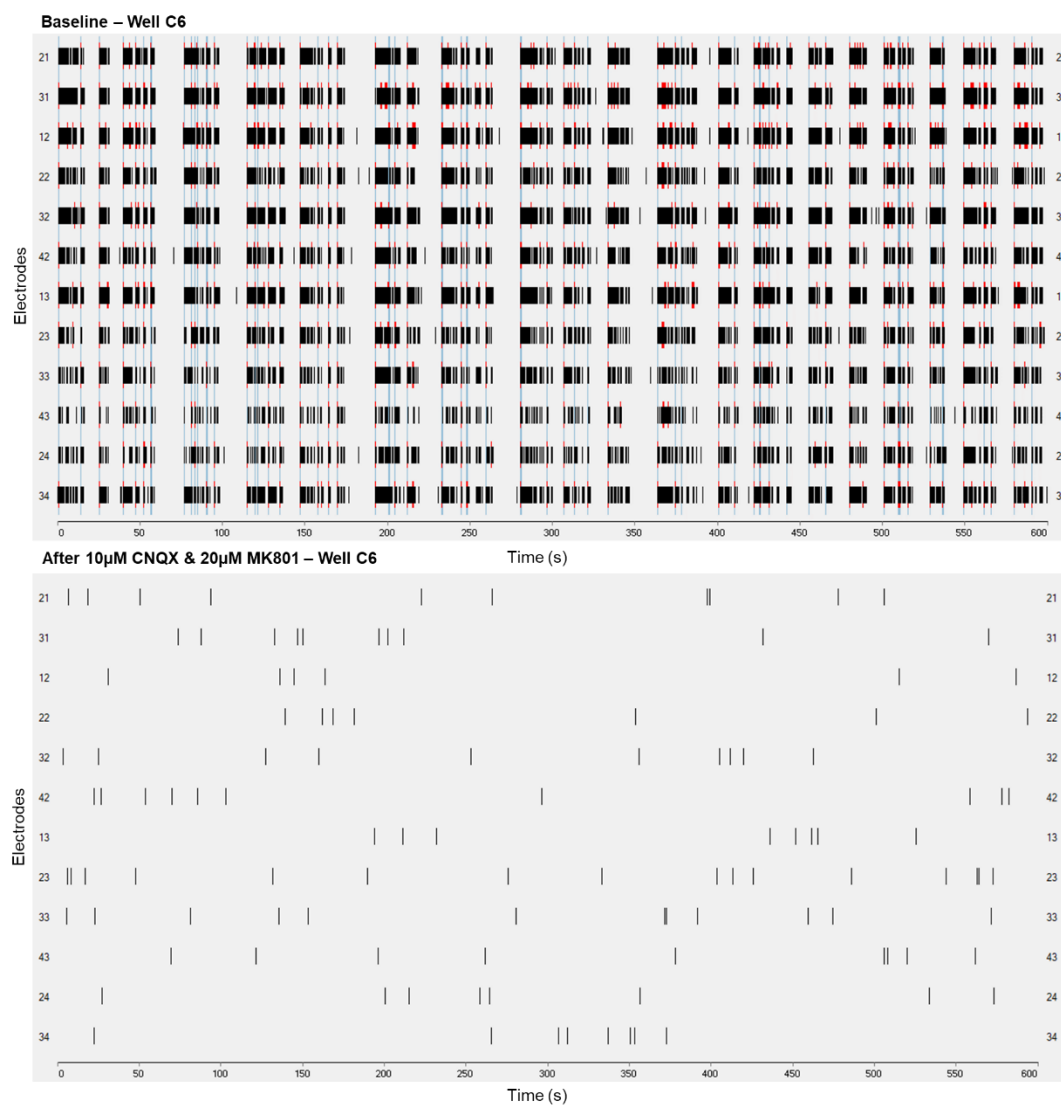
Figure 2-13 Spiking activity from direct and synaptic responses as a response to pulse width and voltage. (a) Spiking activity across 600 ms bins (excluding the first 50 ms bins) of the representative well A4, electrode 12 (b) Spiking activity of direct and synaptic responses to pulse width and voltage showed a downward trend with 250 μ s and 500 μ s pulse widths above 100 mV. Data shown as mean with SEM.

Effects of excitatory and inhibitory agonist on spontaneous and evoked activity:

Dissociated cortical neurons consist of a heterogeneous mixture of excitatory and inhibitory neurons. Given that we did see stimulus responses, inhibitory drugs to confirm or disprove the effects of our stimulation protocol. Using the same 24-well plate, we added 10 μ M and 20 μ M of CNQX and MK801, respectively, to both rows C and D which consisted of 12 wells. After the addition of CNQX and MK801, AMPA and NMDA agonist respectively, the raster plot showed almost no spiking activity across the 12 electrodes (Figure 2-14 (a)). Any spikes seen indicated spiking activity from non-glutamatergic neuronal population present in the culture. No measurable neuronal activity was seen

across all 11 parameters as confirmed by the lack of measurable activity from the spike rate, mean burst spike rate, and mean network burst spike rate parameters after the addition of CNQX and MK801 all electrodes of wells C1-D6 (Figure 2-14 (b-d)).

a.



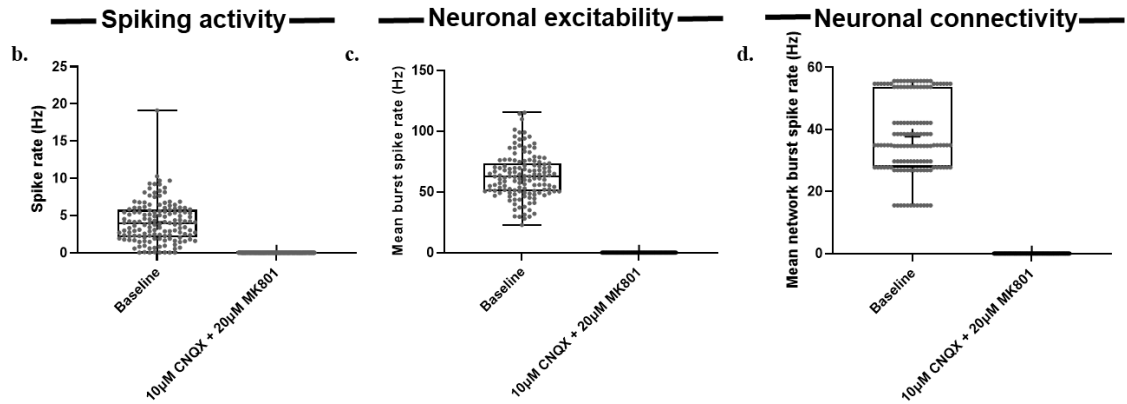


Figure 2-14 Effects of excitatory and inhibitory drugs neuronal activity parameters of dissociated cortical neurons. (a) Representative raster plots of cortical activity on DIV19 before and after the addition of both 10 μ M CNQX and 20 μ M MK801. (b-d) Three parameters measure showed no spiking activity after the addition of CNQX plus MK801 confirming it agonist effects on excitatory neurons.

Effects of stimulation on AMPA, and NMDA treated primary cortical cells: Given that the inhibitory drugs, CNQX + MK801, did inhibit neuronal activity, we then we then utilized the 500 μ s at 500 mV stimulation protocol to see the effects that AMPA + NMDA agonists had on evoked responses. The addition of CNQX and MK801 completely blocked all activity (Figure 2-15 (b)) in comparison to before the addition of CNQX and MK801 (Figure 2-15 (a)). This result indicated that that what we thought was direct activity as a result of stimulation was actually synaptic responses to the stimulation since CNQX and MK801 only blocks synaptic activity, not electrical activity. We additionally confirmed

that the responses seen to the stimulation were dependent on excitatory, glutamatergic neurons [113].

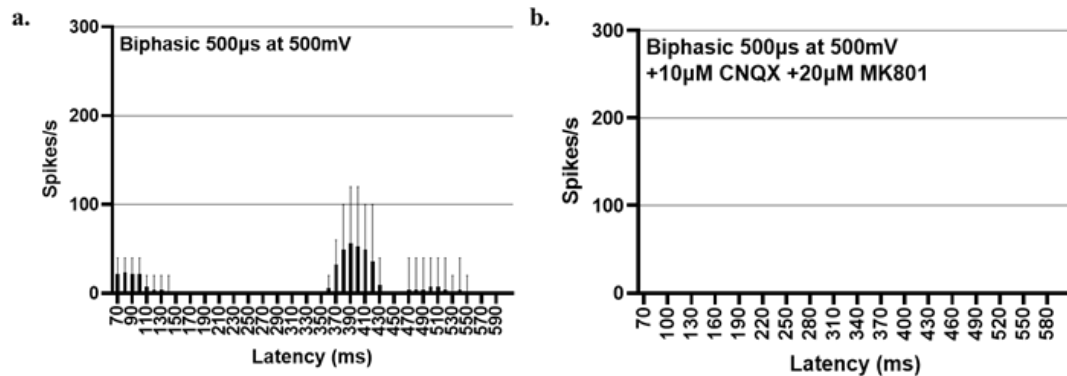


Figure 2-15 Effects of agonist on excitatory neurons after evoked activity. (a) A single electrode from each of the 12 wells pooled from row C-D were shown with stimulation after stimulation as the mean with the range. (b) The same 12 wells pooled from row C-D, where CNQX and MK801 were added, showed no spiking activity in response to stimulation.

2.3.3 Development profile of medium spiny neurons differentiated from iPSCs

To observe neural activity development in human neurons, we utilized one batch of human induced pluripotent stem cells that were differentiated into MSNs. The same 12 parameters describing the spiking activity, neuronal excitability, and neuronal connectivity were utilized to describe the MEA activity level of the entire well or individual electrodes which we aggregated in well-level values by taking the averages of the 12 electrodes (gray

lines) and the medium of those values (orange line) from 6 wells (Figure 2-16). Stable activity was determined with one-way ANOVA followed by multiple comparisons test. A raster plot from DIV14 represented stable network bursting activity across all twelve electrodes (Figure 2-16 (a)).

Spontaneous firing: MEA activity from the MSNs was measured from DIV1 of their complete differentiation from induced pluripotent stem cells to DIV30 for their developmental activity profile (Figure 2-16). The number of active electrodes increased and then stabilized by DIV12. In general, spiking activity increased over the developmental time before stabilizing DIV12 (Figure 2-16 (c)). Spiking activity in the burst was stable by DIV8 for both the non-network bursts (Figure 2-16 (d)) and the network bursts (Figure 2-17 (i)). The burst spike rate was stable DIV1 (Figure 2-16 (e)) while the network burst spike rate stabilized by DIV8 (Figure 2-16 (j)).

Bursting activity: Overall, bursting activity was stable from DIV4 (Figure 2-16 (f-g)) with the exceptions of the mean burst duration (Figure 2-16 (h)) which was plateaued DIV1-DIV24 and then did a rapid increase DIV26-DIV30. There was no statistical difference found in the values of the mean burst duration during DIV26-DIV30.

Neuronal network connectivity: In general, the formation of stable network connectivity emerged between DIV8-DIV12 (Figure 2-16 (i-l)). It was interesting to note that network activity was silent DIV1-DIV8, but once it emerged, it was immediately stable throughout DIV30. Like the mean burst duration (Figure 2-16 (h)), the mean network burst duration showed a high amount of variation DIV6 through DIV24 before suddenly

increasing DIV26-DIV30. There was no statistical difference found in the values of the mean network burst duration during DIV26-DIV30.

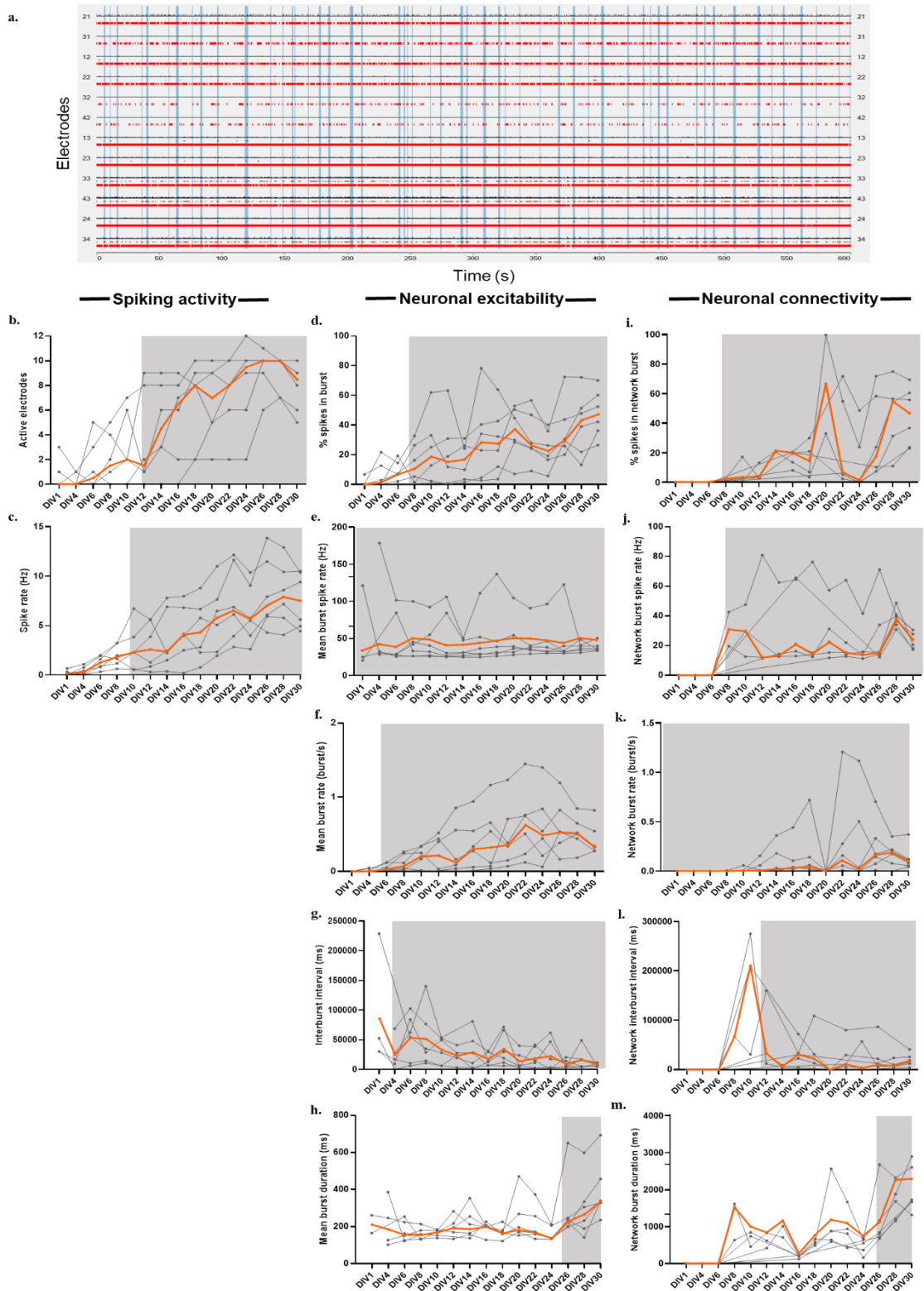


Figure 2-16 Developmental profile of spontaneous activity for MSNs. (a) Representative raster plot of a culture well on DIV14. Stable neuronal activity indicated with gray boxes

for each parameter (c-m). Orange line represented the medium for each parameter from a total of 6 wells (c-m). Each gray line represent the calculated average of 12 electrodes per well for each parameter over the duration of the temporal analysis (c-m).

Next, we calculated the ranges of each parameter according to the stable time window of DIV8-DIV30 indicated by the gray boxes in Figure 2-16. This was done to show the variability amongst the six wells of a single batch of MSNs. These ranges were shown in Table 2-6.

Table 2-6 Calculated ranges in which MEA parameters of one MSN batch of cells behave.

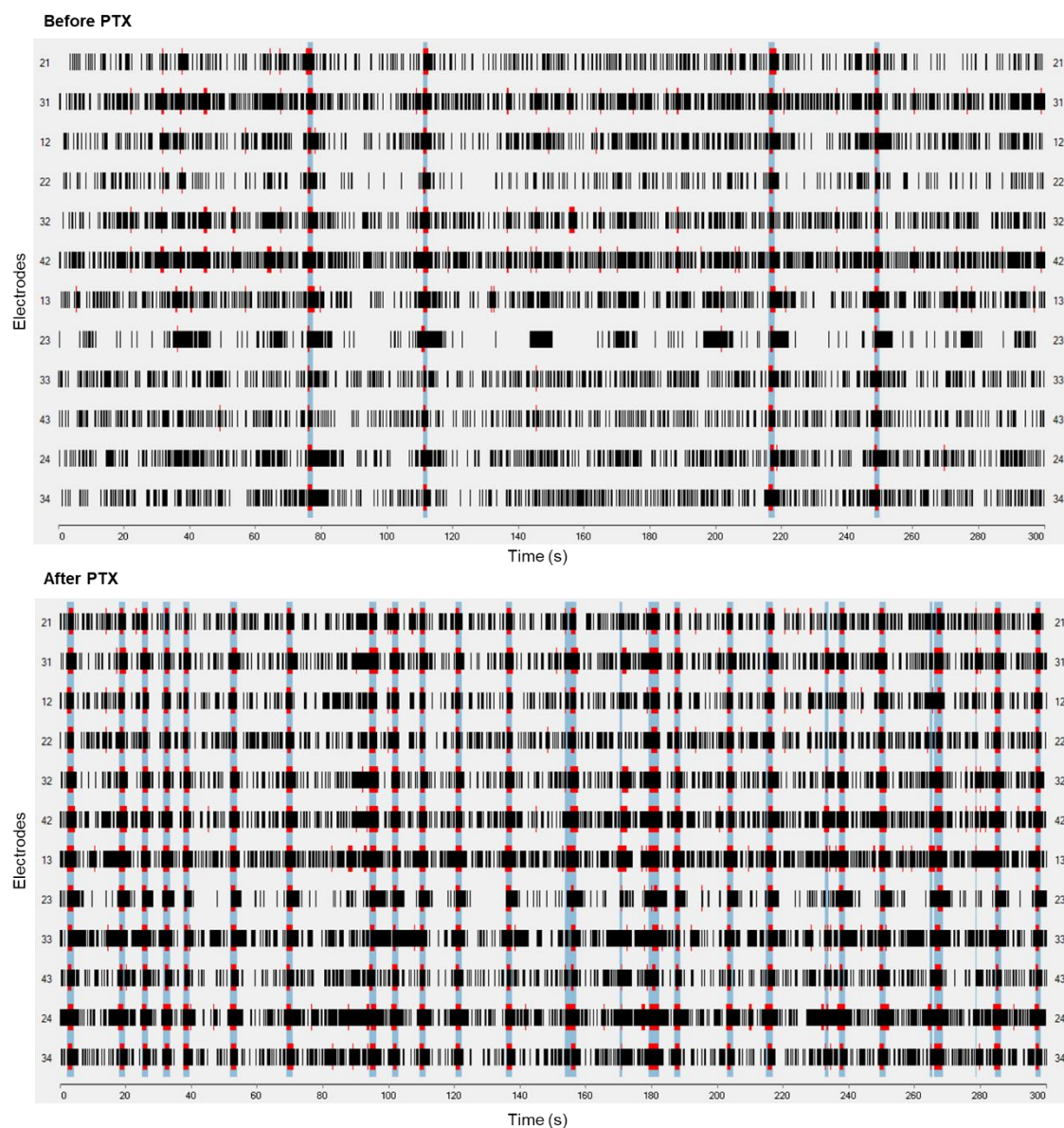
| Stable time window | Parameter | Range |
|---------------------------|---------------------------------------|------------------------|
| DIV10-30 | Spike rate (Hz) | 13.6 ± 3.5 |
| DIV8-30 | % spikes in burst | 78.2 ± 20.4 |
| DIV1-30 | Mean burst spike rate (Hz) | 103.8 ± 25.9 |
| DIV6-30 | Mean burst rate (burst/s) | 1.4 ± 0.4 |
| DIV4-30 | Mean interburst interval (ms) | $139,212 \pm 24,686.5$ |
| DIV26-30 | Mean burst duration (ms) | 570.8 ± 116 |
| DIV8-30 | % spikes in network burst | 99.8 ± 25.2 |
| DIV8-30 | Mean network burst spike rate (Hz) | 69.7 ± 19.5 |
| DIV12-30 | Network burst rate (burst/s) | 1.2 ± 0.2 |
| DIV8-30 | Mean network interburst interval (ms) | $275,166 \pm 56,019.9$ |
| DIV26-30 | Mean network burst duration (ms) | $2,780.5 \pm 707.6$ |

In vivo, medium spiny neurons typically receive cortical and thalamic glutamic synaptic inputs, leading to excitation of these normally inhibitory neurons [114]. To increase excitation, 1 μ M of picrotoxin from a 10 mM solution was added after a 10 minute

baseline recording on DIV34 as an antagonist of the GABA_A receptors (Figure 2-17 (a)).

It was noted that all 11 parameters (except for the active number the electrodes) had statistically significant changes indicating the effects of picrotoxin in our MSN's GABA_A receptors (Figure 2-17). The 10 minute post-PTX significantly increase MSN activity by significantly increasing the spike rate, % spikes in burst, mean burst spike rate, mean burst rate, mean burst duration, % spike in network burst, mean network burst rate, mean network burst rate, and mean network burst duration (Figure 17 (c, d, e, f, h, i, j, k, and m)). In contrast the mean interburst interval and mean network interburst interval parameters were significantly decrease with PTX which was consistent with the increases seen in the burst duration and network burst duration (Figure 17 (g and l)).

a.



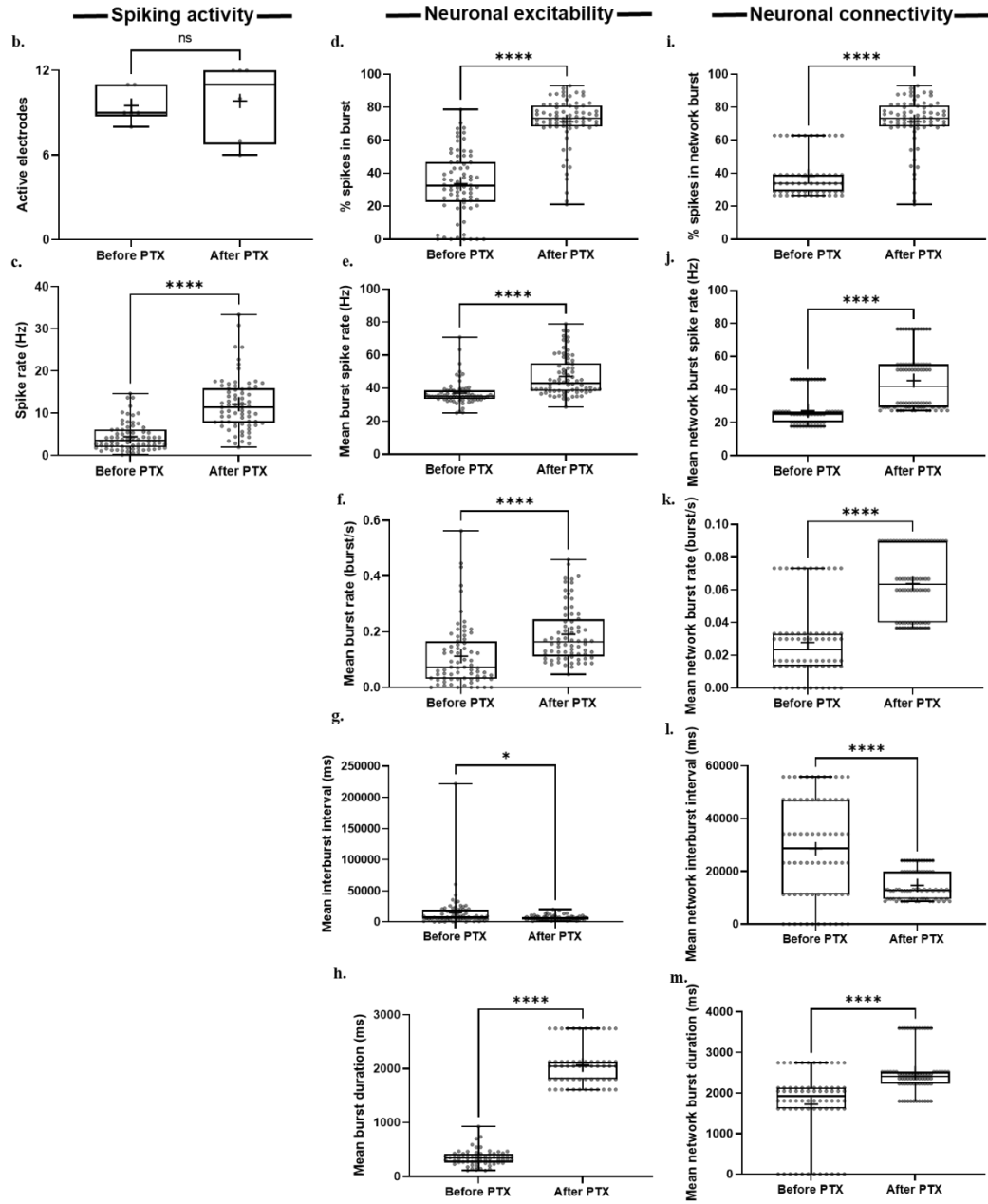


Figure 2-17 The effects of PTX on increasing MSNs activity parameters DIV34. (a) Representative raster plots from well C6 of MSNs on DIV34 before (baseline) and after the addition of 10 μ M PTX. (b-m) Unpaired t-test was used to determine significance ($p > 0.05$) after the addition of PTX ($n_{\text{wells}} = 6$, $n_{\text{electrodes}} = 72$) across all 12 parameters of activity.

2.4 Discussion

This study showed results describing the development profile of network activity in 24-well MEA plates during the first 7-19 DIV for dissociated, primary cortical neurons and 1-34 DIV for MSNs differentiated from iPSCs. The results demonstrated a rapid development of spontaneous spiking, bursting and network activity behavior that stabilized within DIV10-DIV19 for cortical neurons and DIV8-DIV30 for MSNs. Furthermore, the results from the three batches of cortical neurons demonstrated that considering multiple parameters of spiking, bursting, network properties, variability analysis, and PCA classifications are reliable predictors of robust MEA parameters that describe a stable neuronal network at the well and batch levels. We also observed stimuli evoked behavior of cortical neurons to perform pilot studies to establish MEAs as a mechanistic tool for future comparison to diseased neuron states. Overall, our study offers a high-throughput method to single-well systems to study spontaneous network development and future manipulations with drugs, chemicals, and stimuli in diseased phenotypes.

It is crucial to accurately analyze the raw data for multiple parameters that describe network activity. Analysis settings for data extraction can greatly influence the results. We utilized Butterworth high pass and low pass filter settings that were comparable to other studies [115], [108] as well as minimum amplitude of 10 μ V to allow the range of information in the form of activity needed in this study to pass for quantitation. It is important to note that network bursts exhibited by dissociated cortical neurons could be

incorrectly detected by commonly used settings and needed to be adjusted according to what was seen from the raw data.

Previous studies on *in vitro* cortical and hippocampal network development have demonstrated that spontaneous, neuronal activity evolves from random, single spiking on a few electrodes over a period of 2-3 weeks, to bursting activity that synchronizes into stable network bursts [72], [116], [117], [118], [119], [120]. Another study revealed that spiking activity developing into synchronized bursting and network bursting occurred DIV5-DIV12 with reference to the 12 parameters that we utilized for our study [108]. Our data was consistent with that of other laboratories given we had a stable number of active electrodes DIV7-DIV19 and that we saw all 12 parameters of neuronal activity stabilize by DIV14 and stay stable till DIV19 of the temporal analysis [116], [121], [120]. In fact, our cortical neuron networks stabilized 5 DIV earlier then what was previously reported by Charlesworth et al., 2015 and Cotterill et al., 2016. Also the development of our network activity matured earlier then what has been reported with immunocytochemical characterization on DIV28 [122], functional network characterization after DIV28 [123], long-term activity-dependent plasticity characterization after 2 to 3 weeks [124], and spatial-temporal electrical stimuli shape characterization between 3-5 weeks of growth [125]. Factors that could contribute to these differences include the age of the isolated cells (postnatal day 0 versus embryonic day 18) as well as plating density (50,000 versus 150,000 cells) [108], [117], [126]. In terms of the cell density, we plated 150,000 cells per well which could have contributed to the rapid development and stabilization of network

activity given that the neurons are spatially closer together to form synaptic connections. This more rapid development of stable network activity can be beneficial from a screening standpoint since it would shorten assay times, increase throughput, and decrease the overall cost of the experiment.

A factor that can influence the results of MEA activity is batch-to-batch variability. Typically, one plate is available for a given batch of cells and evidence has shown that data sets with three plates from several different batches have greater culture-to-culture variability compared to plate-to-plate or well-to-well variability from a single batch [108]. Thus, obtaining replicate values for a particular assay across several wells and plates originating from one batch would be preferable to obtaining replicate values across several different batches [127]. In our study, we utilized a postnatal-day 1 and three embryonic day 18 cortical batches to quantify neuronal activity variations from these different batches. The use of descriptive analysis methods such as range, coefficient of variation, and PCA indicated that the parameters measured from MEA activity in these batches could be narrowed down to the most robust parameters as well as visualize any variations in the MEA activity amongst the four batches that were examined. The coefficient of network interburst interval has been used to predict cortical culture age [108], differentiate a hippocampal from a cortical network [120], and to determine the most robust parameters of a human neuronal network [115]. In our study, we used it to differentiate the regularity of the network's interburst interval amongst our four batches within a similar stable time window. A study using human neuronal networks from iPSCs concluded that the

coefficient of network interburst interval used for meta-analysis was more variable batch-to-batch [115]. We also saw the high variability with the coefficient of variation between our batches with batches 1, 3 and 4 having more similar variability values compared to batch 2. Although batch 2 and 3 showed a regular network interburst interval across all DIVs, batch 1 and batch 4 showed irregularly on DIV 10, 11, 13, and 19 indicating that this was not related to network maturation. Based on our results, we concluded that this parameter would not be sufficient to differentiate the age of isolated cortical cells nor the DIV of the MEA activity. Additionally, the coefficient of network interburst interval would not be a robust parameter to characterize a stable cortical network.

Multiple, measurable parameters should be utilized to narrow down the most robust MEA activity parameters within a stable time window so that MEAs with stable neuronal networks can be utilized for drug and chemical development, neurotoxicity screening, and identifying functional changes in diseased phenotypes [108], [120], [126]. It is common in the literature to extract the mean firing rate (AKA spike rate) as a parameter to describe the general level of activity [128], [129], [130] or to describe drug or chemically induced alternations in the network [131], [132], [126], [133], [122]. Our data showed that the spike rate was highly variable across the four batches within the stable time windows of DIV10-DIV19. This result was consistent with results seen from pooled human induced pluripotent stem cells grown DIV27-35 [115] indicating its variability across cell type and origin. Thus, this parameter should be interpreted with caution. Given that classification techniques are proven to reliably predict neuronal network age utilizing three to wells per

plate when considering all parameters [108], we utilized 4 batches of six to 24 wells of dissociated cortical neurons to consider all MEA activity parameters with descriptive analysis to determine variability between batches. Interestingly, we found that the mean interburst interval was the most variable parameter between batches 1-4. Indeed, parameters with high variability, including mean burst rate, mean interburst interval, spike rate, mean network interburst interval showed similar variations in batch 1, 3, and 4 compared to the lower variation seen with batch 2. These results indicated batch-to-batch variation rather than an isolated cell age variation. The most robust parameters that aided with identifying stable network activity between different batches were % spikes in network burst, mean burst spike rate, % spike in burst, mean network burst duration, mean network burst spike rate, and mean burst duration. This indicated that using multiple parameters classified as neuronal activity, excitability, and connectivity will provide more robust discrimination in the stability amongst different batches then relying on a single or a few parameters [134]. It is also important to note that three of the six robust parameters categorized as neuronal connectivity, indicating structural evidence of anatomical, functional, synaptic network connectivity within electrophysiological parameters [108], [56], [57].

In vivo, spontaneous activity is crucial for the early development of neuronal networks [135], [136], [137]. Later in development, the contribution of the spontaneous activity in modifying brain connectivity will decrease concurrently with the increase in neuronal plasticity due to sensory inputs [138], [139]. Given that we had identified a time

window of stable, spontaneous MEA activity DIV10-DIV19 for the dissociated cortical neurons, we explored the effects of electrical stimulation to observe evoked spiking activity and to verify if this evoke activity was electrically related or synoptically related. We utilized 15 stimulation protocols to explore increasing pulse width and increasing voltage on our dissociated cortical neurons. In the literature, direct responses to electrical stimuli have been characterized to occur in the first 10-20 ms post-stimulus in MEAs with 2-3 week old cortical cells [113]. Direct responses are understood to be an antidromic response that goes away from the axons terminal and towards the soma as a result of excitation through an axon near the stimulating electrode [113]. In contrast, early post-synaptic spikes, which depend on glutamatergic synapses, occur between 5 and 50 ms post-stimulation [113]. Culture-wide barrages are activity that spreads across the entire MEA and can initiate immediately after the stimulation or occur 100ms or more after stimulation [113]. The type of stimulation parameters greatly influence the ability of stimuli to elicit action potentials. It was demonstrated that positive-to-negative voltage, biphasic pulses were very effective at eliciting action potentials [113]. Thus, we utilized symmetric positive-than-negative voltage pulses of 100, 250, and 500 μ s in duration with 100, 300, 500, 700, or 900 mV magnitudes per phase which were similar protocols utilized in other studies to elicit electrically evoked activity [113], [140], [125]. Our PSTH graphs, which were utilized to show the peak time of when the cortical network responded to the stimuli, suggested that 100 μ s pulse widths at all magnitudes used elicited a similar responses across the 100, 300, 500, 700, and 900 mV. In the literature, 400 μ s positive-then-negative

pulses with increasing magnitudes from 100 to 900 mV showed positive, correlated increases in direct spikes [113]. In the same study, pulse durations up to 300 μ s positively correlated with increasing direct responses while pulse durations 400-800 μ s plateaued the number of direct responses [113]. The plateau seen in the direct responses was due to the fact that wider pulse widths obscure early responses because of stimulation artifacts [113]. We showed that pulse widths of 250 μ s and 500 μ s decreased the number of evoked responses with the 300, 500, 700, and 900 mV magnitudes. Extracellular stimulations and recordings of neuronal activity can act on different sites of a neuron [141], [140]. One study showed the ability to detect evoked activity in a 60 electrode array was not consistent across all electrodes depending on cell density as well as the location of the neurons with respect to the electrodes [140]. For example, action potentials on the soma can produce a larger signal on the extracellular electrode compared to an axon since more ions are needed to depolarize the larger surface area and vice versa [140]. From the same study it was noted that increased electrode spacing may lead to longer detectable latencies due to the geometry of the MEA-60 [140]. Also, direct evoked responses might be induced in the middle of axons that passed near an electrodes which would increase the actual delay from the neuron to its post-synaptic target [140]. Our raw data showed that all of the recording electrodes across all 12 wells recorded spiking activity during the first 10 ms indicating an optimal cell density. However, upon further examination of this detected activity, we found that the first 60 ms of the recording consisted of artifacts from the five burst, especially with longer pulses which was consistent with findings from Wagenaar et al., 2004.

To differentiate and verify that the response we saw from our 15 stimulation parameters were directly-evoked or synaptically-evoked action potentials, we utilized agonist against excitatory neuron receptors AMPA and NMDA. AMPA and NMDA agonists are known to only block synaptic activity, not electrical transmissions [113]. However, we noted from our pilot study that there was no evoked direct activity. Thus, our conclusion of our 15 pilot electrical stimulation protocols may have evoked direct responses that were obscured by the stimulation artifacts of the 5 pulses that was excluded in the first 60 ms of spikes/s used for the PSTH data. Our second conclusion was that our 15 pilot electrical stimulations evoked glutamatergic based transmission given that AMPA and NMDA are agonist of glutamatergic receptors for post-synaptic transmission. We would need to do additional pilot studies using a single pulse instead of 5 pulses with all 15 stimulation protocols. This would help us determine if reducing the amount of stimulation artifacts would allow us to tease out electrical responses at an early latency time frame compared to the stimuli.

Human induced-pluripotent stem cells can be differentiated into central nerve cells [142], [143], [144] and form functional synaptic connections that establish a functional neuronal network *in vitro* [143], [145], [146], [147]. Furthermore, electrophysiological studies have demonstrated that iPSC derived neurons emit synchronized spiking activity [145], [148] indicating their differentiation and ability to form functional synaptic connection with other neurons. Thus, we utilized a batch of MSNs derived from human iPSCs as a comparison to the dissociated cortical neurons to observe the electrical

physiological differences between a mixed neuronal population (dissociated cortical neurons) and a pure neurons cell population free of any non-neuronal populations. It was noted that mean burst spike rate, and mean interburst interval were stable from DIV1 while parameters such as mean burst duration and mean network burst duration were stable by DIV26. The other parameters stabilized between DIV8 to DIV12. Compared to the cortical neurons, MSNs require a larger window of DIVs (DIV8-DIV26) for some of the parameters to reach stabilization. One thing to note was that most of the parameters from the neuronal connectivity category were immediately stable as soon as they could be measured by the MEA. This immediate formation of neuronal network activity was more rapid than that seen in literature with iPSCs whose neuronal networks stabilize between DIV27-DIV35 [115]. More batches would need to be measured to confirm the stable time window for our MSNs since many factors can influence a stable time window for network activity from iPSCs. These factors could include the cell density [115], the maturation time due to small-molecule supplementation protocols [149], and the type of cell adhesion molecule used to mature the cell culture [150].

In the striatum, MSNs consist of 90% of the neuronal population [151]. Their membrane potentials oscillate between a hyperpolarized state that requires excitatory cortical inputs and a depolarized state [152]. Thus, cortical inputs disrupt these oscillations through GABAergic synapses from interneurons which are highly interconnected with MSNs and modulate the excitability of MSNs [151], [153]. Picrotoxin is an antagonist of GABA_A receptors which are the primary mediators of inhibitory neurotransmission [154].

In this experiment, we wanted to observe if there was an increase in the MEA activity of MSNs when their inhibitory GABA receptor was blocked by the picrotoxin. The results indicated that the MSNs were able to receive excitatory glutamatergic signals from cortical neurons. Parameters referring to synaptic excitability and connectivity were significantly increased after picrotoxin. It was also noted that the interburst interval and network interburst interval significantly decreased with the increase in bursting activity indicating a more rapid, synchronized network bursting rather than an increase of random spiking activity with the picrotoxin. This observation was also confirmed with the significant increase seen in the mean burst duration and mean network burst duration. Overall, we showed that our MSN batch had a highly organized network activity, that the MSNs expressed GABA receptors, and that these MSNs were expressing an inhibitory, GABAergic phenotype.

2.5 Conclusions

In conclusion, we have described the early development of neural networks cultured in 24-well MEA plates. This development was qualitatively equivalent to single-well MEAs but with an increased amount of neuronal activity information retrieved compared to a single batch of cells. We also demonstrated that using differently aged dissociated cells did not contribute to any statistically distinct variations amongst the multi-parametric evaluation of neuronal spiking, excitability, or connectivity parameters. We also have begun pilot studies to into evoked responses via stimulation to establish the

MEA as a mechanistic tool to bridge molecular and phenotypic network activity to look at the potential for diseases to disrupt that activity.

2.6 Future directions

To establish a functional link between molecular changes and neuronal activity, we will utilize the MEA platform as an approach to study how molecular changes lead to neuronal activity changes in neurodegenerative disease, such as Huntington's disease and Alzheimer's disease.

3 APPENDICES

Appendix A. List of Published Papers

1. Abd, M.A., Al-Saidi, M., Lin, M., **Liddle, G.**, Mondal, K. and Engeberg, E.D., 2020. Surface Feature Recognition and Grasped Object Slip Prevention with a Liquid Metal Tactile Sensor for a Prosthetic Hand. In *2020 8th IEEE RAS/EMBS International Conference for Biomedical Robotics and Biomechatronics (BioRob)* (pp. 1174-1179). IEEE.
2. **Liddle, G.**, Wei, J., Hartmann, J., 2022. Cancer therapy, immunotherapy, photothermal therapy. Ghenadii Korotcenkv & Kunal Mondal (Ed.). Metal Oxides for Biomedical and Biosensor Applications. (1st ed., pp. 85-102). Cambridge, MA: *Elsevier*

Appendix B. List of Papers Under-Preparation

3. **Genevieve M. Abd**, Moaed A. Abd, Maohua Lin, Jianning Wei, E Du, Emmanuelle Tognoli, Erik Engeberg, “Structural (re)generation of cultured Dorsal Root Ganglion neurons in response to biological action potential-like stimuli” under preparation.
4. **Genevieve Abd**, Anju Gupta, Tagbo H. R. Niepa, Seeram Ramakrishna, Ashutosh Sharma, and Kunal Mondal. “Carbon-based Electrically Conductive Scaffolds for Tissue Engineering and Regenerative Medicine” 2022

4 REFERENCES

- [1] P. J. Kumar, R. D. Adams, A. B. Harkins, E. D. Engeberg, and R. K. Willits, “Stimulation Frequency Alters the Dorsal Root Ganglion Neurite Growth and Directionality In Vitro,” *IEEE Trans. Biomed. Eng.*, vol. 63, no. 6, pp. 1257–1268, Jun. 2016, doi: 10.1109/TBME.2015.2492998.
- [2] S. Han, D. H. Kim, J. Sung, H. Yang, J. W. Park, and I. Youn, “Electrical stimulation accelerates neurite regeneration in axotomized dorsal root ganglion neurons by increasing MMP-2 expression,” *Biochem. Biophys. Res. Commun.*, vol. 508, no. 2, pp. 348–353, Jan. 2019, doi: 10.1016/j.bbrc.2018.11.159.
- [3] M. Wood and R. K. Willits, “Short-duration, DC electrical stimulation increases chick embryo DRG neurite outgrowth,” *Bioelectromagnetics*, vol. 27, no. 4, pp. 328–331, May 2006, doi: 10.1002/bem.20214.
- [4] M. D. Wood and R. K. Willits, “Applied electric field enhances DRG neurite growth: Influence of stimulation media, surface coating and growth supplements,” *J. Neural Eng.*, vol. 6, no. 4, 2009, doi: 10.1088/1741-2560/6/4/046003.
- [5] T. M. Brushart, R. Jari, V. Verge, C. Rohde, and T. Gordon, “Electrical stimulation restores the specificity of sensory axon regeneration,” *Exp. Neurol.*, vol. 194, no. 1, pp. 221–229, Jul. 2005, doi: 10.1016/j.expneurol.2005.02.007.

- [6] T. Gordon, “Electrical Stimulation to Enhance Axon Regeneration After Peripheral Nerve Injuries in Animal Models and Humans,” *Neurotherapeutics*, vol. 13, no. 2. Springer New York LLC, pp. 295–310, 01-Apr-2016, doi: 10.1007/s13311-015-0415-1.
- [7] S. Han, D. H. Kim, J. Sung, H. Yang, J. W. Park, and I. Youn, “Electrical stimulation accelerates neurite regeneration in axotomized dorsal root ganglion neurons by increasing MMP-2 expression,” *Biochem. Biophys. Res. Commun.*, vol. 508, no. 2, pp. 348–353, Jan. 2019, doi: 10.1016/j.bbrc.2018.11.159.
- [8] Y. Zhang *et al.*, “VDR Status Arbitrates the Prometastatic Effects of Tumor-Associated Macrophages,” *Mol. cancer Res.*, no. 13, pp. 1181–1191, 2014, doi: 10.1158/1541-7786.MCR-14-0036.
- [9] B. Greenebaum *et al.*, “Effects of pulsed magnetic fields on neurite outgrowth from chick embryo dorsal root ganglia,” *Bioelectromagnetics*, vol. 17, no. 4, pp. 293–302, Jan. 1996, doi: 10.1002/(SICI)1521-186X(1996)17:4<293::AID-BEM5>3.0.CO;2-Z.
- [10] M. Y. Macias, J. H. Battocletti, C. H. Sutton, F. A. Pintar, and D. J. Maiman, “Directed and enhanced neurite growth with pulsed magnetic field stimulation,” *Bioelectromagnetics*, vol. 21, no. 4, pp. 272–286, May 2000, doi: 10.1002/(SICI)1521-186X(200005)21:4<272::AID-BEM4>3.0.CO;2-5.
- [11] M. P. Willand, M. A. Nguyen, G. H. Borschel, and T. Gordon, “Electrical Stimulation to Promote Peripheral Nerve Regeneration,” *Neurorehabil. Neural*

- Repair*, vol. 30, no. 5, pp. 490–496, Jun. 2016, doi: 10.1177/1545968315604399.
- [12] N. L. U. Van Meeteren, J. H. Brakkee, F. P. T. Hamers, P. J. M. Helders, and W. H. Gispen, “Exercise training improves functional recovery and motor nerve conduction velocity after sciatic nerve crush lesion in the rat,” *Arch. Phys. Med. Rehabil.*, vol. 78, no. 1, pp. 70–77, 1997, doi: 10.1016/S0003-9993(97)90013-7.
- [13] R. Molteni, J. Q. Zheng, Z. Ying, F. Gómez-Pinilla, and J. L. Twiss, “Voluntary exercise increases axonal regeneration from sensory neurons,” *Proc. Natl. Acad. Sci. U. S. A.*, vol. 101, no. 22, pp. 8473–8478, Jun. 2004, doi: 10.1073/pnas.0401443101.
- [14] T. Marqueste, J. R. Alliez, O. Alluin, Y. Jammes, and P. Decherchi, “Neuromuscular rehabilitation by treadmill running or electrical stimulation after peripheral nerve injury and repair,” *J. Appl. Physiol.*, vol. 96, no. 5, pp. 1988–1995, May 2004, doi: 10.1152/jappphysiol.00775.2003.
- [15] E. Asensio-Pinilla, E. Udina, J. Jaramillo, and X. Navarro, “Electrical stimulation combined with exercise increase axonal regeneration after peripheral nerve injury,” *Exp. Neurol.*, vol. 219, no. 1, pp. 258–265, Sep. 2009, doi: 10.1016/j.expneurol.2009.05.034.
- [16] N. M. Geremia, T. Gordon, T. M. Brushart, A. A. Al-Majed, and V. M. K. Verge, “Electrical stimulation promotes sensory neuron regeneration and growth-associated gene expression,” *Exp. Neurol.*, vol. 205, no. 2, pp. 347–359, Jun. 2007, doi: 10.1016/j.expneurol.2007.01.040.

- [17] A. A. Al-Majed, T. M. Brushart, and T. Gordon, "Electrical stimulation accelerates and increases expression of BDNF and trkB mRNA in regenerating rat femoral motoneurons," *Eur. J. Neurosci.*, vol. 12, no. 12, pp. 4381–4390, Dec. 2000, doi: 10.1111/j.1460-9568.2000.01341.x.
- [18] S. L. Tam, V. Archibald, B. Jassar, N. Tyreman, and T. Gordon, "Increased neuromuscular activity reduces sprouting in partially denervated muscles," *J. Neurosci.*, vol. 21, no. 2, pp. 654–667, Jan. 2001, doi: 10.1523/jneurosci.21-02-00654.2001.
- [19] L. T. Siu and T. Gordon, "Mechanisms controlling axonal sprouting at the neuromuscular junction," *Journal of Neurocytology*, vol. 32, no. 5–8, J Neurocytol, pp. 961–974, Jun-2003, doi: 10.1023/B:NEUR.0000020635.41233.0f.
- [20] R. E. Burke, "Motor Units: Anatomy, Physiology, and Functional Organization," in *Comprehensive Physiology*, Hoboken, NJ, USA: John Wiley & Sons, Inc., 2011, pp. 345–422.
- [21] D. Ventre, M. Puzan, E. Ashbolt, and A. Koppes, "Enhanced total neurite outgrowth and secondary branching in dorsal root ganglion neurons elicited by low intensity pulsed ultrasound," *J. Neural Eng.*, vol. 15, no. 4, 2018, doi: 10.1088/1741-2552/aabebe.
- [22] M. Imaninezhad, K. Pemberton, F. Xu, K. Kalinowski, R. Bera, and S. P. Zustiak, "Directed and enhanced neurite outgrowth following exogenous electrical stimulation on carbon nanotube-hydrogel composites," *J. Neural Eng.*, vol. 15, no.

5, 2018, doi: 10.1088/1741-2552/aad65b.

- [23] K. B. Chapman, T. A. Yousef, A. Foster, M. D. Stanton-Hicks, and N. van Helmond, “Mechanisms for the Clinical Utility of Low-Frequency Stimulation in Neuromodulation of the Dorsal Root Ganglion,” *Neuromodulation*, vol. 24, no. 4, pp. 738–745, 2021, doi: 10.1111/ner.13323.
- [24] A. R. Kent, X. Min, Q. H. Hogan, and J. M. Kramer, “Mechanisms of Dorsal Root Ganglion Stimulation in Pain Suppression: A Computational Modeling Analysis,” *Neuromodulation*, vol. 21, no. 3, pp. 234–246, 2018, doi: 10.1111/ner.12754.
- [25] A. S. Koopmeiners, S. Mueller, J. Kramer, and Q. H. Hogan, “Effect of Electrical Field Stimulation on Dorsal Root Ganglion Neuronal Function,” *Neuromodulation Technol. Neural Interface*, vol. 16, no. 4, pp. 304–311, Jul. 2013, doi: 10.1111/ner.12028.
- [26] T. Gordon, E. Udina, V. M. K. Verge, and E. I. Posse De Chaves, “Brief electrical stimulation accelerates axon regeneration in the peripheral nervous system and promotes sensory axon regeneration in the central nervous system,” *Motor Control*, vol. 13, no. 4. Human Kinetics Publishers Inc., pp. 412–441, 2009, doi: 10.1123/mcj.13.4.412.
- [27] C. H. Kao, J. J. J. Chen, Y. M. Hsu, D. T. Bau, C. H. Yao, and Y. S. Chen, “High-frequency electrical stimulation can be a complementary therapy to promote nerve regeneration in diabetic rats,” *PLoS One*, vol. 8, no. 11, Nov. 2013, doi: 10.1371/journal.pone.0079078.

- [28] X. Yan *et al.*, “Electrical stimulation induces calcium-dependent neurite outgrowth and immediate early genes expressions of dorsal root ganglion neurons,” *Neurochem. Res.*, vol. 39, no. 1, pp. 129–141, Nov. 2014, doi: 10.1007/s11064-013-1197-7.
- [29] B. Greenebaum *et al.*, “Effects of pulsed magnetic fields on neurite outgrowth from chick embryo dorsal root ganglia,” *Bioelectromagnetics*, vol. 17, no. 4, pp. 293–302, 1996, doi: 10.1002/(SICI)1521-186X(1996)17:4<293::AID-BEM5>3.0.CO;2-Z.
- [30] E. M. Izhikevich, “Simple Model of Spiking Neurons,” *IEEE Trans. NEURAL NETWORKS*, vol. 14, no. 6, 2003, doi: 10.1109/TNN.2003.820440.
- [31] S. Mahnič-Kalamiza and D. Miklavčič, “Scratching the electrode surface: Insights into a high-voltage pulsed-field application from in vitro & in silico studies in indifferent fluid,” *Electrochim. Acta*, vol. 363, p. 137187, Dec. 2020, doi: 10.1016/j.electacta.2020.137187.
- [32] J. N. Sleigh, G. A. Weir, and G. Schiavo, “A simple, step-by-step dissection protocol for the rapid isolation of mouse dorsal root ganglia,” *BMC Res. Notes*, vol. 9, no. 1, Feb. 2016, doi: 10.1186/s13104-016-1915-8.
- [33] N. Huang, C. Erie, M. L. Lu, and J. Wei, “Aberrant subcellular localization of SQSTM1/p62 contributes to increased vulnerability to proteotoxic stress recovery in Huntington’s disease,” *Mol. Cell. Neurosci.*, vol. 88, pp. 43–52, Apr. 2018, doi: 10.1016/j.mcn.2017.12.005.

- [34] S. Y. Ho, C. Y. Chao, H. L. Huang, T. W. Chiu, P. Charoenkwan, and E. Hwang, "NeurphologyJ: An automatic neuronal morphology quantification method and its application in pharmacological discovery," *BMC Bioinformatics*, vol. 12, 2011, doi: 10.1186/1471-2105-12-230.
- [35] A. M. Rajnicek, K. R. Robinson, and C. D. McCaig, "The direction of neurite growth in a weak DC electric field depends on the substratum: Contributions of adhesivity and net surface charge," *Dev. Biol.*, vol. 203, no. 2, pp. 412–423, 1998, doi: 10.1006/dbio.1998.9039.
- [36] I. Rishal and M. Fainzilber, "Axon–soma communication in neuronal injury," *Nat. Rev. Neurosci.* 2013 151, vol. 15, no. 1, pp. 32–42, Dec. 2013, doi: 10.1038/nrn3609.
- [37] T. A, "Tuning the orchestra: transcriptional pathways controlling axon regeneration," *Front. Mol. Neurosci.*, vol. 4, no. JANUARY 2012, 2012, doi: 10.3389/FNMOL.2011.00060.
- [38] K. L. LANKFORD, S. G. WAXMAN, and J. D. KOCSIS, "Mechanisms of Enhancement of Neurite Regeneration In Vitro Following a Conditioning Sciatic Nerve Lesion," *J. Comp. Neurol.*, vol. 391, no. 1, p. 11, Feb. 1998.
- [39] S. Zhou *et al.*, "microRNA-222 Targeting PTEN Promotes Neurite Outgrowth from Adult Dorsal Root Ganglion Neurons following Sciatic Nerve Transection," *PLoS One*, vol. 7, no. 9, p. e44768, Sep. 2012, doi: 10.1371/JOURNAL.PONE.0044768.

- [40] K. MJ *et al.*, “Contribution of macrophages to enhanced regenerative capacity of dorsal root ganglia sensory neurons by conditioning injury,” *J. Neurosci.*, vol. 33, no. 38, pp. 15095–15108, 2013, doi: 10.1523/JNEUROSCI.0278-13.2013.
- [41] A. Conte, N. Khan, G. Defazio, J. C. Rothwell, and A. Berardelli, “Pathophysiology of somatosensory abnormalities in Parkinson disease,” *Nature Reviews Neurology*, vol. 9, no. 12. Nature Publishing Group, pp. 687–697, 12-Dec-2013, doi: 10.1038/nrneurol.2013.224.
- [42] M. Paoloni, B. Volpe, M. Mangone, F. Ioppolo, and V. Santilli, “Peripheral Nerve Conduction Abnormalities in Nonparetic Side of Ischemic Stroke Patients,” *J. Clin. Neurophysiol.*, vol. 27, no. 1, pp. 48–51, Feb. 2010, doi: 10.1097/WNP.0b013e3181cb42ae.
- [43] M. G. Fehlings, C. H. Tator, and R. D. Linden, “The relationships among the severity of spinal cord injury, motor and somatosensory evoked potentials and spinal cord blood flow,” *Electroencephalogr. Clin. Neurophysiol. Evoked Potentials*, vol. 74, no. 4, pp. 241–259, Jul. 1989, doi: 10.1016/0168-5597(89)90055-5.
- [44] M. Siemionow and G. Brzezicki, “Chapter 8 Current Techniques and Concepts in Peripheral Nerve Repair,” *International Review of Neurobiology*, vol. 87, no. C. Int Rev Neurobiol, pp. 141–172, 2009, doi: 10.1016/S0074-7742(09)87008-6.
- [45] A. N. Koppes, A. M. Seggio, and D. M. Thompson, “Neurite outgrowth is significantly increased by the simultaneous presentation of Schwann cells and

- moderate exogenous electric fields,” *J. Neural Eng.*, vol. 8, no. 4, p. 046023, Jun. 2011, doi: 10.1088/1741-2560/8/4/046023.
- [46] H.-L. Su *et al.*, “Late administration of high-frequency electrical stimulation increases nerve regeneration without aggravating neuropathic pain in a nerve crush injury,” *BMC Neurosci.* 2018 191, vol. 19, no. 1, pp. 1–12, Jun. 2018, doi: 10.1186/S12868-018-0437-9.
- [47] Q. Zhang, S. Beirne, K. Shu, D. Esrafilzadeh, X.-F. Huang, and G. G. Wallace, “Electrical Stimulation with a Conductive Polymer Promotes Neurite Outgrowth and Synaptogenesis in Primary Cortical Neurons in 3D,” *Sci. Reports* 2018 81, vol. 8, no. 1, pp. 1–10, Jun. 2018, doi: 10.1038/s41598-018-27784-5.
- [48] Y. J. Chang, C. M. Hsu, C. H. Lin, M. S. C. Lu, and L. Chen, “Electrical stimulation promotes nerve growth factor-induced neurite outgrowth and signaling,” *Biochim. Biophys. Acta - Gen. Subj.*, vol. 1830, no. 8, pp. 4130–4136, Aug. 2013, doi: 10.1016/J.BBAGEN.2013.04.007.
- [49] L. Yu *et al.*, “Dorsal root ganglion progenitors differentiate to gamma-aminobutyric acid- and choline acetyltransferase-positive neurons,” *Neural Regen. Res.*, vol. 7, no. 7, p. 485, Mar. 2012, doi: 10.3969/J.ISSN.1673-5374.2012.07.001.
- [50] U. De, K. A.-P. in clinical and biological research, and undefined 1986, “Quantitative analyses of filopodial activity of mammalian neuronal growth cones, in exogenous, electrical fields.,” *europemc.org*.
- [51] C. M. Loya, D. Van Vactor, and T. A. Fulga, “Understanding neuronal connectivity

- through the post-transcriptional toolkit,” *Genes Dev.*, vol. 24, no. 7, pp. 625–635, Apr. 2010, doi: 10.1101/GAD.1907710.
- [52] E. Salinas and T. J. Sejnowski, “CORRELATED NEURONAL ACTIVITY AND THE FLOW OF NEURAL INFORMATION,” *Nat. Rev. Neurosci.*, vol. 2, no. 8, p. 539, Aug. 2001, doi: 10.1038/35086012.
- [53] B. Wamsley and G. Fishell, “Genetic and activity-dependent mechanisms underlying interneuron diversity,” *Nat. Rev. Neurosci.* 2017 185, vol. 18, no. 5, pp. 299–309, Apr. 2017, doi: 10.1038/nrn.2017.30.
- [54] H. Markram, “Organizing principles for a diversity of GABAergic interneurons and synapses in the neocortex,” *Science (80-.)*, vol. 287, no. 5451, pp. 273–278, 2000, doi: 10.1126/SCIENCE.287.5451.273/ASSET/C52B865B-ED06-4E70-9841-90A4B7259380/ASSETS/GRAPHIC/SE0108184006.JPEG.
- [55] G. Buzsáki and J. J. Chrobak, “Temporal structure in spatially organized neuronal ensembles: a role for interneuronal networks,” *Curr. Opin. Neurobiol.*, vol. 5, no. 4, pp. 504–510, 1995, doi: 10.1016/0959-4388(95)80012-3.
- [56] S. Ito *et al.*, “Large-Scale, High-Resolution Multielectrode-Array Recording Depicts Functional Network Differences of Cortical and Hippocampal Cultures,” *PLoS One*, vol. 9, no. 8, p. 105324, Aug. 2014, doi: 10.1371/JOURNAL.PONE.0105324.
- [57] S. Feldt, P. Bonifazi, and R. Cossart, “Dissecting functional connectivity of neuronal microcircuits: experimental and theoretical insights,” *Trends Neurosci.*,

- vol. 34, no. 5, pp. 225–236, May 2011, doi: 10.1016/J.TINS.2011.02.007.
- [58] K. J. Friston, “Functional and Effective Connectivity: A Review,” doi: 10.1089/brain.2011.0008.
- [59] S. Song, K. D. Miller, and L. F. Abbott, “Competitive Hebbian learning through spike-timing-dependent synaptic plasticity,” *Nat. Neurosci.*, vol. 3, no. 9, pp. 919–926, Sep. 2000, doi: 10.1038/78829.
- [60] D. N. Abrous, M. Koehl, and M. Le Moal, “Adult neurogenesis: From precursors to network and physiology,” *Physiol. Rev.*, vol. 85, no. 2, pp. 523–569, Apr. 2005, doi: 10.1152/PHYSREV.00055.2003/ASSET/IMAGES/LARGE/Z9J0020503540008.JPEG.
- [61] X. Navarro, M. Vivó, and A. Valero-Cabré, “Neural plasticity after peripheral nerve injury and regeneration,” *Progress in Neurobiology*, vol. 82, no. 4. Pergamon, pp. 163–201, 01-Jul-2007, doi: 10.1016/j.pneurobio.2007.06.005.
- [62] D. E. Feldman, “Synaptic mechanisms for plasticity in neocortex,” *Annu. Rev. Neurosci.*, vol. 32, pp. 33–55, Jun. 2009, doi: 10.1146/ANNUREV.NEURO.051508.135516.
- [63] L. Oberman and A. Pascual-Leone, “Changes in plasticity across the lifespan: Cause of disease and target for intervention,” *Prog. Brain Res.*, vol. 207, pp. 91–120, 2013, doi: 10.1016/B978-0-444-63327-9.00016-3.
- [64] T. V. P. Bliss and A. R. Gardner-Medwin, “Long-lasting potentiation of synaptic

- transmission in the dentate area of the unanaesthetized rabbit following stimulation of the perforant path,” *J. Physiol.*, vol. 232, no. 2, pp. 357–374, Jul. 1973, doi: 10.1113/JPHYSIOL.1973.SP010274.
- [65] H. Lee, E. J. Lee, Y. S. Song, and E. Kim, “Long-term depression-inducing stimuli promote cleavage of the synaptic adhesion molecule NGL-3 through NMDA receptors, matrix metalloproteinases and presenilin/ γ -secretase,” *Philos. Trans. R. Soc. B Biol. Sci.*, vol. 369, no. 1633, Jan. 2014, doi: 10.1098/RSTB.2013.0158.
- [66] F. Gobbo and A. Cattaneo, “Neuronal Activity at Synapse Resolution: Reporters and Effectors for Synaptic Neuroscience,” *Front. Mol. Neurosci.*, vol. 13, p. 184, Oct. 2020, doi: 10.3389/FNMOL.2020.572312/BIBTEX.
- [67] L. J. J. Nicolai *et al.*, “Genetically encoded dendritic marker sheds light on neuronal connectivity in *Drosophila*,” *Proc. Natl. Acad. Sci. U. S. A.*, vol. 107, no. 47, pp. 20553–20558, Nov. 2010, doi: 10.1073/PNAS.1010198107.
- [68] F. Y. Shen, M. M. Harrington, L. A. Walker, H. P. J. Cheng, E. S. Boyden, and D. Cai, “Light microscopy based approach for mapping connectivity with molecular specificity,” *Nat. Commun.* 2020 111, vol. 11, no. 1, pp. 1–12, Sep. 2020, doi: 10.1038/s41467-020-18422-8.
- [69] Y. Zang, M. Chen, S. Yang, and H. Chen, “Electro-optical neural networks based on time-stretch method,” *IEEE J. Sel. Top. Quantum Electron.*, vol. 26, no. 1, pp. 1–10, Jan. 2020, doi: 10.1109/JSTQE.2019.2957446.
- [70] F. Rothganger, C. E. Warrender, D. Trumbo, and J. B. Aimone, “N2A: A

computational tool for modeling from neurons to algorithms,” *Front. Neural Circuits*, vol. 8, no. JAN, p. 1, Jan. 2014, doi: 10.3389/FNCIR.2014.00001/ABSTRACT.

- [71] M. E. J. Obien, K. Deligkaris, T. Bullmann, D. J. Bakkum, and U. Frey, “Revealing neuronal function through microelectrode array recordings,” *Frontiers in Neuroscience*, vol. 9, no. JAN. Frontiers Media S.A., p. 423, 2015, doi: 10.3389/fnins.2014.00423.
- [72] J. Van Pelt, I. Vajda, P. S. Wolters, M. A. Corner, and G. J. A. Ramakers, “Dynamics and plasticity in developing neuronal networks in vitro,” *Prog. Brain Res.*, vol. 147, no. SPEC. ISS., pp. 171–188, 2005, doi: 10.1016/S0079-6123(04)47013-7.
- [73] E. Maeda, H. P. C. Robinson, and A. Kawana, “The mechanisms of generation and propagation of synchronized bursting in developing networks of cortical neurons,” *J. Neurosci.*, vol. 15, no. 10, pp. 6834–6845, 1995, doi: 10.1523/JNEUROSCI.15-10-06834.1995.
- [74] A. Noguchi, Y. Ikegaya, and N. Matsumoto, “In Vivo Whole-Cell Patch-Clamp Methods: Recent Technical Progress and Future Perspectives,” *Sensors (Basel)*, vol. 21, no. 4, pp. 1–21, Feb. 2021, doi: 10.3390/S21041448.
- [75] E. Journal, O. P. Hamill, A. Marty, E. Neher, B. Sakmann, and F. J. Sigworth, “Pfligers Archiv Improved Patch-Clamp Techniques for High-Resolution Current Recording from Cells and Cell-Free Membrane Patches,” vol. 391, pp. 85–100,

1981.

- [76] F. J. Sigworth and E. Neher, “Single Na⁺ channel currents observed in cultured rat muscle cells,” *Nature*, vol. 287, no. 5781, pp. 447–449, 1980, doi: 10.1038/287447A0.
- [77] E. Neher and B. Sakmann, “Single-channel currents recorded from membrane of denervated frog muscle fibres,” *Nature*, vol. 260, no. 5554, pp. 799–802, 1976, doi: 10.1038/260799A0.
- [78] M. V. Accardi, M. K. Pugsley, R. Forster, E. Troncy, H. Huang, and S. Authier, “The emerging role of in vitro electrophysiological methods in CNS safety pharmacology,” *J. Pharmacol. Toxicol. Methods*, vol. 81, pp. 47–59, Sep. 2016, doi: 10.1016/J.VASCN.2016.03.008.
- [79] R. Horn and A. Marty, “Muscarinic activation of ionic currents measured by a new whole-cell recording method,” *J. Gen. Physiol.*, vol. 92, no. 2, pp. 145–159, Aug. 1988, doi: 10.1085/JGP.92.2.145.
- [80] S. B. Kodandaramaiah, G. T. Franzesi, B. Y. Chow, E. S. Boyden, and C. R. Forest, “Automated whole-cell patch clamp electrophysiology of neurons in vivo,” *Nat. Methods*, vol. 9, no. 6, p. 585, Jun. 2012, doi: 10.1038/NMETH.1993.
- [81] R. Perin, T. K. Berger, and H. Markram, “A synaptic organizing principle for cortical neuronal groups,” *Proc. Natl. Acad. Sci. U. S. A.*, vol. 108, no. 13, pp. 5419–5424, Mar. 2011, doi: 10.1073/PNAS.1016051108.
- [82] X. Jiang, G. Wang, A. J. Lee, R. L. Stornetta, and J. J. Zhu, “The organization of

- two new cortical interneuronal circuits,” *Nat. Neurosci.*, vol. 16, no. 2, pp. 210–221, Feb. 2013, doi: 10.1038/NN.3305.
- [83] J. Negri, V. Menon, and T. L. Young-Pearse, “Assessment of spontaneous neuronal activity In vitro using multi-well multi-electrode arrays: Implications for assay development,” *eNeuro*, vol. 7, no. 1, pp. 1–27, 2020, doi: 10.1523/ENEURO.0080-19.2019.
- [84] M. E. Spira and A. Hai, “Multi-electrode array technologies for neuroscience and cardiology,” *Nat. Nanotechnol. /*, vol. 8, 2013, doi: 10.1038/NNANO.2012.265.
- [85] M. E. J. Obien, K. Deligkaris, T. Bullmann, D. J. Bakkum, and U. Frey, “Revealing neuronal function through microelectrode array recordings,” *Front. Neurosci.*, vol. 9, no. JAN, p. 423, 2015, doi: 10.3389/FNINS.2014.00423/BIBTEX.
- [86] V. J. Garcia *et al.*, “Huntington’s disease patient-derived astrocytes display electrophysiological impairments and reduced neuronal support,” *Front. Neurosci.*, vol. 13, no. JUN, p. 669, 2019, doi: 10.3389/FNINS.2019.00669/BIBTEX.
- [87] M. M. Heinricher, “Principles of Extracellular Single-Unit Recording Extracellular Recording: Neuronal Activity in a Functional Context.”
- [88] C. A. Terzuolo and T. Araki, “AN ANALYSIS OF INTRA- VERSUS EXTRACELLULAR POTENTIAL CHANGES ASSOCIATED WITH ACTIVITY OF SINGLE SPINAL MOTONEURONS*,” *Ann. N. Y. Acad. Sci.*, vol. 94, no. 2, pp. 547–558, Sep. 1961, doi: 10.1111/J.1749-6632.1961.TB35558.X.

- [89] C. T. McKee, J. A. Last, P. Russell, and C. J. Murphy, "Indentation versus tensile measurements of young's modulus for soft biological tissues," *Tissue Eng. - Part B Rev.*, vol. 17, no. 3, pp. 155–164, Jun. 2011, doi: 10.1089/TEN.TEB.2010.0520.
- [90] L. Karumbaiah, S. Norman, N. Rajan, S. A.- Biomaterials, and undefined 2012, "The upregulation of specific interleukin (IL) receptor antagonists and paradoxical enhancement of neuronal apoptosis due to electrode induced strain and," *Elsevier*.
- [91] G. Higgins *et al.*, "Biomechanical analysis of silicon microelectrode-induced strain in the brain," *iopscience.iop.org*, vol. 2, pp. 81–89, 2005, doi: 10.1088/1741-2560/2/4/003.
- [92] B. Ghane-Motlagh and M. Sawan, "A review of Microelectrode Array technologies: Design and implementation challenges," *2013 2nd Int. Conf. Adv. Biomed. Eng. ICABME 2013*, pp. 38–41, Oct. 2013, doi: 10.1109/ICABME.2013.6648841.
- [93] R. Biran, D. C. Martin, and P. A. Tresco, "Neuronal cell loss accompanies the brain tissue response to chronically implanted silicon microelectrode arrays," *Exp. Neurol.*, vol. 195, no. 1, pp. 115–126, Sep. 2005, doi: 10.1016/J.EXPNEUROL.2005.04.020.
- [94] M. E. Raichle and M. A. Mintun, "Brain Work and Brain Imaging," 2006, doi: 10.1146/annurev.neuro.29.051605.112819.
- [95] P. K. Shetty, F. Galeffi, and D. A. Turner, "Cellular Links between Neuronal Activity and Energy Homeostasis," *Front. Pharmacol.*, vol. 3, 2012, doi:

10.3389/FPHAR.2012.00043.

- [96] S. Ogawa, T. M. Lee, A. R. Kay, and D. W. Tank, “Brain magnetic resonance imaging with contrast dependent on blood oxygenation,” *Proc. Natl. Acad. Sci. U. S. A.*, vol. 87, no. 24, pp. 9868–9872, 1990, doi: 10.1073/PNAS.87.24.9868.
- [97] N. K. Logothetis, J. Pauls, M. Augath, T. Trinath, and A. Oeltermann, “Neurophysiological investigation of the basis of the fMRI signal,” *Nature*, vol. 412, no. 6843, pp. 150–157, Jul. 2001, doi: 10.1038/35084005.
- [98] M. E. Raichle, “Functional Brain Imaging and Human Brain Function,” *J. Neurosci.*, vol. 23, no. 10, pp. 3959–3962, May 2003, doi: 10.1523/JNEUROSCI.23-10-03959.2003.
- [99] N. K. Logothetis, “The underpinnings of the BOLD functional magnetic resonance imaging signal,” *J. Neurosci.*, vol. 23, no. 10, pp. 3963–3971, May 2003, doi: 10.1523/JNEUROSCI.23-10-03963.2003.
- [100] G. H. Glover, “Overview of Functional Magnetic Resonance Imaging,” *Neurosurg. Clin. NA*, vol. 22, pp. 133–139, 2011, doi: 10.1016/j.nec.2010.11.001.
- [101] C. Sun, J. S. H. Lee, and M. Zhang, “Magnetic nanoparticles in MR imaging and drug delivery,” *Advanced Drug Delivery Reviews*, vol. 60, no. 11. Elsevier, pp. 1252–1265, 17-Aug-2008, doi: 10.1016/j.addr.2008.03.018.
- [102] D. M. Mandell *et al.*, “Mapping cerebrovascular reactivity using blood oxygen level-dependent MRI in patients with arterial steno-occlusive disease: Comparison with arterial spin labeling MRI,” *Stroke*, vol. 39, no. 7, pp. 2021–2028, Jul. 2008,

doi: 10.1161/STROKEAHA.107.506709.

- [103] J. H. Kim *et al.*, “Interpreting the Entire Connectivity of Individual Neurons in Micropatterned Neural Culture With an Integrated Connectome Analyzer of a Neuronal Network (iCANN),” *Front. Neuroanat.*, vol. 15, p. 78, Oct. 2021, doi: 10.3389/FNANA.2021.746057/BIBTEX.
- [104] D. A. Wagenaar, R. Madhavan, J. Pine, and S. M. Potter, “Controlling Bursting in Cortical Cultures with Closed-Loop Multi-Electrode Stimulation,” *J. Neurosci.*, vol. 25, no. 3, p. 680, Jan. 2005, doi: 10.1523/JNEUROSCI.4209-04.2005.
- [105] J. H. Choi, J. H. Kim, R. Heo, and K. J. Lee, “Modulating the precision of recurrent bursts in cultured neural networks,” *Phys. Rev. Lett.*, vol. 108, no. 13, Mar. 2012, doi: 10.1103/PHYSREVLETT.108.138103.
- [106] J. H. Kim, R. Heo, J. H. Choi, and K. J. Lee, “Dynamic transitions among multiple oscillators of synchronized bursts in cultured neural networks,” *J. Stat. Mech. Theory Exp.*, vol. 2014, no. 4, 2014, doi: 10.1088/1742-5468/2014/04/P04019.
- [107] N. Zhang, M. C. An, D. Montoro, and L. M. Ellerby, “Characterization of Human Huntington’s Disease Cell Model from Induced Pluripotent Stem Cells,” *PLoS Curr.*, vol. 2, no. OCT, pp. 1–11, 2010, doi: 10.1371/CURRENTS.RRN1193.
- [108] E. Cotterill, D. Hall, K. Wallace, W. R. Mundy, S. J. Eglen, and T. J. Shafer, “Characterization of early cortical neural network development in multiwell microelectrode array plates,” *J. Biomol. Screen.*, vol. 21, no. 5, pp. 510–519, Jun. 2016, doi: 10.1177/1087057116640520.

- [109] G. Palm, A. M. H. J. Aertsen, and G. L. Gerstein, “On the significance of correlations among neuronal spike trains,” *Biol. Cybern.*, vol. 59, no. 1, pp. 1–11, Jun. 1988, doi: 10.1007/BF00336885.
- [110] G. W. Gross, B. K. Rhoades, D. L. Reust, and F. U. Schwalm, “Stimulation of monolayer networks in culture through thin-film indium-tin oxide recording electrodes,” *J. Neurosci. Methods*, vol. 50, no. 2, pp. 131–143, 1993, doi: 10.1016/0165-0270(93)90001-8.
- [111] Y. Jimbo and A. Kawana, “Electrical stimulation and recording from cultured neurons using a planar electrode array,” *Bioelectrochemistry Bioenerg.*, vol. 29, no. 2, pp. 193–204, 1992, doi: 10.1016/0302-4598(92)80067-Q.
- [112] M. P. Maher, J. Pine, J. Wright, and Y. C. Tai, “The neurochip: a new multielectrode device for stimulating and recording from cultured neurons,” *J. Neurosci. Methods*, vol. 87, no. 1, pp. 45–56, Feb. 1999, doi: 10.1016/S0165-0270(98)00156-3.
- [113] D. A. Wagenaar, J. Pine, and S. M. Potter, “Effective parameters for stimulation of dissociated cultures using multi-electrode arrays,” *J. Neurosci. Methods*, vol. 138, no. 1–2, pp. 27–37, Sep. 2004, doi: 10.1016/J.JNEUMETH.2004.03.005.
- [114] X. A. Perez, D. Zhang, T. Bordia, and M. Quik, “Striatal D1 medium spiny neuron activation induces dyskinesias in parkinsonian mice,” *Mov. Disord.*, vol. 32, no. 4, p. 538, Apr. 2017, doi: 10.1002/MDS.26955.
- [115] B. Mossink *et al.*, “Stem Cell Reports Article Human neuronal networks on micro-

- electrode arrays are a highly robust tool to study disease-specific genotype-phenotype correlations in vitro,” 2021, doi: 10.1016/j.stemcr.2021.07.001.
- [116] D. A. Wagenaar, J. Pine, and S. M. Potter, “An extremely rich repertoire of bursting patterns during the development of cortical cultures,” *BMC Neurosci.*, vol. 7, Feb. 2006, doi: 10.1186/1471-2202-7-11.
- [117] M. Chiappalone, M. Bove, A. Vato, M. Tedesco, and S. Martinoia, “Dissociated cortical networks show spontaneously correlated activity patterns during in vitro development,” *Brain Res.*, vol. 1093, no. 1, pp. 41–53, Jun. 2006, doi: 10.1016/J.BRAINRES.2006.03.049.
- [118] S. Illes, W. Fleischer, M. Siebler, H. P. Hartung, and M. Dihn  , “Development and pharmacological modulation of embryonic stem cell-derived neuronal network activity,” *Exp. Neurol.*, vol. 207, no. 1, pp. 171–176, Sep. 2007, doi: 10.1016/J.EXPNEUROL.2007.05.020.
- [119] E. Biffi, G. Regalia, A. Menegon, G. Ferrigno, and A. Pedrocchi, “The Influence of Neuronal Density and Maturation on Network Activity of Hippocampal Cell Cultures: A Methodological Study,” *PLoS One*, vol. 8, no. 12, p. e83899, Dec. 2013, doi: 10.1371/JOURNAL.PONE.0083899.
- [120] P. Charlesworth, E. Cotterill, A. Morton, S. G. N. Grant, and S. J. Egl  n, “Quantitative differences in developmental profiles of spontaneous activity in cortical and hippocampal cultures,” *Neural Dev.*, vol. 10, no. 1, p. 1, Jan. 2015, doi: 10.1186/S13064-014-0028-0.

- [121] H. Kamioka, E. Maeda, Y. Jimbo, H. P. C. Robinson, and A. Kawana, "Spontaneous periodic synchronized bursting during formation of mature patterns of connections in cortical cultures," *Neurosci. Lett.*, vol. 206, no. 2–3, pp. 109–112, Mar. 1996, doi: 10.1016/S0304-3940(96)12448-4.
- [122] H. T. Hogberg, T. Sobanski, A. Novellino, M. Whelan, D. G. Weiss, and A. K. Bal-Price, "Application of micro-electrode arrays (MEAs) as an emerging technology for developmental neurotoxicity: Evaluation of domoic acid-induced effects in primary cultures of rat cortical neurons," *Neurotoxicology*, vol. 32, no. 1, pp. 158–168, Jan. 2011, doi: 10.1016/J.NEURO.2010.10.007.
- [123] A. Bikbaev, R. Frischknecht, and M. Heine, "Brain extracellular matrix retains connectivity in neuronal networks," *Sci. Reports 2015 51*, vol. 5, no. 1, pp. 1–12, Sep. 2015, doi: 10.1038/srep14527.
- [124] D. J. Bakkum, Z. C. Chao, and S. M. Potter, "Long-Term Activity-Dependent Plasticity of Action Potential Propagation Delay and Amplitude in Cortical Networks," *PLoS One*, vol. 3, no. 5, p. e2088, May 2008, doi: 10.1371/JOURNAL.PONE.0002088.
- [125] D. J. Bakkum, Z. C. Chao, and S. M. Potter, "Spatio-temporal electrical stimuli shape behavior of an embodied cortical network in a goal-directed learning task," *J. Neural Eng.*, vol. 5, no. 3, pp. 310–323, Sep. 2008, doi: 10.1088/1741-2560/5/3/004.
- [126] P. Valdivia, M. Martin, W. R. LeFew, J. Ross, K. A. Houck, and T. J. Shafer,

- “Multi-well microelectrode array recordings detect neuroactivity of ToxCast compounds,” *Neurotoxicology*, vol. 44, pp. 204–217, 2014, doi: 10.1016/J.NEURO.2014.06.012.
- [127] K. Wallace, J. D. Strickland, P. Valdivia, W. R. Mundy, and T. J. Shafer, “A multiplexed assay for determination of neurotoxicant effects on spontaneous network activity and viability from microelectrode arrays,” *Neurotoxicology*, vol. 49, pp. 79–85, Jul. 2015, doi: 10.1016/J.NEURO.2015.05.007.
- [128] C. Lu *et al.*, “Micro-electrode array recordings reveal reductions in both excitation and inhibition in cultured cortical neuron networks lacking Shank3,” *Mol. Psychiatry*, vol. 21, no. 2, pp. 159–168, Feb. 2016, doi: 10.1038/MP.2015.173.
- [129] B. J. Wainger *et al.*, “Intrinsic membrane hyperexcitability of amyotrophic lateral sclerosis patient-derived motor neurons,” *Cell Rep.*, vol. 7, no. 1, pp. 1–11, Oct. 2014, doi: 10.1016/J.CELREP.2014.03.019.
- [130] T. Chailangkarn *et al.*, “A human neurodevelopmental model for Williams syndrome,” *Nature*, vol. 536, no. 7616, pp. 338–343, Aug. 2016, doi: 10.1038/NATURE19067.
- [131] G. W. Gross, A. Harsch, B. K. Rhoades, and W. Göpel, “Odor, drug and toxin analysis with neuronal networks in vitro: extracellular array recording of network responses,” *Biosens. Bioelectron.*, vol. 12, no. 5, pp. 373–393, Jan. 1997, doi: 10.1016/S0956-5663(97)00012-2.
- [132] A. F. M. Johnstone, G. W. Gross, D. G. Weiss, O. H. U. Schroeder, A. Gramowski,

- and T. J. Shafer, “Microelectrode arrays: a physiologically based neurotoxicity testing platform for the 21st century,” *Neurotoxicology*, vol. 31, no. 4, pp. 331–350, Aug. 2010, doi: 10.1016/J.NEURO.2010.04.001.
- [133] J. Nicolas *et al.*, “Detection of marine neurotoxins in food safety testing using a multielectrode array,” *Mol. Nutr. Food Res.*, vol. 58, no. 12, pp. 2369–2378, Dec. 2014, doi: 10.1002/MNFR.201400479.
- [134] A. P. Passaro, O. Aydin, M. T. A. Saif, and S. L. Stice, “Development of an objective index, neural activity score (NAS), reveals neural network ontogeny and treatment effects on microelectrode arrays,” *Sci. Rep.*, vol. 11, no. 1, p. 9110, Apr. 2021, doi: 10.1038/S41598-021-88675-W.
- [135] L. C. Katz and C. J. Shatz, “Synaptic Activity and the Construction of Cortical Circuits,” *Science (80-.)*, vol. 274, no. 5290, pp. 1133–1138, Nov. 1996, doi: 10.1126/SCIENCE.274.5290.1133.
- [136] Y. Ben-Ari, “Developing networks play a similar melody,” *Trends Neurosci.*, vol. 24, no. 6, pp. 353–360, Jun. 2001, doi: 10.1016/S0166-2236(00)01813-0.
- [137] R. E. Baker, M. A. Corner, and J. van Pelt, “Spontaneous neuronal discharge patterns in developing organotypic mega-co-cultures of neonatal rat cerebral cortex,” *Brain Res.*, vol. 1101, no. 1, pp. 29–35, Jun. 2006, doi: 10.1016/J.BRAINRES.2006.05.028.
- [138] R. Khazipov, A. Sirota, X. Leinekugel, G. L. Holmes, Y. Ben-Ari, and G. Buzsáki, “Early motor activity drives spindle bursts in the developing somatosensory

- cortex,” *Nat. 2005 4327018*, vol. 432, no. 7018, pp. 758–761, Dec. 2004, doi: 10.1038/nature03132.
- [139] B. Arthur, F. Renato, and H. Martin, “Brain extracellular matrix retains functional connectivity in mature neuronal networks,” *Front. Neurosci.*, vol. 10, 2016, doi: 10.3389/FCONF.NINS.2016.93.00050/ABSTRACT.
- [140] D. J. Bakkum, Z. C. Chao, and S. M. Potter, “Long-Term Activity-Dependent Plasticity of Action Potential Propagation Delay and Amplitude in Cortical Networks,” *PLoS One*, vol. 3, no. 5, p. e2088, May 2008, doi: 10.1371/JOURNAL.PONE.0002088.
- [141] C. C. McIntyre and W. M. Grill, “Selective Microstimulation of Central Nervous System Neurons,” *Ann. Biomed. Eng. 2000 283*, vol. 28, no. 3, pp. 219–233, 2000, doi: 10.1114/1.262.
- [142] D. V. Hansen, J. L. R. Rubenstein, and A. R. Kriegstein, “Deriving excitatory neurons of the neocortex from pluripotent stem cells,” *Neuron*, vol. 70, no. 4, p. 645, May 2011, doi: 10.1016/J.NEURON.2011.05.006.
- [143] Y. Shi, P. Kirwan, J. Smith, H. P. C. Robinson, and F. J. Livesey, “Human cerebral cortex development from pluripotent stem cells to functional excitatory synapses,” *Nat. Neurosci.*, vol. 15, no. 3, pp. 477–486, Mar. 2012, doi: 10.1038/NN.3041.
- [144] F. Soldner *et al.*, “Generation of isogenic pluripotent stem cells differing exclusively at two early onset Parkinson point mutations,” *Cell*, vol. 146, no. 2, pp. 318–331, Jul. 2011, doi: 10.1016/J.CELL.2011.06.019.

- [145] A. Odawara, Y. Saitoh, A. H. Alhebshi, M. Gotoh, and I. Suzuki, “Long-term electrophysiological activity and pharmacological response of a human induced pluripotent stem cell-derived neuron and astrocyte co-culture,” *Biochem. Biophys. Res. Commun.*, vol. 443, no. 4, pp. 1176–1181, Jan. 2014, doi: 10.1016/J.BBRC.2013.12.142.
- [146] J. E. Kim *et al.*, “Investigating synapse formation and function using human pluripotent stem cell-derived neurons,” *Proc. Natl. Acad. Sci. U. S. A.*, vol. 108, no. 7, pp. 3005–3010, Feb. 2011, doi: 10.1073/PNAS.1007753108.
- [147] T. Hiragi *et al.*, “Differentiation of human induced pluripotent stem cell (hiPSC)-derived neurons in mouse hippocampal slice cultures,” *Front. Cell. Neurosci.*, vol. 11, May 2017, doi: 10.3389/FNCEL.2017.00143.
- [148] K. Fukushima, Y. Miura, K. Sawada, K. Yamazaki, and M. Ito, “Establishment of a Human Neuronal Network Assessment System by Using a Human Neuron/Astrocyte Co-Culture Derived from Fetal Neural Stem/Progenitor Cells,” *J. Biomol. Screen.*, vol. 21, no. 1, pp. 54–64, Jan. 2016, doi: 10.1177/1087057115610055.
- [149] J. Mertens, M. C. Marchetto, C. Bardy, and F. H. Gage, “Evaluating cell reprogramming, differentiation and conversion technologies in neuroscience,” *Nat. Rev. Neurosci.*, vol. 17, no. 7, pp. 424–437, Jul. 2016, doi: 10.1038/NRN.2016.46.
- [150] A. Hyysalo, M. Ristola, E.-L. Mäkinen, S. Häyrynen, M. Nykter, and S. Narkilahti, “Laminin $\alpha 5$ substrates promote survival, network formation and functional

- development of human pluripotent stem cell-derived neurons in vitro,” 2017, doi: 10.1016/j.scr.2017.09.002.
- [151] N. Mallet, C. Le Moine, S. Charpier, and F. Gonon, “Feedforward Inhibition of Projection Neurons by Fast-Spiking GABA Interneurons in the Rat Striatum In Vivo,” *J. Neurosci.*, vol. 25, no. 15, pp. 3857–3869, Apr. 2005, doi: 10.1523/JNEUROSCI.5027-04.2005.
- [152] C. J. Wilson, “The generation of natural firing patterns in neostriatal neurons,” *Prog. Brain Res.*, vol. 99, no. C, pp. 277–297, Jan. 1993, doi: 10.1016/S0079-6123(08)61352-7.
- [153] J. Arama *et al.*, “GABAA receptor activity shapes the formation of inhibitory synapses between developing medium spiny neurons,” *Front. Cell. Neurosci.*, vol. 9, no. AUGUST, p. 290, Aug. 2015, doi: 10.3389/FNCEL.2015.00290/BIBTEX.
- [154] R. W. Olsen, “Picrotoxin-like channel blockers of GABAA receptors,” *Proc. Natl. Acad. Sci. U. S. A.*, vol. 103, no. 16, pp. 6081–6082, Apr. 2006, doi: 10.1073/PNAS.0601121103/ASSET/7E96FFEF-3F49-4642-9D09-079A151A90B1/ASSETS/GRAPHIC/ZPQ0170620100001.JPEG.